AC

CALIBRATION OF SEASAT SCATTEROMETER USING TROPICAL RAINFOREST

A Thesis
Submitted to the
Department of Electrical and Computer Engineering
Brigham Young University

In Partial Fulfillment
of the Requirements for the Degree
Master of Science

by
Gary B. Skouson
October 1992

This thesis by Gary B. Skouson is accepted in its present form by the Department of Electrical and Computer Engineering of Brigham Young University as satisfying the thesis requirement for the degree of Master of Science.

David G. Long
Committee Chairman

A. Lee Swindlehurst
Committee Member

Richard H. Selfridge
Graduate Coordinator

11/20/92
Date

ACKNOWLEDGMENTS

I am grateful to many people for the help which I have received on this paper. I thank Dr. David G. Long for the time which he spent in discussing the data, model and imaging techniques. I am also grateful for the time which he has spent correcting my writing to make this and other papers readable. I would like to thank Warren B. Davis for his help in developing many of the routines used in plotting the data.

I am especially grateful for my wife Darlene for all that she has done to help me get through school.

The data used in this research was obtained from the Physical Oceanography DACC at Jet Propulsion Laboratory/California Institute of Technology.

CONTENTS

Acknowledgments iii

1 Introduction 1

2 Scatterometer Description 3
- 2.1 Scatterometer Basics . . . 3
- 2.2 Seasat Scatterometer Description . . . 4

3 Data Description 9
- 3.1 Description of Data Set Characteristics . . . 9
  - 3.1.1 Data Set Selection . . . 9
  - 3.1.2 Location determination . . . 10
- 3.2 Scatterometer Peak Gain And Antenna Pattern . . . 14
  - 3.2.1 Antenna Biases . . . 14
- 3.3 Time Response . . . 19

4 Model Development 23
- 4.1 Introduction . . . 23
- 4.2 Model Method . . . 23
- 4.3 Model Parameters . . . 24
- 4.4 Selecting Polynomial Order . . . 26

5 Model Parameter Estimation 28
- 5.1 Polynomial Parameter Estimation . . . 28
- 5.2 Cell Gain Bias Estimation . . . 30
  - 5.2.1 Window Length Determination . . . 30

6 Correction Method 44
- 6.1 Introduction . . . 44
- 6.2 Model Parameters . . . 44
- 6.3 Reference Equation Selection . . . 46
  - 6.3.1 Polynomial Response . . . 46
  - 6.3.2 Seasonal Correction . . . 47
- 6.4 Example Correction . . . 48

7 Recalibration Assessment 54
- 7.1 Linearity and Error Comparison . . . 54
- 7.2 Parameter Location Dependance . . . 56
- 7.3 Image Improvement . . . 56

8 Conclusions 67
8.1 Discussion 67
8.2 Findings 67
8.3 Further Work 68

A Amazon Data 71

B Congo Data 83

LIST OF FIGURES

2.1 Plots showing experimental results of the relationship between σ° and θ_i for different surfaces from [2] 5
2.2 SASS scatterometer antenna pattern 6
2.3 Antenna illumination pattern and iso-Doppler intersections 7
2.4 Total integrated cell area for Doppler cells 8
3.1 The original SIRF image from which the area for the data set is chosen. 11
3.2 The landmask used in selecting the calibration data set. The gray area is the area of the data selection mask. White and black are not within the 1 dB region 12
3.3 This shows the landmask with the mask region showing differences in terrain over the region. The divisions on the image show the four split regions to be used in testing spatial variations 13
3.4 Plot of σ° versus θ_i for antenna # 1. (Ascending on top and descending on bottom.) 15
3.5 Plot of σ° versus θ_i for antenna # 2. (Ascending on top and descending on bottom.) 16
3.6 Plot of σ° versus θ_i for antenna # 3. (Ascending on top and Descending on bottom.) 17
3.7 Plot of σ° versus θ_i for antenna # 4. (Ascending on top and Descending on bottom.) 18
3.8 Illustration of mean and variance before correction 19
3.9 Illustration of the mean and variance after the calibration correction has been done 19
3.10 σ° values over time. Ascending (top) and descending (bottom) . . 21
3.11 Plot of time of day as a function of day number 22
4.1 Diagram of the processing model 25
5.1 This shows the constant term from a polynomial fit using four, (top) eight (middle) and sixteen (bottom) day time windows 33
5.2 Model A parameters for ascending (top) and descending (bottom) passes 34
5.3 Model B parameters for the ascending (top) and descending (bottom) passes 35
5.4 Model C parameters for the ascending (top) and descending (bottom) passes 36
5.5 Model D parameters for the ascending (top) and descending (bottom) passes 37
5.6 Model E parameters for the ascending (top) and descending (bottom) passes 38

5.7 Model cell gain bias parameters. Top, cells 1 - 4, center, cells 5 - 8 and bottom cells 9 - 12. 39
5.8 Measurement model for antenna 1 ascending (top) and descending (bottom) 40
5.9 Measurement model for antenna 2 ascending (top) and descending (bottom) 41
5.10 Measurement model for antenna 3 ascending (top) and descending (bottom) 42
5.11 Measurement model for antenna 4 ascending (top) and descending (bottom) 43
6.1 Correction to be made for antenna 1 Ascending (top) and descending (bottom). 50
6.2 Correction to be made for antenna 2 Ascending (top) and descending (bottom). 51
6.3 Correction to be made for antenna 3 Ascending (top) and descending (bottom). 52
6.4 Correction to be made for antenna 4 Ascending (top) and descending (bottom). 53
7.1 Plot of the mean and variance for uncorrected (top) and corrected (bottom) measurements 55
7.2 A parameters for sections NW (top) and SW (bottom) of the calibration data set 57
7.3 A parameters for sections NE (top) and SE (bottom) of the calibration data set 58
7.4 Estimated A parameters over the Congo rain forest. Ascending (top) and Descending (bottom) 59
7.5 The SIRF image made using corrected measurements. 60
7.6 This shows the improvement in the corrected image (top) over the uncorrected image (bottom) 61
7.7 This shows the improvement in the corrected image (top) over the uncorrected image (bottom) 62
7.8 The Congo SIRF image made using uncorrected measurements. . . 63
7.9 The Congo SIRF image made using corrected measurements. 64
7.10 Land mask made using the corrected SIRF image 66
A.1 Model A parameters estimated from the corrected mask. Ascending (top), descending (bottom). 72
A.2 Model B parameters estimated from the corrected mask. Ascending (top), descending (bottom). 73
A.3 Model C parameters estimated from the corrected mask. Ascending (top), descending (bottom). 74
A.4 Model D parameters estimated from the corrected mask. Ascending (top), descending (bottom). 75

A.5 Model E parameters estimated from the corrected mask. Ascending (top), descending (bottom). 76
A.6 Model Cell gain biases estimated from the corrected mask. Cells 1 - 4 (top), 5 - 8 (middle) and 9 - 12 (bottom). 77
A.7 Difference between the Amazon model using the original and corrected land masks for antenna 1. Ascending (top), descending (bottom). 78
A.8 Difference between the Amazon model using the original and corrected land masks for antenna 2. Ascending (top), descending (bottom). 79
A.9 Difference between the Amazon model using the original and corrected land masks for antenna 3. Ascending (top), descending (bottom). 80
A.10 Difference between the Amazon model using the original and corrected land masks for antenna 4. Ascending (top), descending (bottom). 81
B.1 Variance around a linear regression for the Congo measurements for uncorrected (top) measurements and for measurements corrected with the Amazon correction factors. 84
B.2 Model A parameters estimated from the corrected mask. Ascending (top), descending (bottom). 85
B.3 Model B parameters estimated from the corrected mask. Ascending (top), descending (bottom). 86
B.4 Model C parameters estimated from the corrected mask. Ascending (top), descending (bottom). 87
B.5 Model D parameters estimated from the corrected mask. Ascending (top), descending (bottom). 88
B.6 Model E parameters estimated from the corrected mask. Ascending (top), descending (bottom). 89
B.7 Model Cell gain biases estimated from the corrected mask. Cells 1 - 4 (top), 5 - 8 (middle) and 9 - 12 (bottom). 90
B.8 Difference between the Amazon model and the Congo model for antenna 1. Ascending (top), descending (bottom). 91
B.9 Difference between the Amazon model and the Congo model for antenna 2. Ascending (top), descending (bottom). 92
B.10 Difference between the Amazon model and the Congo model for antenna 3. Ascending (top), descending (bottom). 93
B.11 Difference between the Amazon model and the Congo model for antenna 4. Ascending (top), descending (bottom). 94

CHAPTER 1

INTRODUCTION

The Seasat-A satellite scatterometer (SASS) was launched in June, 1978. It was designed to measure wind vectors over the ocean using the backscatter measurement[1]. Measurements were recorded from July 6 until October 10, 1978, when the satellite power system failed.

Previous studies of SASS data show that inconsistencies exist in the data, especially between different antennas and resolution cells. Because of these inconsistencies, it is desirable to correct the measurements. In 1984, Bracalente and Sweet [1] developed an algorithm to compensate for small gain biases in the measurements. This algorithm also included a method for more accurately determining the system noise power. However even using these corrections the gain bias between measurements made with different antennas and cells is still evident. This report describes a method for removing these biases from the measurements, giving a more consistent data set. In the recalibration method described here, all of the measurements have been previously corrected using the algorithm developed by Bracalante and Sweet [1].

After analyzing the SASS data, a model for the measurements is developed. This model describes the response of the antennas and cells with respect to incidence angle and time. Using this model, a correction is calculated for each measurement in order to remove the inconsistencies in the data. This analysis of the data and the measurement model are the main contributions of this work.

Chapter 2 contains background information about the Seasat scatterometer relevant to the data correction. Next, a discussion is given of the methods used in obtaining a data set for analysis and modeling. From this data set, errors and problems with the data are discussed. A model for the data will be described in Chapter 4 and a method for estimating the model parameters will be given in

[1]The backscatter is a measure of the power reflected by an object or surface when it is illuminated by a pulse of radar energy. This reflected power gives a measure of the scattering characteristics of the surface.

the following chapter. Chapter 6 describes methods for recalibrating the measurements using the measurement model. In Chapter 7, the effects of the recalibration will be given. A summary of the findings and results of the recalibration will then be presented.

CHAPTER 2

SCATTEROMETER DESCRIPTION

2.1 Scatterometer Basics

A scatterometer is a radar that transmits a signal and then measures the power reflected from a surface. This provides a measure of the scattering characteristics of the surface. The main characteristic that is used to describe the surface is the normalized radar cross section, σ°. The equation for σ° is given by

$$\sigma^\circ = \frac{(4\pi)^3 P_R R^4}{P_T \lambda^2 L_s G^2 A} \tag{2.1}$$

where [3]

$$\begin{aligned} P_R &= \text{received power} \\ P_T &= \text{transmitted power} \\ R &= \text{range from scatterometer to measurement surface} \\ \lambda &= \text{signal wavelength} \\ L_s &= \text{system losses} \\ G &= \text{antenna gain} \\ A &= \text{measurement area} \end{aligned} \tag{2.2}$$

Parameters P_T through A are determined at the time of measurement or from tests done prior to making the measurement. In order to obtain a highly accurate measurement of the return power (P_R), a measurement of the noise power (P_n) is subtracted from the signal plus noise measurement (P_{s+n}), i.e.,

$$P_R = P_{s+n} - P_n \tag{2.3}$$

The quantity σ°, is essentially a measurement of the *brightness* of the surface being illuminated. The brightness depends on the particular frequency,

polarization and incidence angle used. This measurement is useful in calculating winds over the ocean [4] and in discriminating between vegetation types[5, 6].

In general, σ° is a function of the incidence angle (θ_i) at which the measurements are taken, with larger incidence angles producing smaller values for σ°. At small deviations from a 40° angle, this relationship is almost linear. Because of this, the relationship between σ° and θ_i has been modeled as a line [1, 7]:

$$\sigma^\circ = a + b(\theta_i - \phi), \tag{2.4}$$

where a and b are respectively the intercept and slope of the line, and ϕ is chosen to be within the linear region. Examples of the relationship between σ° and θ_i over different surfaces are shown in Figure 2.1.

2.2 Seasat Scatterometer Description

The Seasat scatterometer (SASS) was an interrupted-CW radar which operated at 14.6 GHz. It had four antennas and a peak transmission power of 100 W. Each of the four antennas was able to operate in both horizontal and vertical polarization modes thus giving eight possible *beams*. These antennas were arranged so that the antenna illumination patterns were at 90° angles from each other. Figure 2.2 illustrates the satellite antenna illumination pattern at the earth's surface. Doppler filtering was used to split the antenna beam into fifteen resolution cells along the antenna illumination pattern, providing a much higher resolution than the antenna beam alone would give. This Doppler filtering is explained further below.

The measurements for a single antenna were taken during a 1.89s measurement period. During this period, 64 transmit/receive pulses were sent. The first three pulses were used to scale the gain for each cell in one of four possible gain states. The remaining 61 samples were combined to obtain the received power average. Only one antenna was sampled at a time, with each of four beams observed in sequence. The completion time for this four beam measurement cycle was 7.56s. This time was designed to give a 50 km spacing between the measurements from a given beam [4].

The velocity difference between the earth and the spacecraft causes a frequency shift in the return signal. The amount of this frequency shift, known

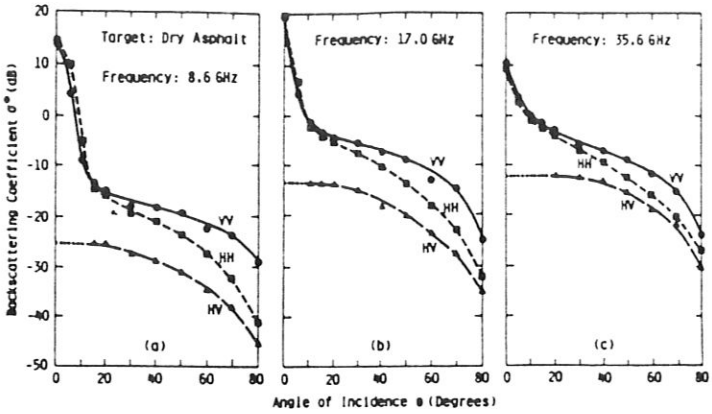

Angular response of the scattering coefficient of dry asphalt at (a) 8.6 GHz, (b) 17.0 GHz, and (c) 35.6 GHz (from Stiles *et al.*, 1979).

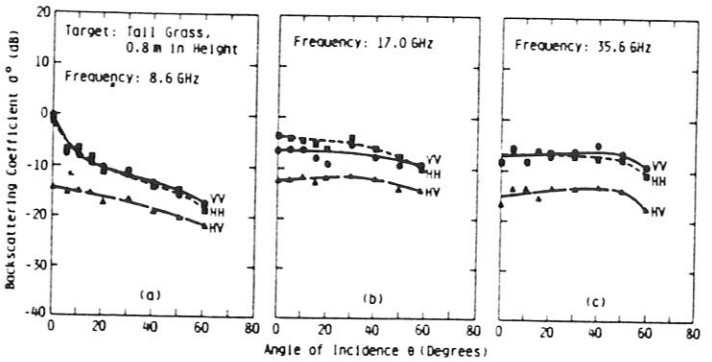

Angular response of the scattering coefficient of tall grass at (a) 8.6 GHz, (b) 17.0 GHz, and (c) 35.6 GHz.

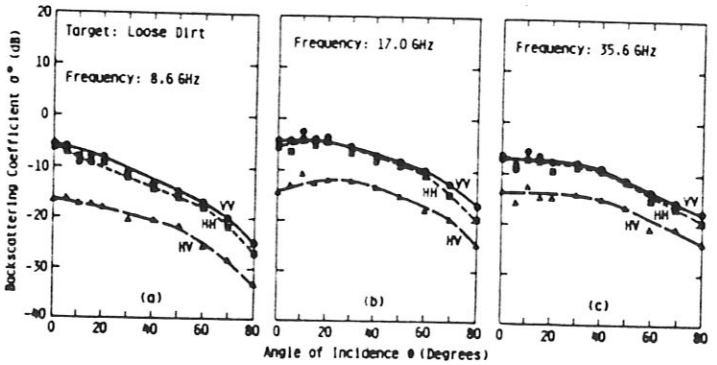

Angular response of the scattering coefficient of loose dirt at (a) 8.6 GHz, (b) 17.0 GHz, and (c) 35.6 GHz.

Figure 2.1: Plots showing experimental results of the relationship between σ° and θ_i for different surfaces from [2]

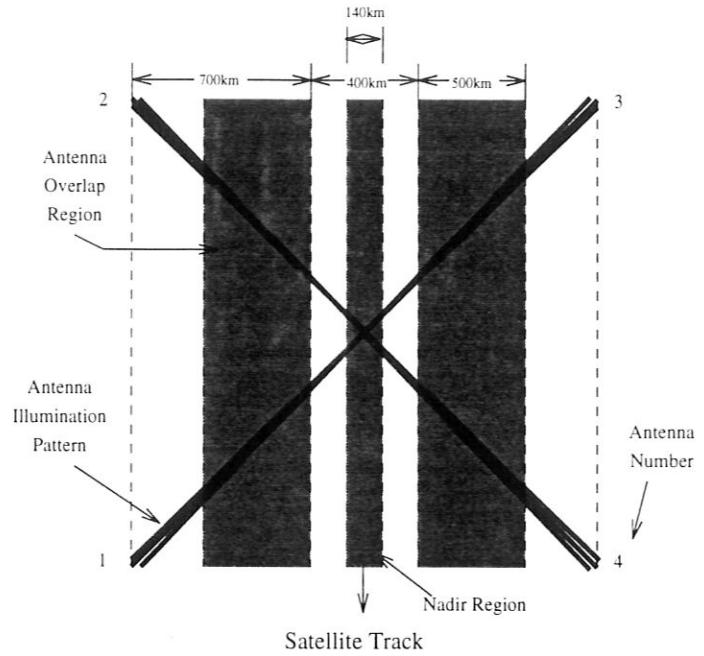

Figure 2.2: SASS scatterometer antenna pattern

as a Doppler shift, depends on the location of the measurement relative to the spacecraft. This Doppler shift in the frequency of the return signal will be greatest for locations directly in front of or behind the spacecraft, while locations directly below or to the side of the satellite have little change in frequency. The difference in frequency of the return signal allows the signal to be separated by location, using band pass filters. This technique is known as Doppler filtering.

Ideally, the iso-Doppler curves are hyperbolic with the major axis running along the path of the satellite subtrack (see Figure 2.3). Due to the rotation and curvature of the earth, the major axis of the hyperbolic iso-Doppler lines is tilted from the satellite subtrack by 3.5° at the equator [4]. Figure 2.3 illustrates the intersections of the antenna illumination pattern with the iso-Doppler lines. Unfortunately, this skew of the iso-Doppler lines was not taken into account when designing the filters for the Seasat mission.

Using Doppler filtering, each antenna was split into fifteen cells. Of these cells, twelve are out from the satellite subtrack at incidence angles ranging from about 20° to 75°. The other three cells are closer to the satellite subtrack with small incidence angles from the satellite. These three cells at small incidence

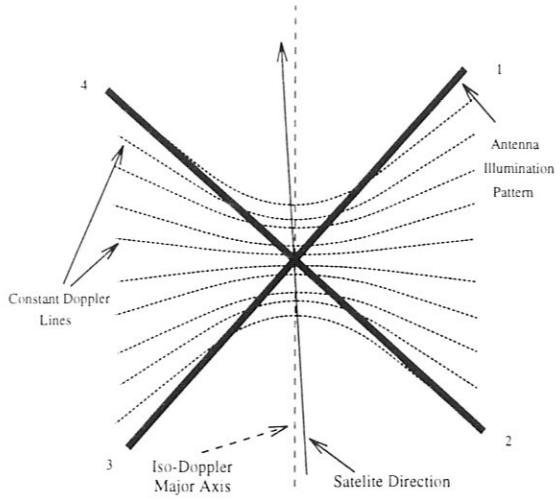

Figure 2.3: Antenna illumination pattern and iso-Doppler intersections

angles are not used in land imaging applications, as they are far from the linear response region.

Because of the tilt of the iso-Doppler lines, the size, location and incidence angle for a given cell may be quite different from the fore to aft beams, or from ascending to descending passes. In Figure 2.3, observe that the iso-Doppler lines and the antenna illumination pattern intersect at different distances from the satellite subtrack from the fore to the aft beams.

The actual measurement cells are found by using the instantaneous Doppler cell area and then integrating over the time that the measurements are being taken. By doing this we get a cell shape for the total measurement cell as illustrated in Figure 2.4 [3].

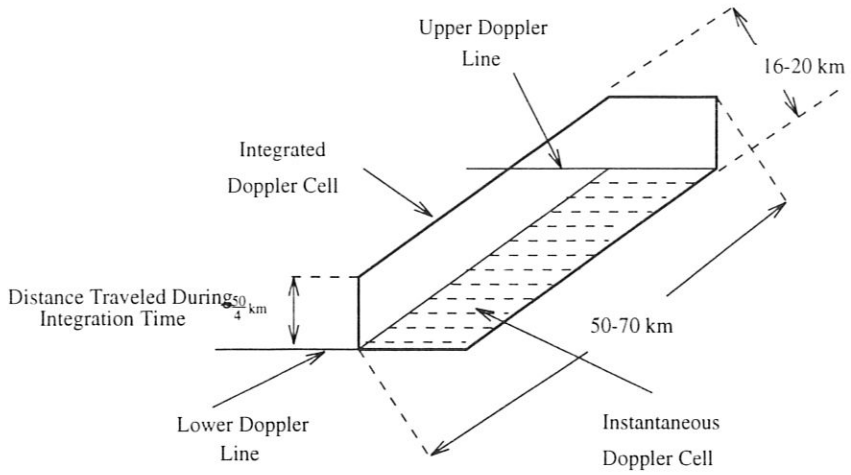

Figure 2.4: Total integrated cell area for Doppler cells

CHAPTER 3

DATA DESCRIPTION

3.1 Description of Data Set Characteristics

The σ° measurements must be accurate in order to obtain an accurate estimate of wind vectors, or to accurately image vegetation types. However, discrepancies may arise due to calibration errors. This chapter will discuss the Seasat data in general and some of the possible sources of errors in the data. This discussion deals with time-varying as well as time-stationary errors that may occur in the measurements.

In order to make an accurate evaluation of the SASS data it is necessary to select a homogenous area from which to acquire measurements to study. By using such a data set, any variations in the data will be due to differences in the measurement process.

3.1.1 Data Set Selection

In selecting measurements to be used in the calibration and study of SASS data, a homogeneous extended-area target is used. The Amazon rain forest has been used in past calibration studies [1, 7]. This area is considered to be good for calibration purposes because of its large area of uniform terrain and vegetation response. One concern is that the area must be isotropic with respect to azimuthal variations. Previous studies have determined that the Amazon rain forest is homogeneous and isotropic[1, 7]. Because there are only a few specific azimuth angles at which measurements are made, it is difficult to determine if any inconsistencies in the measurements are due to azimuthal variations, or if they are due to the changes in the land cover or the antenna parameters over time. However, the geometry of the leaves and the trees in the forest are expected to provide uniform scattering for all azimuth angles.

Besides having an area which is isotropic and homogeneous, it is important that the area contain sufficient measurements to reduce the effects of noise

on the calibration calculations. The size of the area is also important in making sure that the side-lobes of the antenna are still within a fairly homogeneous region. Using a large data set from a consistent area will help ensure that the calibration data set is as consistent as possible with respect to location, thus reducing errors due to location. Because of the lack of coverage from the horizontal polarization measurements, only vertical polarization is considered in this report.

3.1.2 Location determination

Although the Amazon area is quite homogeneous, some spatial variation is evident (Figure 3.1). Thus, a crucial step in selecting the calibration data set within the Amazon forest is the selection of the actual area from which the data set will come. This area should have a small range of σ° while being sufficiently large. In order to select such an area, the Scatterometer Image Reconstruction Technique with Filtering (SIRF) algorithm [5, 6] was used to make an image of the Amazon area using the uncorrected σ° measurements. The image used is shown in Figure 3.1. From this image, an area corresponding to $\sigma^\circ \in$ [-7,-8] dB was selected. Although the range of σ° from locations covered by this mask is 1 dB, the deviation of the averages of the measurements will be smaller due to the large number of measurements being used. The selected area is shown in Figure 3.2. Only those measurements which fall completely inside of this mask area (grey) are to be used in the following chapters. By doing this, all of the measurements used will be from the same type of terrain and thus will give the same response.

Although this land mask has been selected to ensure that the variations of the measurements are small, there may still be some variations due to location. Figure 3.3 shows the land of the mask area with a plotting scale selected to expose existing variations. This area is split into four sections. While no obvious correlation exists, the calibration procedure may be followed for the entire region and for each of the sections separately. This gives an indication of how sensitive the calibration method is to location. The split of the areas will be done along lines of 4° south latitude and 63° west longitude with the sections being called SW, NW, NE and SE depending on the location of the section as shown in Figure 3.3

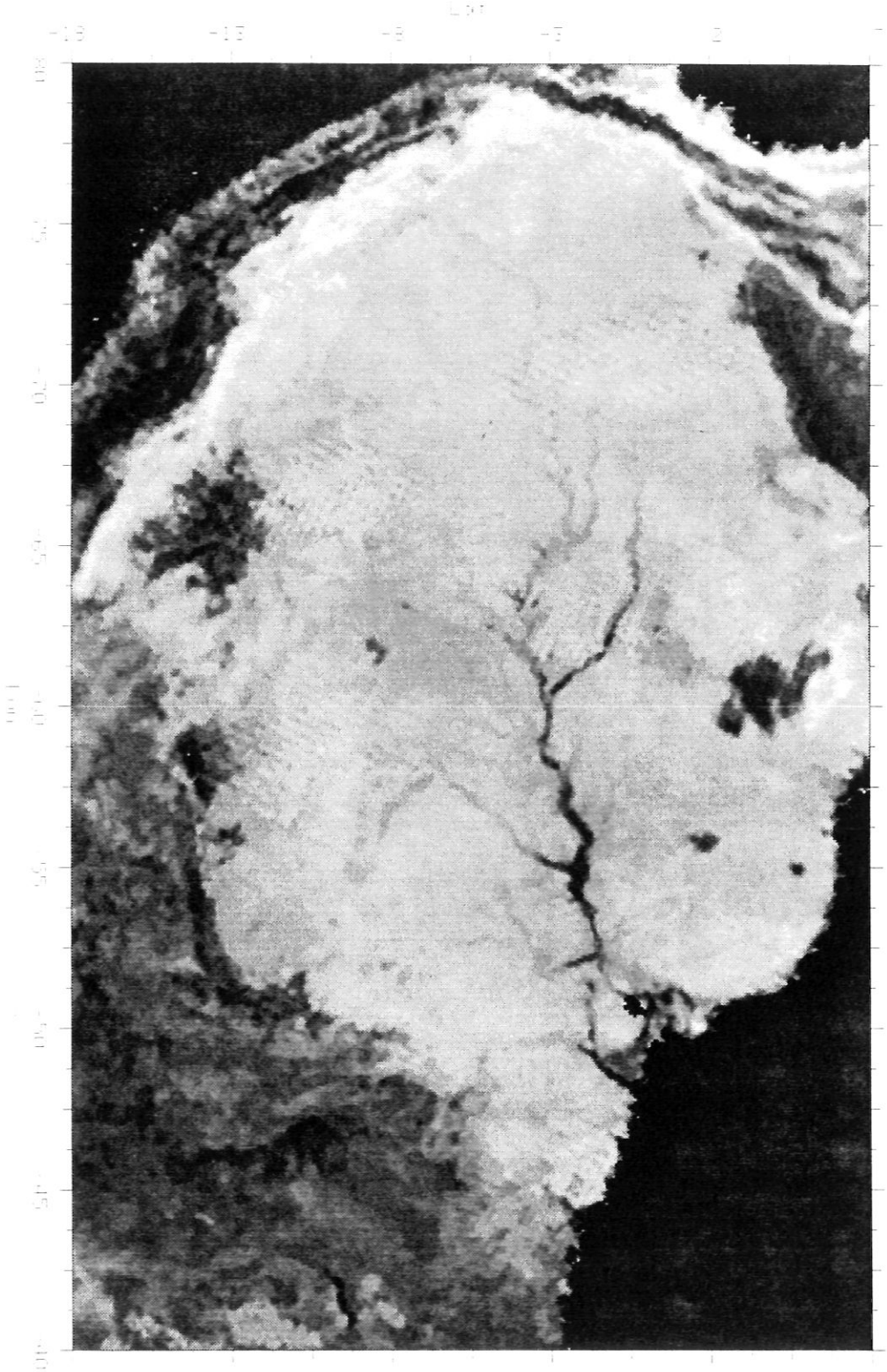

Figure 3.1: The original SIRF image from which the area for the data set is chosen.

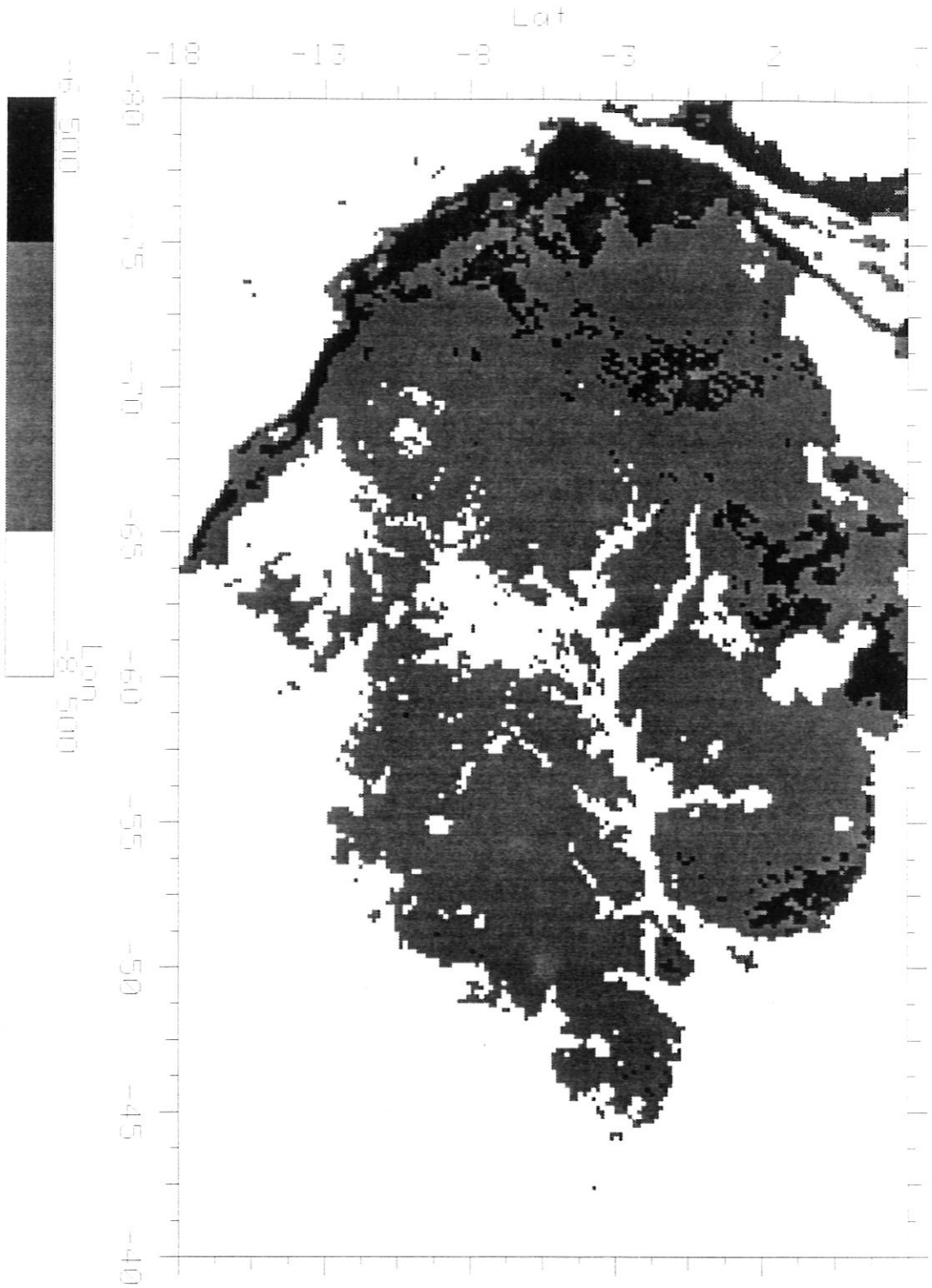

Figure 3.2: The landmask used in selecting the calibration data set. The gray area is the area of the data selection mask. White and black are not within the 1 dB region

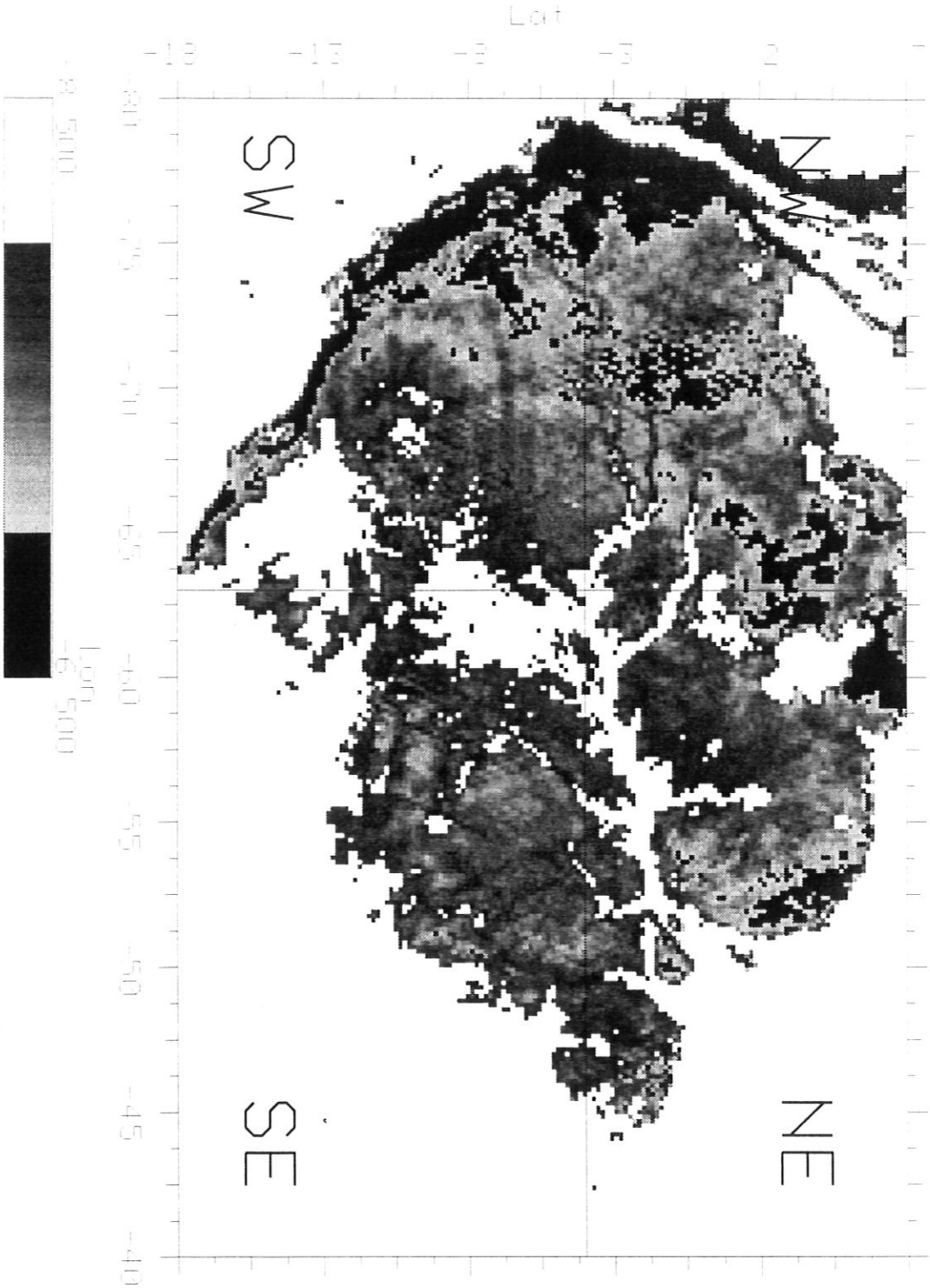

Figure 3.3: This shows the landmask with the mask region showing differences in terrain over the region. The divisions on the image show the four split regions to be used in testing spatial variations

3.2 Scatterometer Peak Gain And Antenna Pattern

The response of σ° versus θ_i is shown in Figures 3.4 through 3.7 for the selected area.[1] The measurements for these plots are split into ascending and descending passes, covering the first 30 days of the mission. These plots follow the experimental data shown in Figure 2.1 from Chapter 2 reasonably well. Although the response of the data is quite close to the expected response for scatterometer data, it is noted that the response from one antenna to another, or from ascending to descending passes, is not the same.

3.2.1 Antenna Biases

From the σ° versus θ_i plots, it can be seen that there are differences in the σ° response of the antennas. These differences are in part due to the differences in the antenna gain pattern and also the process used in filtering, amplifying and recording the measurements. Some of these differences in the data may come from the bandpass filter gains used in determining the cell power received. The gain variations in these filters are expected to be quite a bit smaller than the variations in the antenna and land cover.

Figure 3.8 is a representation of the measurements in a single incidence angle bin from four antennas where

$$m_{ai} = \text{ mean for antenna } i$$

and

$$m_o = \text{ mean for combined measurements}$$

and the horizontal position is arbitrary. This plot illustrates the mean m_a and variance of the measurements from each individual antenna and the overall mean and variance of the combined measurements. Here we assume that all of the data has been collected from the same incidence angle bin and thus should have roughly the same antenna and cell gain for each of the individual antennas. The effect of

[1] Many of these and later plots are generated by binning the measurements in a two dimensional grid. The bins with a number of measurements below a given threshold are white while those bins having more than a maximum threshold are black. Bins having a number of measurements between these two thresholds are given a shade of grey depending on the number of measurements. The usual upper and lower cutoffs are 10 and 1 respectively.

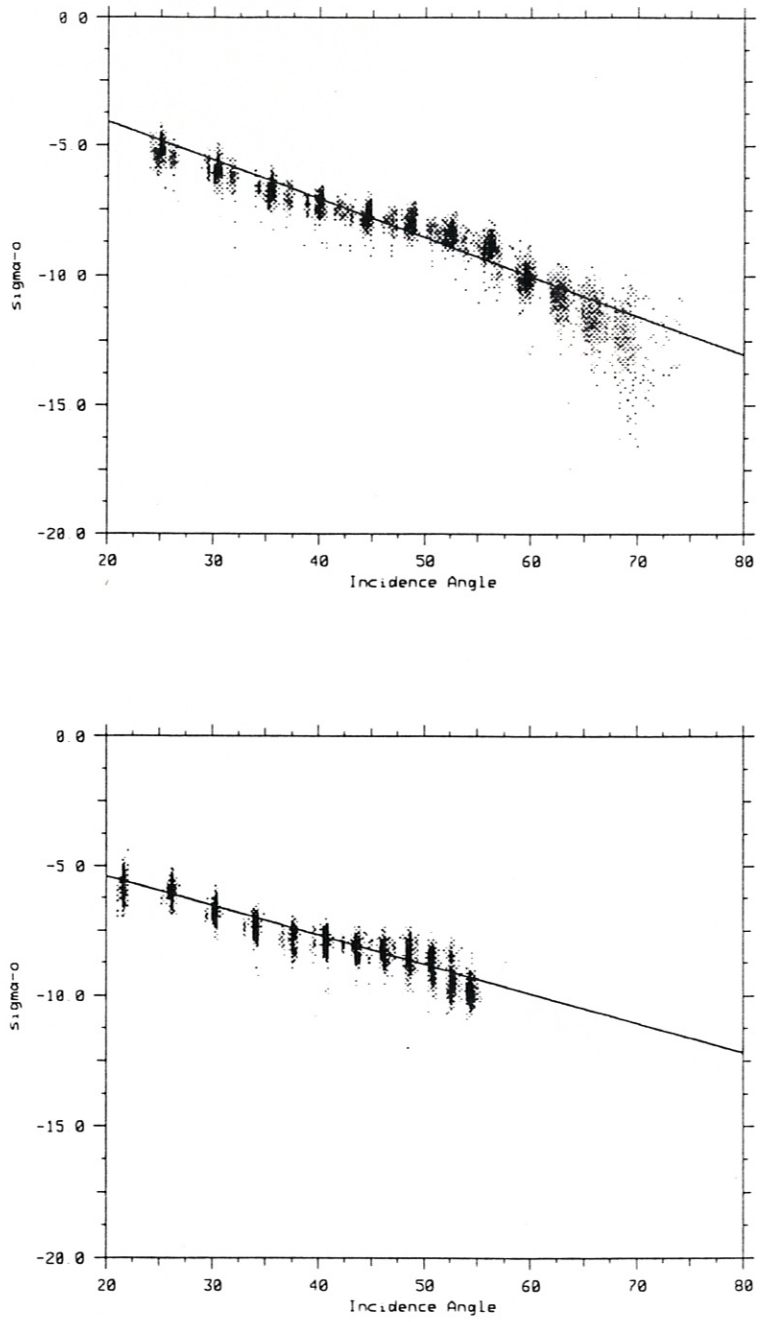

Figure 3.4: Plot of σ° versus θ_i for antenna # 1. (Ascending on top and descending on bottom.)

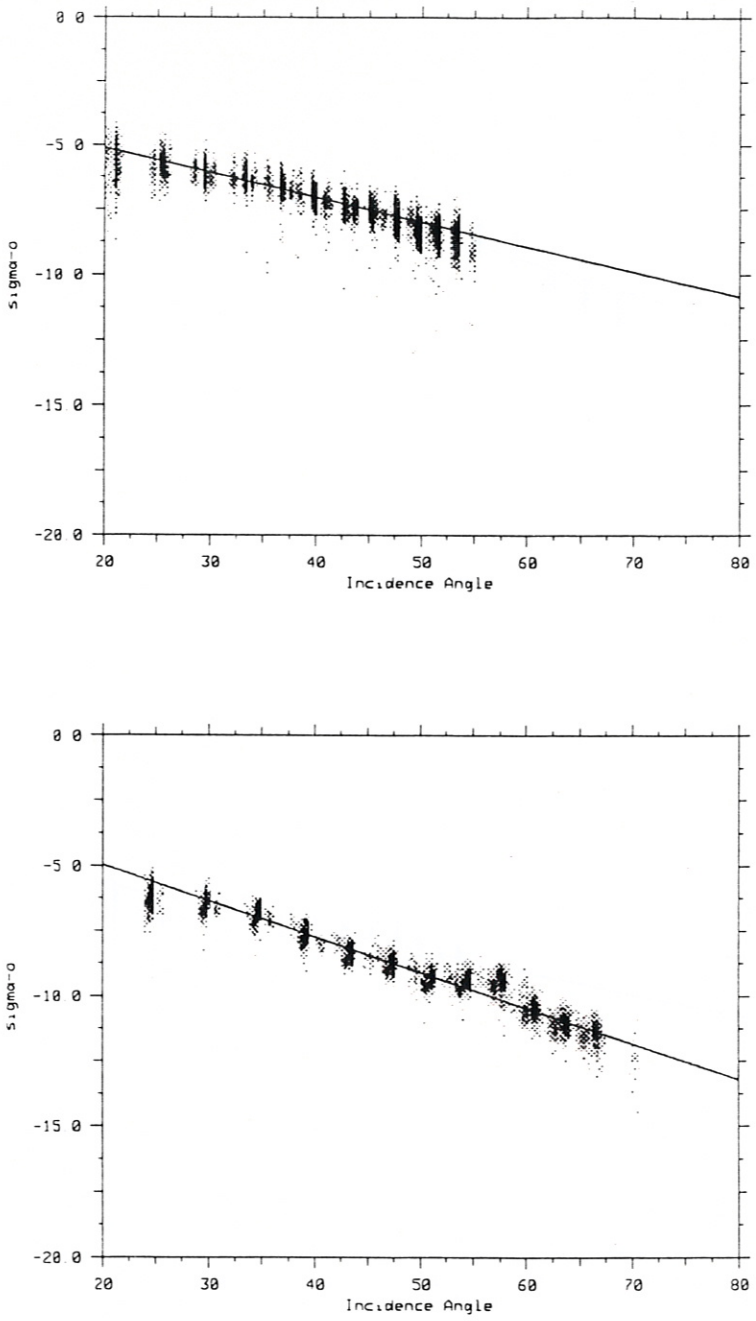

Figure 3.5: Plot of σ° versus θ_i for antenna # 2. (Ascending on top and descending on bottom.)

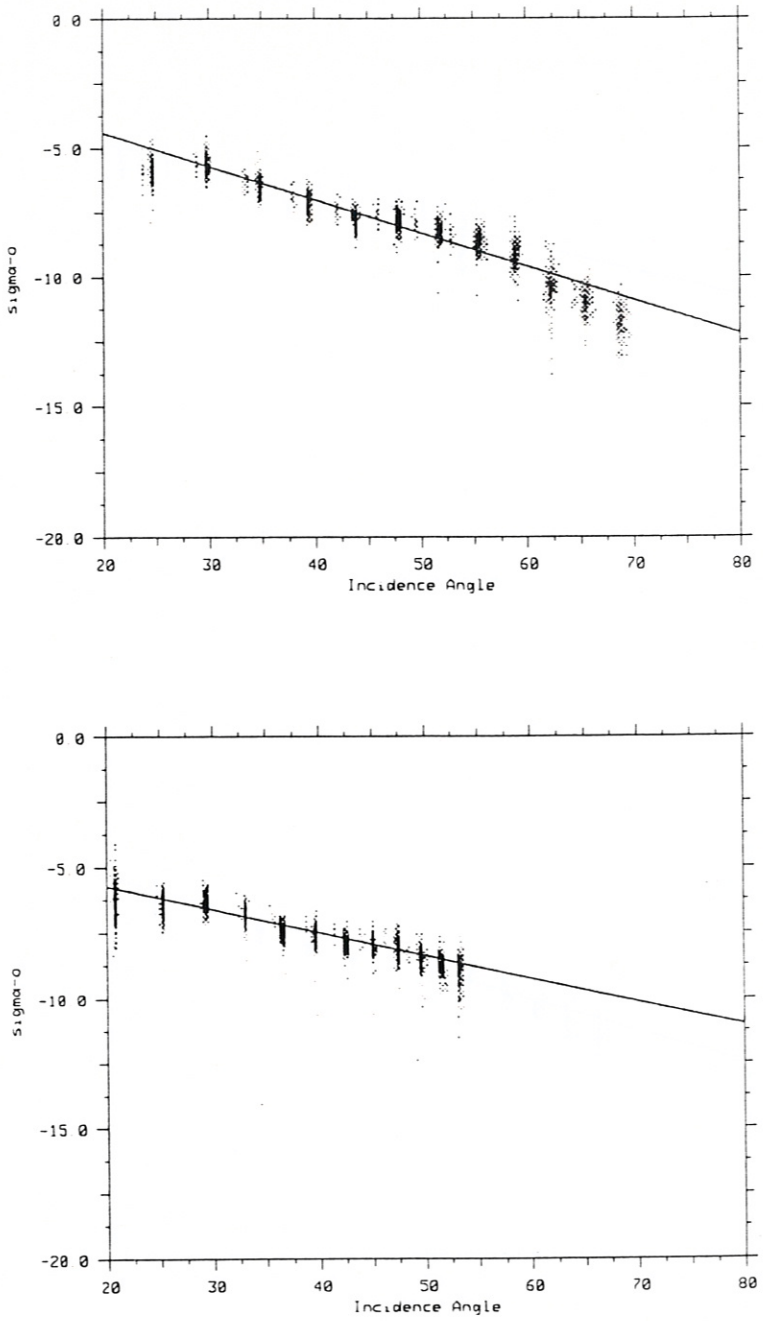

Figure 3.6: Plot of σ° versus θ_i for antenna # 3. (Ascending on top and Descending on bottom.)

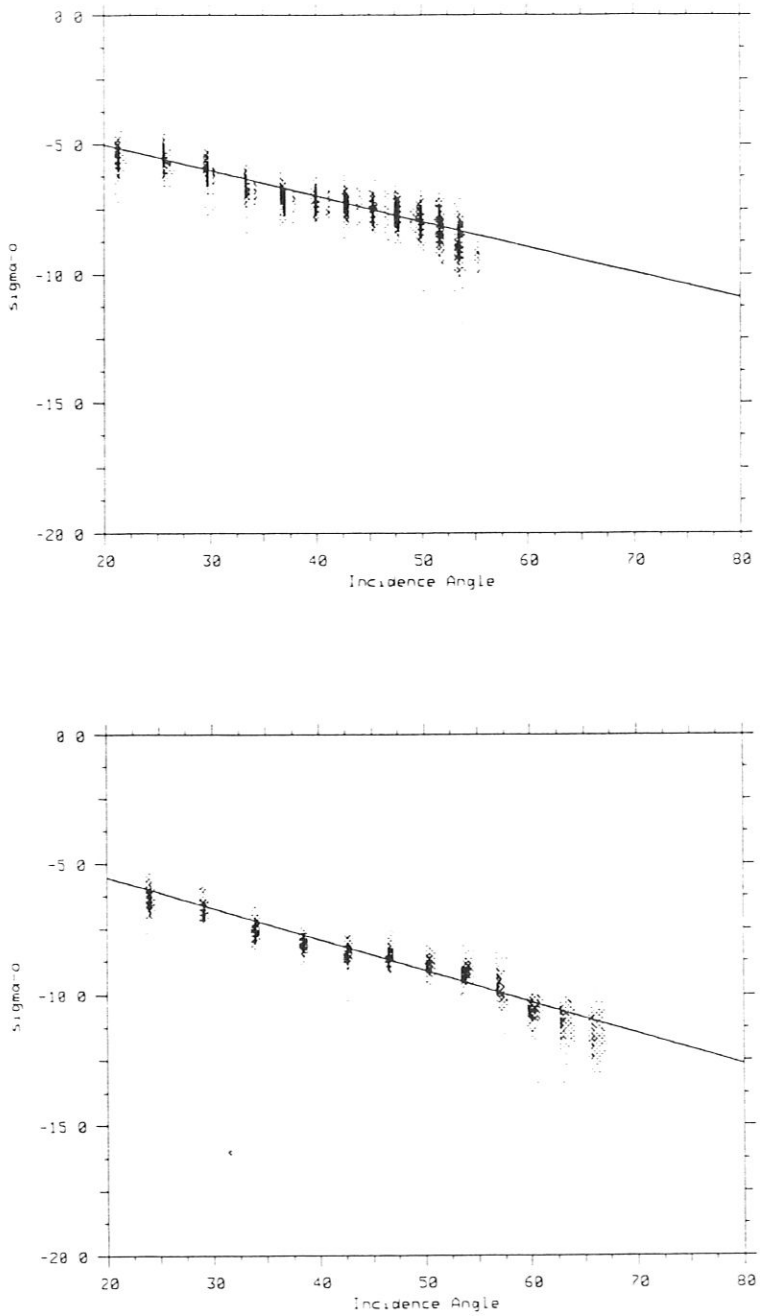

Figure 3.7: Plot of σ° versus θ_i for antenna # 4. (Ascending on top and Descending on bottom.)

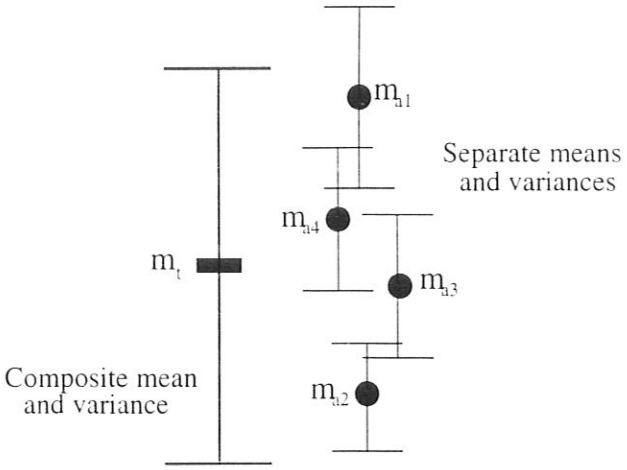

Figure 3.8: Illustration of mean and variance before correction

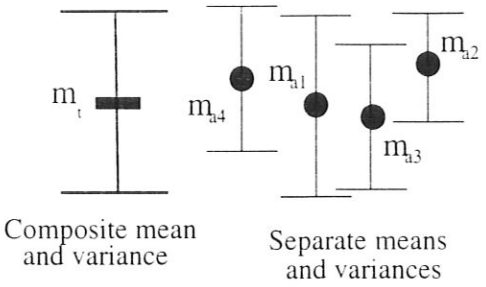

Figure 3.9: Illustration of the mean and variance after the calibration correction has been done

the overall correction is to move the means of the antennas together as in Figure 3.9. Although this will not change the variance of the individual antennas, the variance of the combined measurements will be reduced. Because nothing is done to change the variance of the individual antennas, the actual change in the variance of the total group of measurements depends only upon the change in the means of the different antennas. This is only true for a short time period, where nothing is done to correct for the actual time variability of the measurements from different antennas. When the time variability is removed, the individual variances will also be reduced, thus further reducing the variance of the combined measurements.

3.3 Time Response

Variations in the antenna gain pattern over time will also affect the calibration. In studying the time variability in the SASS data, two time scales are

considered. The first is attributed to the seasonal changes in the land cover. These changes will happen over the period of several days or longer. For example, they may be caused by the change from a wet to a dry season or by a seasonal change in the temperature. The other scale to be considered is the change in the land cover during the day or from morning to night, including changes in the moisture content of the vegetation.

Figure 3.10 shows the average σ° as a function of time for the mission for both the ascending and descending passes. From this figure, a change in the location of the measurements from the beginning to the end of the mission can be seen. This change in the measurement value is attributed to seasonal variations in σ°, which happen slowly over time.

The time-of-day variations in the data are difficult to study because of the limited number of times during the day the scatterometer passes over a given area. In fact the scatterometer will only pass over a given point two times per day. Measurements taken on the ascending passes (satellite travel is from south to north) occur in the morning while measurements taken during the descending passes occur at night. In Figures 3.4 through 3.7, some differences between the ascending and descending passes can be seen in the slope and intercept of the best line fit. Figure 3.11 shows time of day as a function of day number. From this we can see a strong correlation between the time of day and the day number. In accounting for the time varying effects in the SASS data, the measurements are separated by time of day by separating the measurements taken during the ascending passes of the satellite from those of the descending passes. The other changes, which happen over several days or longer, will be attributed to seasonal changes in the land cover and to changes in the instrument.

In order to be able to eliminate the seasonal variations from consideration in the modeling of the measurements, short windows of time are chosen. These time windows are chosen such that the seasonal variations within the window are small. These windows are centered at different times over the mission, which allows the corrections due to seasonal changes to be made.

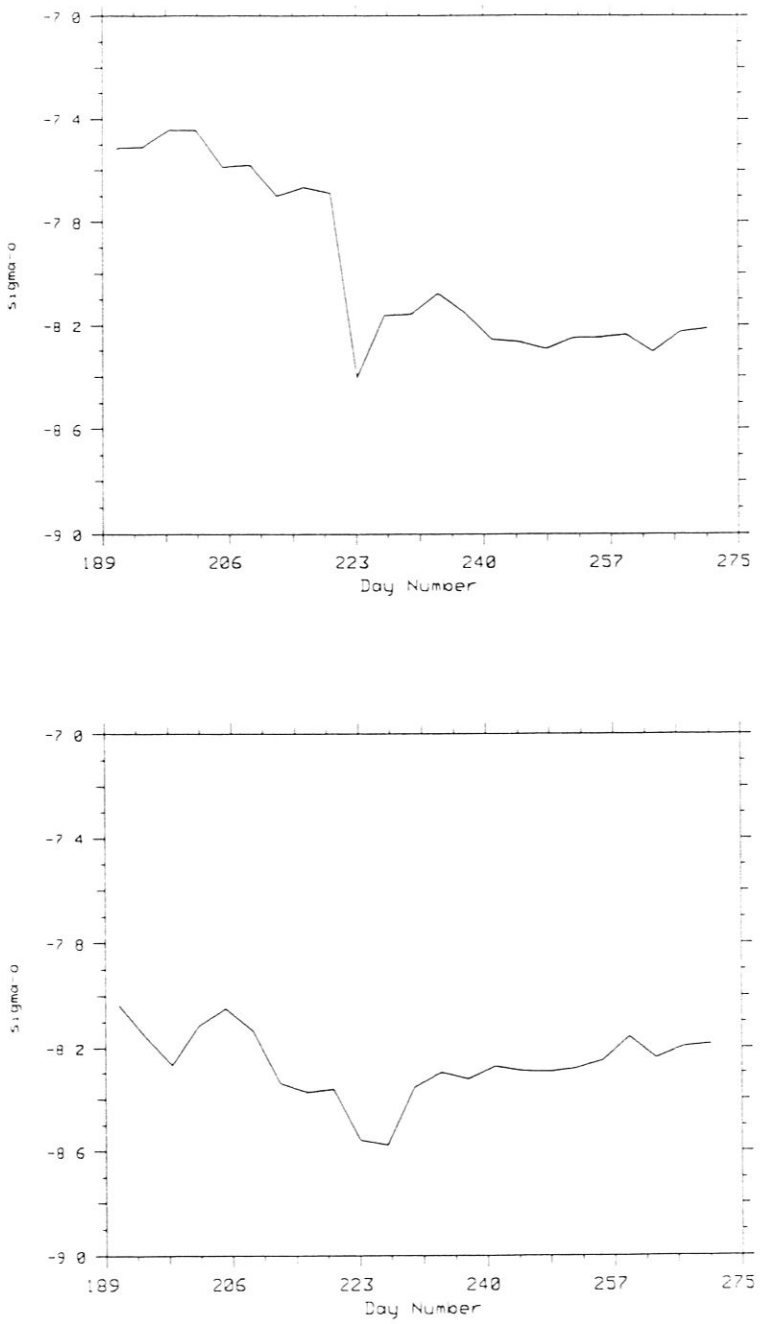

Figure 3.10: σ° values over time. Ascending (top) and descending (bottom)

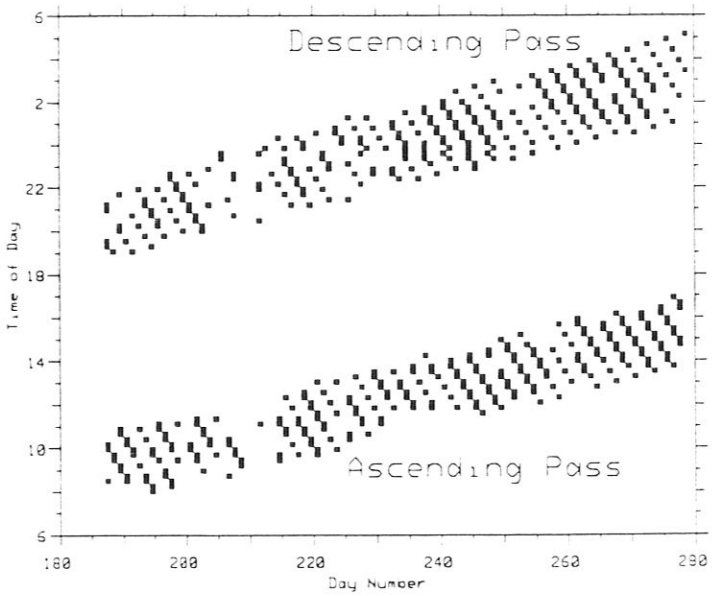

Figure 3.11: Plot of time of day as a function of day number

CHAPTER 4

MODEL DEVELOPMENT

4.1 Introduction

An examination of the data reveals that the σ° measurement is not consistent from antenna to antenna or even from cell to cell using the same antenna. The purpose of this chapter is to determine a model for the instrument measurements. From this model of the measurements, inconsistencies in the data caused by the different antennas and cells can be removed, giving an improved data set. This *recalibrated* data set should be much more useful because of the consistency of the data from antenna to antenna and from cell to cell.

Errors between the recorded σ° measurements and the actual σ° of the land cover are partly due to the noise in the transmit/receive medium and the differences in the antennas and the processing done on the measurements. One of the complicating factors in being able to remove these errors is that the response of the surface (σ°) is not constant during the mission. In order to better understand the recorded data and to be able to better understand which of the variations in the data are caused by the antennas, a model will be developed for the recorded measurements, including the inconsistencies. This will make it possible to remove the errors caused by the instrument and processing while preserving the usefulness of the time-varying data.

4.2 Model Method

As stated above, the recorded value of σ° not only contains the response of the surface being measured, but also information from the instrument and processing. The general equation relating the recorded measurement (in dB) can be written as:

$$z_n = \sigma^\circ_L\left(Loc_n, time_n, \theta_{in}\right) + G_{INST}\left(time_n, Beam_n, cell_n, \theta_{in}\right) + noise_n \qquad (4.1)$$

where z_n is the n^{th} measurement stored in the SASS GDR (geophysical data record), $\sigma^\circ_L()$ is the actual response of the land cover, and where $G_{INST}()$ contains

all of the effects added by the antenna and the instrument gain errors. Independent variables are listed in Table 4.1. In this report, all measurement and σ° values are assumed to be in dB unless otherwise stated.

Variable	Description
Loc	Location of measurement (latitude/longitude)
$time$	Time of measurement
θ_i	Incidence angle to cell
$Beam$	Antenna beam number
$cell$	Cell number

Table 4.1: Variable descriptions for variables of Equation 4.1

A data set made by choosing a constant σ° mask as described in the previous chapter will be used to eliminate the location dependence of z_n. By separating the antennas into ascending and descending tracks and choosing a time window sufficiently small to avoid differences due to seasonal changes, the land dependency can be modeled as being only a function of incidence angle, and time can be eliminated as a variable in G_{INST}. Ignoring noise, Eq. 4.1 can be written as:

$$z_n = \sigma_L^\circ(\theta_{in}) + G_{INST}(Beam_n, cell_n, \theta_{in}) \tag{4.2}$$

or

$$z_n = \mathcal{F}(\theta_{in}, cell_n, beam_n, Asc/Des_n) \tag{4.3}$$

where $\mathcal{F}$ is the model function to be determined. In this case the actual value of the land cover response will not be found but will be determined as the mean response of all antennas. The estimation of the model is greatly simplified by eliminating the time and location dependence of the problem.

4.3 Model Parameters

The processing of the measured σ° can be modeled as shown in Figure 4.1. This figure shows the three main stages of the processing. These are: the absolute gain stage (G_{AB}), the separated antenna stage (G_{SA}) and the separated cell stage (G_C). In the absolute gain stage, the same gain is given to all of the

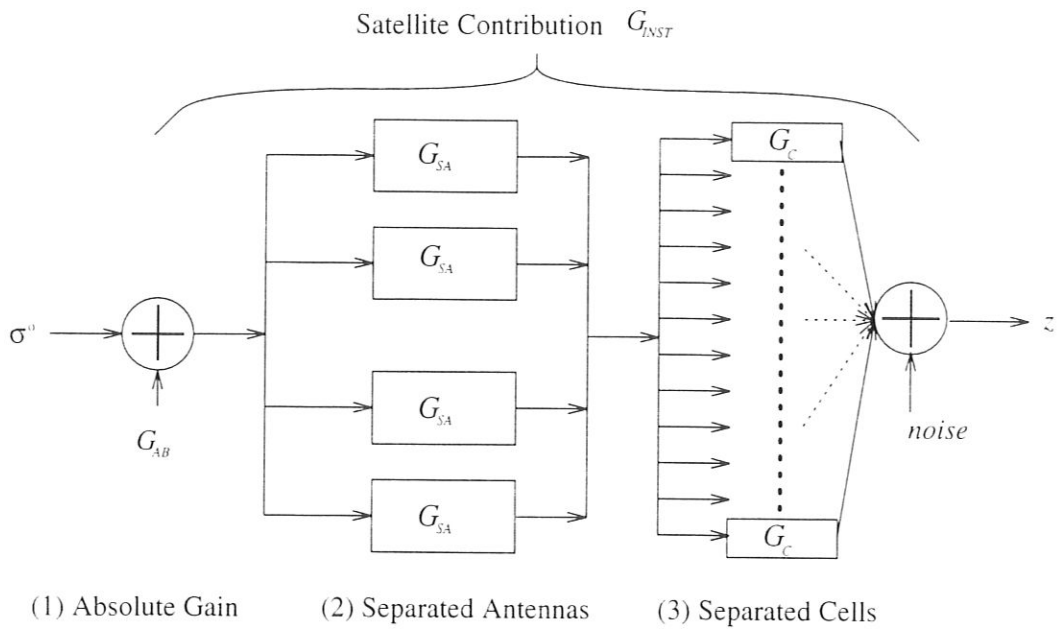

Figure 4.1: Diagram of the processing model

signals, regardless of which antenna or cell is being used. Thus, the absolute gain (G_{AB}) will not have any effect on the relative error between measurements. In addition, this absolute gain is not obtainable from the data and will not be considered further in this report. As described in Chapter 1, the antenna illumination is split into resolution cells using Doppler filtering. In this stage of the processing, the signal is filtered and amplified on a cell by cell basis. Because of differences in the filters used, biases exist between the gain at each cell, due to the differences in the actual and assumed gain of the filters.

From the plots of the measurements z_n versus θ_i (Figures 3.4 - 3.7) we see that the data fits fairly well to a line at angles between 30° and 50°. At extreme angles, the linear model doesn't fit the data as well. However, the data is still quite smooth and a polynomial model should fit quite well. We assume a decomposition of $\mathcal{F}$ as:

$$\mathcal{F} = F\left(\theta_{in}, beam_n, Asc/Des_n\right) + G_C\left(cell_n\right) \tag{4.4}$$

where F is a model of the σ° response curve with respect to θ_i and G_C is the cell gain correction.

Order	2		3		4		5	
Beam	σ	$r^2(\%)$	σ	$r^2(\%)$	σ	$r^2(\%)$	σ	$r^2(\%)$
Asc. 1	0.0785	88.9	0.0665	92.0	0.0662	92.1	0.0853	92.8
Asc. 2	0.0872	73.4	0.0862	73.7	0.0862	73.7	0.0853	74.3
Asc. 3	0.0688	87.4	0.0676	88.3	0.0640	89.5	0.0598	90.8
Asc. 4	0.0916	71.7	0.0885	73.6	0.0842	76.1	0.0842	76.1
Des. 1	0.0961	61.0	0.0929	63.6	0.0899	65.9	0.0895	66.2
Des. 2	0.0809	88.0	0.0809	88.0	0.0776	89.0	0.0723	89.1
Des. 3	0.0932	57.6	0.0927	58.2	0.0913	59.4	0.0908	59.9
Des. 4	0.0828	83.0	0.0783	84.8	0.0783	84.8	0.0762	85.6

Table 4.2: Standard deviation of the model error using different orders of polynomials for the model

4.4 Selecting Polynomial Order

In order to model the σ° measurements with a polynomial, it has been noted that a linear model is not sufficient. To select an appropriate polynomial order for the model, the fit error for different polynomial models will be examined. These errors, along with the r^2 parameter[1], give an indication of how much improvement should be gained from the use of one model order as compared to another. Because experimental plots show the measurements are relatively well behaved, a low order polynomial should be adequate for this model.

Polynomials of different orders were used as a model for σ° versus θ_i (see Figures 3.4 through 3.7). Table 4.2 shows the standard deviation of the model error and the r^2 parameters for a polynomial regression for each of the antennas on ascending and descending passes. From this table, no single model is best. In some cases the third order model seems to be good enough; however, in other cases the fourth order model is clearly an improvement. For the work here, a fourth order model will be used.

Using a fourth order polynomial Eq. 4.4 can be written as

$$z_{jkl} = a_{jl} + b_{jl}\theta_{in} + c_{jl}{\theta_i}^2 + d_{jl}{\theta_i}^3 + e_{jl}{\theta_i}^4 + G_{Ck} \tag{4.5}$$

[1]The r^2 parameter is a measure of the percentage of the variation about the mean explained by the regression

where j represents the antenna number (1 - 4), k is the cell number (1 - 12) and l is one for ascending and two for descending.

CHAPTER 5

MODEL PARAMETER ESTIMATION

Estimation of the model parameters will be considered in two parts, the antenna parameters F and the cell gains G_C. In doing this, it is necessary to assume that the polynomial parameters and the cell gain parameters are independent. Because these parameters represent different parts of the system, it is not unreasonable to assume independence. These antenna parameters will be estimated first because of the lower order of the model. This will leave the higher order terms to be explained by the cell gains. If the cell gains were to be estimated first, some of the lower order responses due to the antenna parameters may be included in the cell gain parameters. Also, the antenna parameters and the land cover is much more likely to have time changes than are the cell gains. This is because of the temperature sensitivity of the antennas and the seasonal changes in the land cover. The bandpass filters should have a smaller fluctuation with respect to time.

5.1 Polynomial Parameter Estimation

The approach used in estimating the model parameters is least-squares. Ignoring the cell contributions for the moment, Eq. 4.5 can be written as:

$$z_{jl} = a_{jl} + b_{jl}\theta_i + c_{jl}\theta_i^2 + d_{jl}\theta_i^3 + e_{jl}\theta_i^4 \tag{5.1}$$

In order to increase the accuracy of the numerical estimate, the parameters are scaled to have similar magnitudes. Without loss of generality, variable substitutions can be made in Eq. 5.1. Here we will use

$$\vartheta = \frac{\theta_i - 40^\circ}{10} \tag{5.2}$$

and

$$\begin{aligned} A_{jl} &= a_{jl} \\ B_{jl} &= 10b_{jl} \end{aligned}$$

$$\begin{aligned} C_{jl} &= 100c_{jl} \\ D_{jl} &= 1000d_{jl} \\ E_{jl} &= 10000e_{jl} \end{aligned} \tag{5.3}$$

so that

$$z_{jl} = A_{jl} + B_{jl}\vartheta + C_{jl}\vartheta^2 + D_{jl}\vartheta^3 + E_{jl}\vartheta^4 \tag{5.4}$$

Writing this in matrix form we have:

$$Z_{jl} = M_{jl}\vec{x}_{jl} \tag{5.5}$$

where

$$Z_{kl} = \begin{bmatrix} z_{1jl} \\ z_{2jl} \\ \vdots \\ z_{N_m jl} \end{bmatrix} \tag{5.6}$$

$$\vec{x}_{jl} = \begin{bmatrix} A_{jl} \\ B_{jl} \\ C_{jl} \\ D_{jl} \\ E_{jl} \end{bmatrix} \tag{5.7}$$

$$M_{jl} = \begin{bmatrix} 1 & \vartheta_1 & \vartheta_1^2 & \vartheta_1^3 & \vartheta_1^4 \\ 1 & \vartheta_2 & \vartheta_2^2 & \vartheta_2^3 & \vartheta_2^4 \\ \vdots & \vdots & \vdots & \vdots & \\ 1 & \vartheta_N & \vartheta_N^2 & \vartheta_N^3 & \vartheta_N^4 \end{bmatrix} \tag{5.8}$$

and j and l are as before, the antenna number and whether it is ascending or descending; N is the total number of measurements used. For the problem here, N is quite large and covers several incidence angles, insuring that M_{jl} is full rank.

We will use the least squares method to solve for the parameter vector $\vec{x}$, so that

$$\vec{x}_{jl} = \left(M_{jl}^T M_{jl}\right)^{-1} M_{jl}^T Z_{jl}. \tag{5.9}$$

5.2 Cell Gain Bias Estimation

In estimating the cell gain bias, it is first necessary to find the residual error from the polynomial model parameters. The cell gain bias estimation will be based on the amount of error existing from the polynomial model. To find this we define $Zcor$ as:

$$Zcor_n = z_n - \mathcal{F}\left(\theta_n, cell_n, beam_n, Asc/Des_n\right), \tag{5.10}$$

where $\mathcal{F}$ is the same as in Eq. (4.3), and the z_n or $Zcor_n$ are separated by cell number. This correction error should be relatively small, as long as the polynomial model is good. The estimate of the cell gain bias for each of the parameters is calculated by averaging the error for each cell, as:

$$G_{Ck} = \frac{\sum_{n=1}^{N_k} Zcor_n g_k(n)}{N_k}, \tag{5.11}$$

where

$$g_k(n) = \begin{cases} 1 & \text{if the } n^{th} \text{ measurement is from cell } k \\ 0 & \text{otherwise} \end{cases}, \tag{5.12}$$

G_{Ck} is the cell gain bias parameter for the k^{th} cell, and N_k is the number of measurements made from the k^{th} cell. The vector $Zcor$ should be close to zero. This cell gain correction will take care of any of the cells that tend deviate from the desired zero value.

The estimation of both the cell gain bias and the polynomial fit to the measurements will give a close approximation to the actual data. By using this model, the data can be *corrected* so that it will be much more consistent from antenna to antenna and from cell to cell.

5.2.1 Window Length Determination

In selecting the length of the time window to be used in the parameter estimation problem, it is important to consider the tradeoffs. If the time window is too large, time variations of the instrument and land cover will not be seen by the parameter calculation. Thus the model will not adequately describe these changes. However, if the window is too small, the parameter estimation may yield

Window size (days)	Error
1	0.378
2	0.101
4	0.093
5	0.105
6	0.107
7	0.105
8	0.101
10	0.105
12	0.114
15	0.113
16	0.109
20	0.115

Table 5.1: This table shows the mean squared error for different window sizes

poor quality estimates, due to the small number of measurements being used in the parameter calculation. In order to pick a good window length, model parameters for one of the antennas were calculated using several window lengths. Using this estimate, the mean squared model error was calculated, where

$$e = \sum_{n-1}^{N} (z_n - \hat{z}_n)^2 \tag{5.13}$$

is the squared error of the measurement z_n and the predicted value $\hat{z}_n$, where the total number of measurements is N. Sample results can be found in Table 5.1. From this table, it can be seen that the window length has only a small effect on accuracy, as long as the window length is large enough to include enough measurements. Although the window length of four days gives the minimum error, if the one day window is ignored, the difference in the individual errors is less than one percent of the average error.

Because the window length has only a limited effect on the model error, an alternate method of deciding on the size for the window is considered. In this approach the variation in the parameter are examined. Figure 5.1 shows the dominant model parameter, A, representing the average value of σ°. These figures use window lengths of four, eight and sixteen days, with window centers at one day intervals. From these plots, it is noted that the variations in the

parameter value using the four-day window are at a much higher frequency than those using longer windows. The four day window length also has difficulty in estimating the parameters from day 205 to 207 because of the small number of measurements in this time period. In effect, the larger window length acts as a low-pass filter. However, the sixteen day window seems to smooth out the sharp jump occurring at day 220. Because it is assumed that the seasonal variability in the surface vegetation is slowly varying, short term variations are attributed to noise. Hence, a window length of eight days will be used because of the good combination of the small susceptibility to errors in the measurements, while not filtering the measurements heavily.

Using this approach, the model parameters have been calculated and are shown in Figures 5.2 through 5.7. As expected, the A parameters show quite a bit more variation over the time period than do the cell gain parameters. Figures 5.8 through 5.11 show the measurement model as a function of incidence angle and time for each antenna. Note that due to the small number of measurements taken around day number 210, there are sharp points in some of the plots (Figures 5.2 through 5.11).

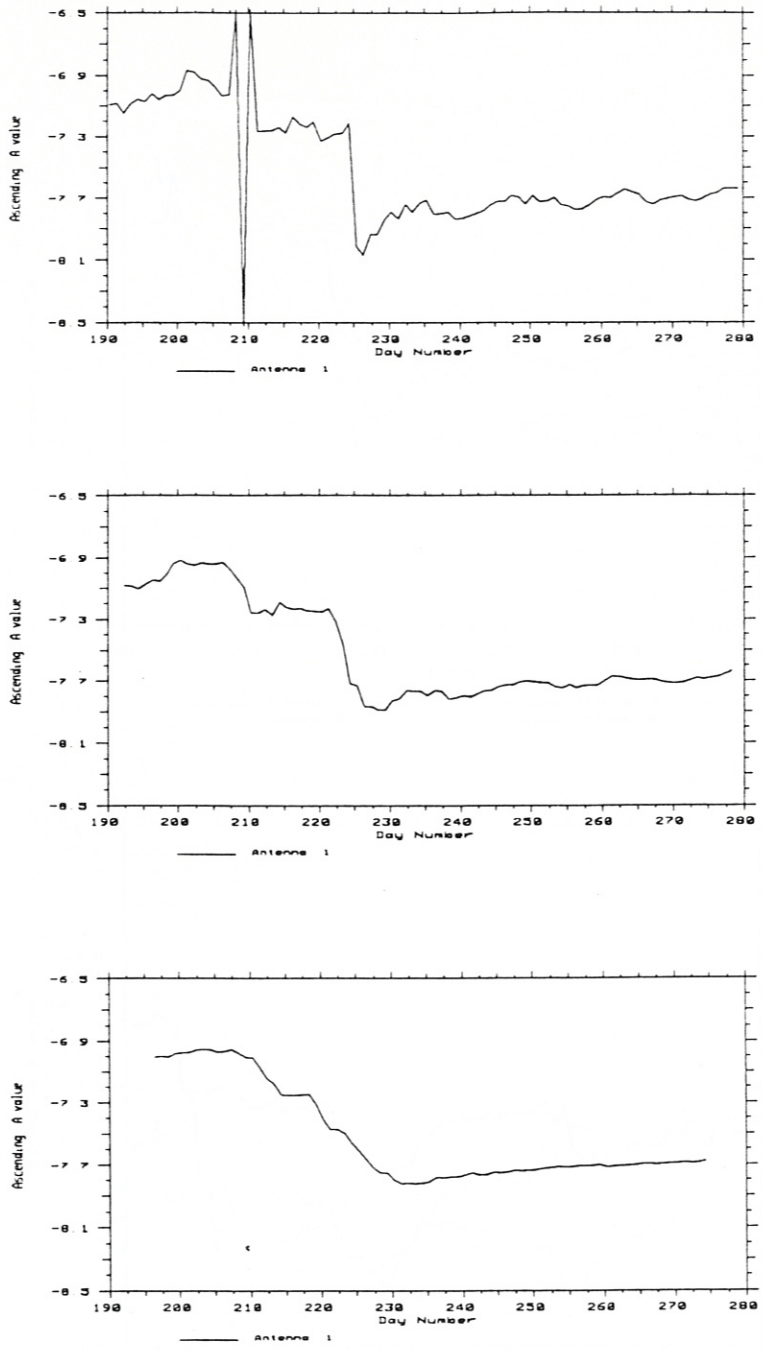

Figure 5.1: This shows the constant term from a polynomial fit using four, (top) eight (middle) and sixteen (bottom) day time windows

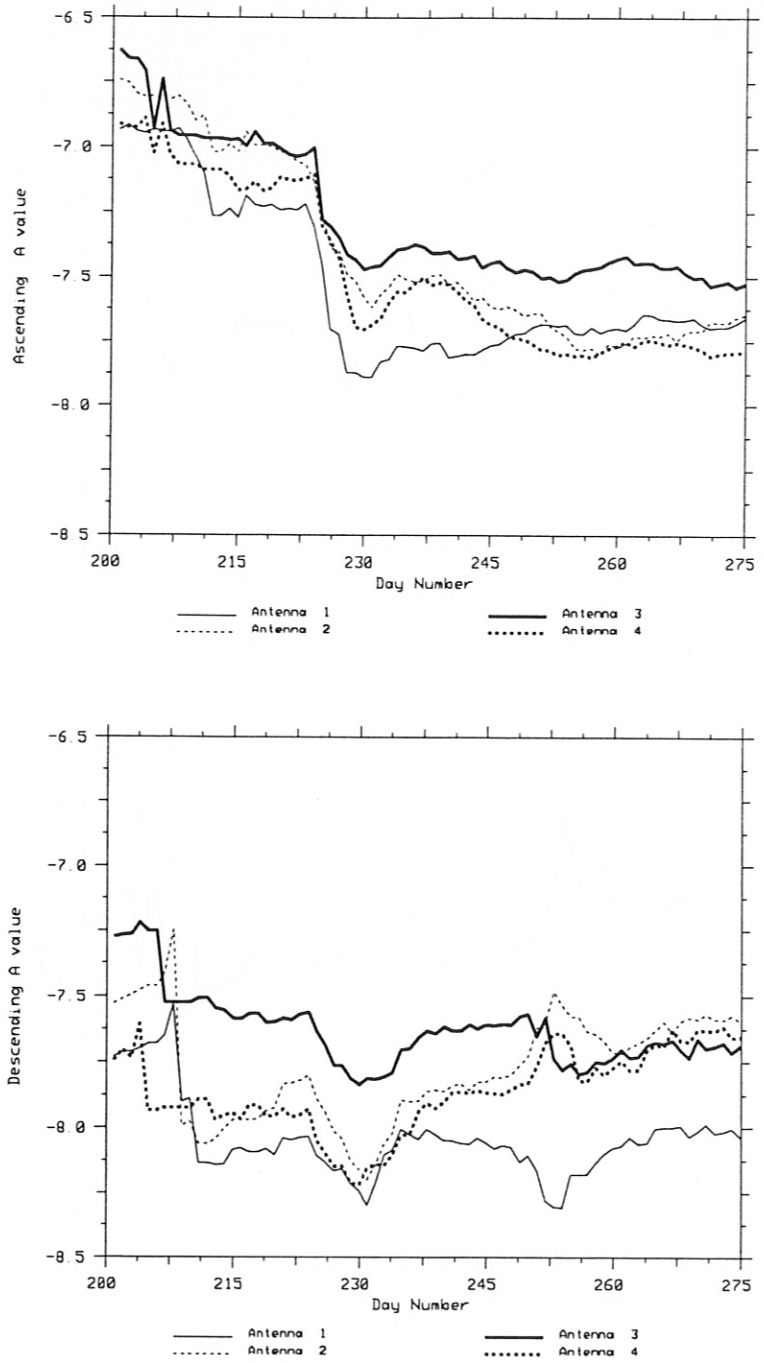

Figure 5.2: Model A parameters for ascending (top) and descending (bottom) passes

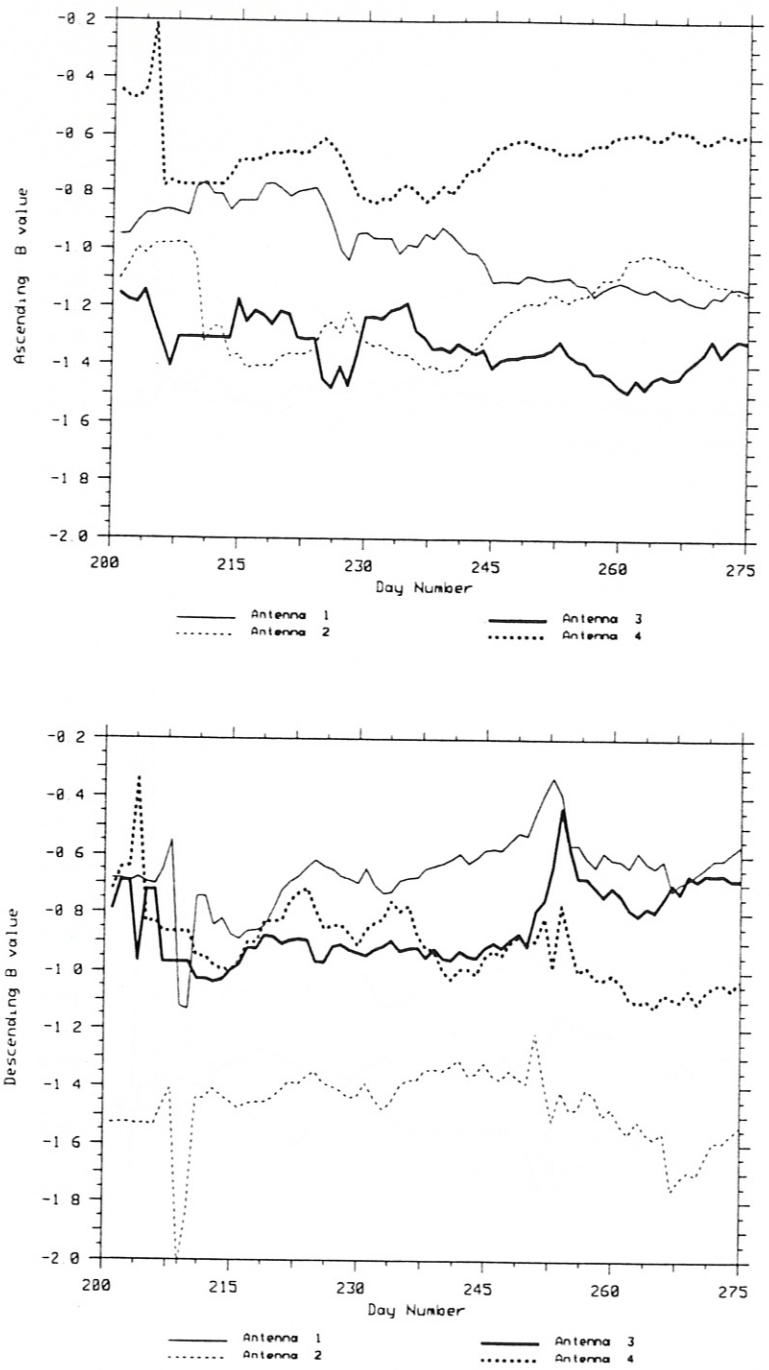

Figure 5.3: Model B parameters for the ascending (top) and descending (bottom) passes

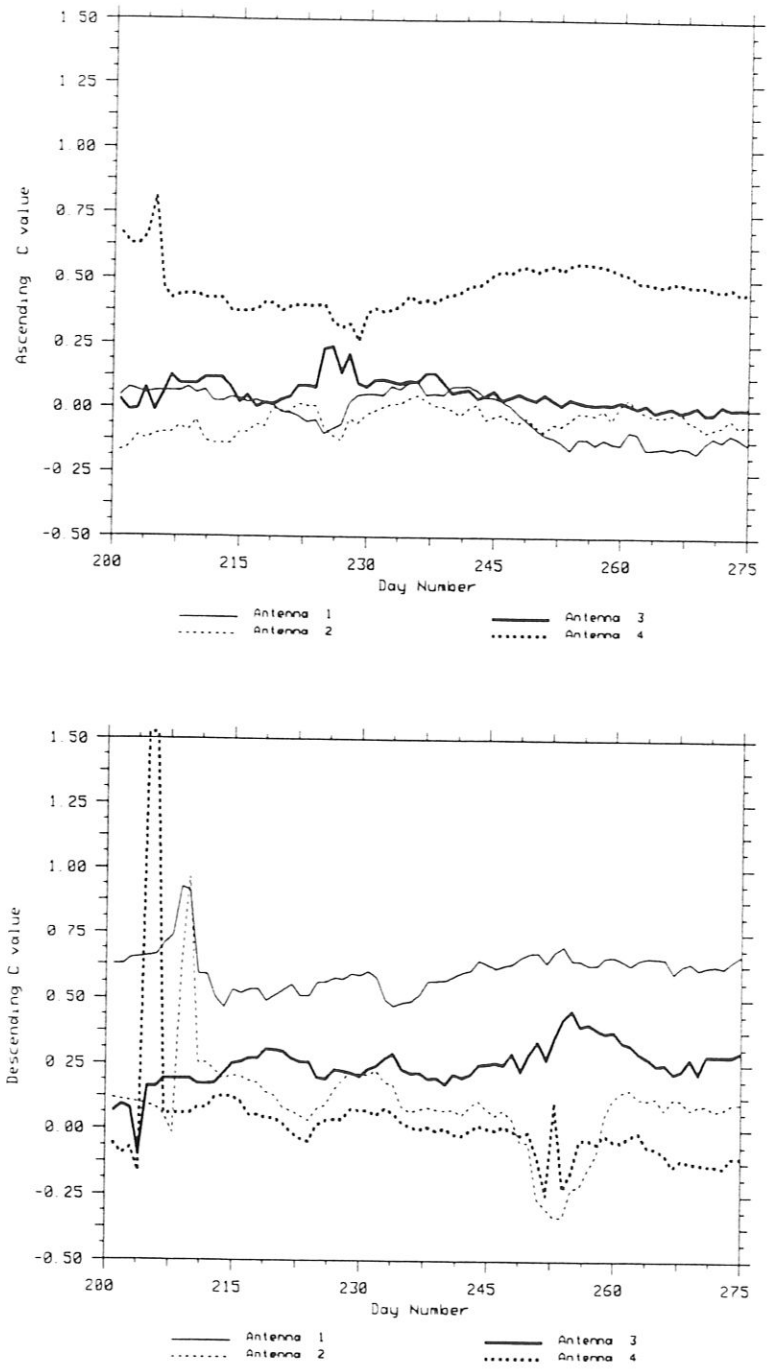

Figure 5.4: Model C parameters for the ascending (top) and descending (bottom) passes

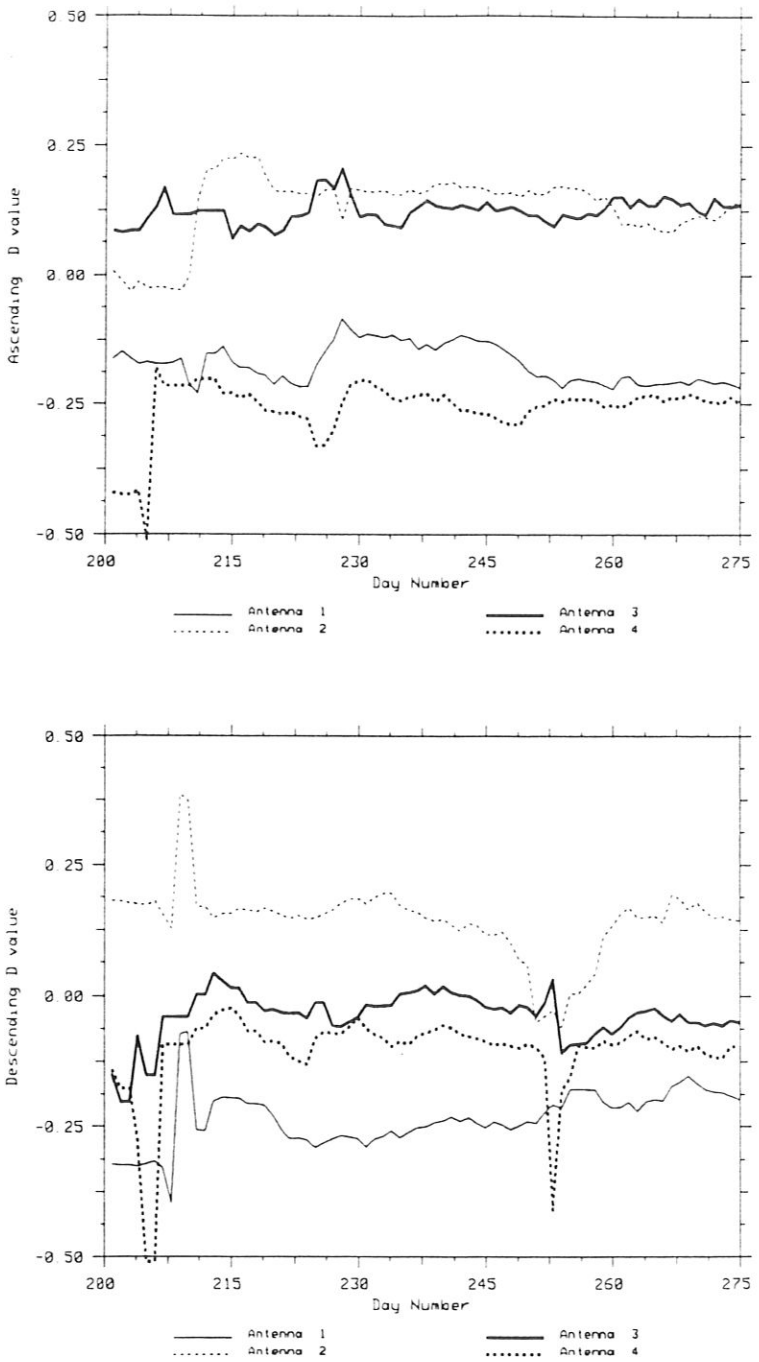

Figure 5.5: Model D parameters for the ascending (top) and descending (bottom) passes

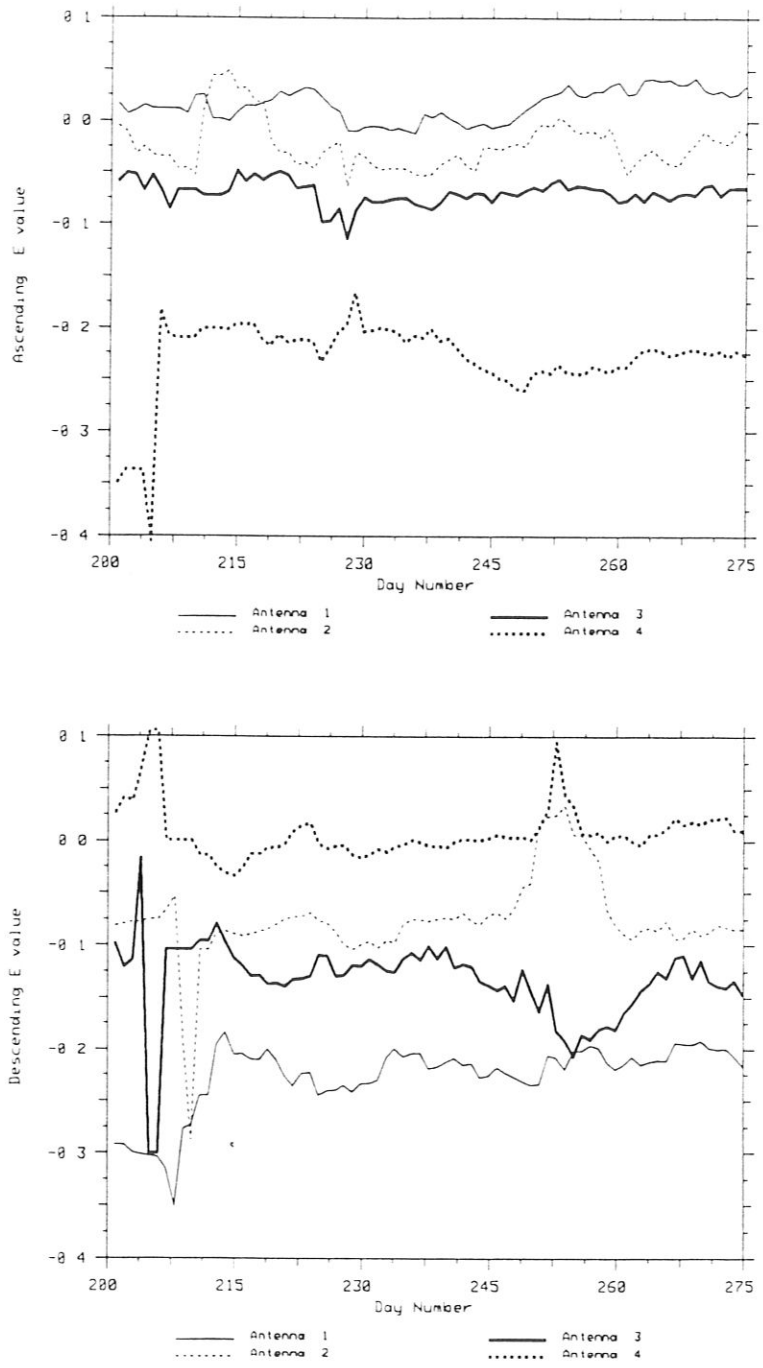

Figure 5.6: Model E parameters for the ascending (top) and descending (bottom) passes

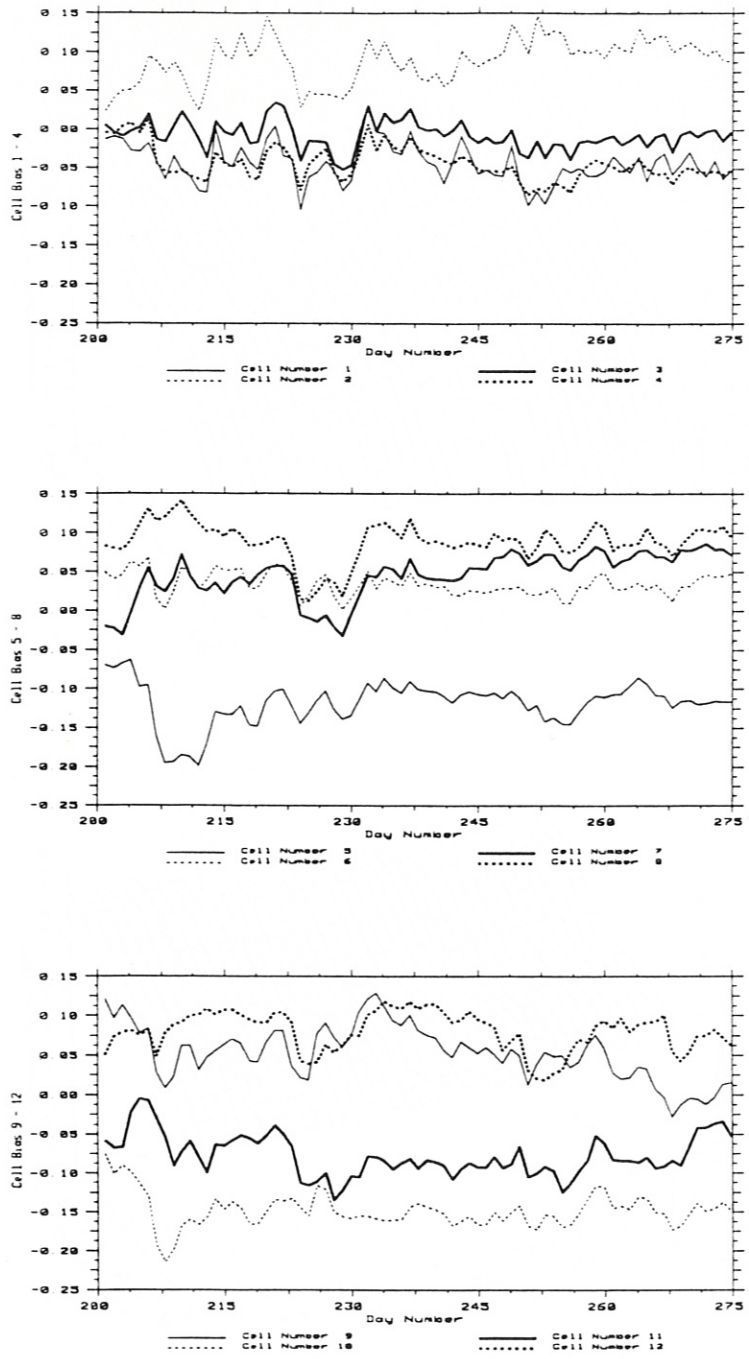

Figure 5.7: Model cell gain bias parameters. Top, cells 1 - 4, center, cells 5 - 8 and bottom cells 9 - 12.

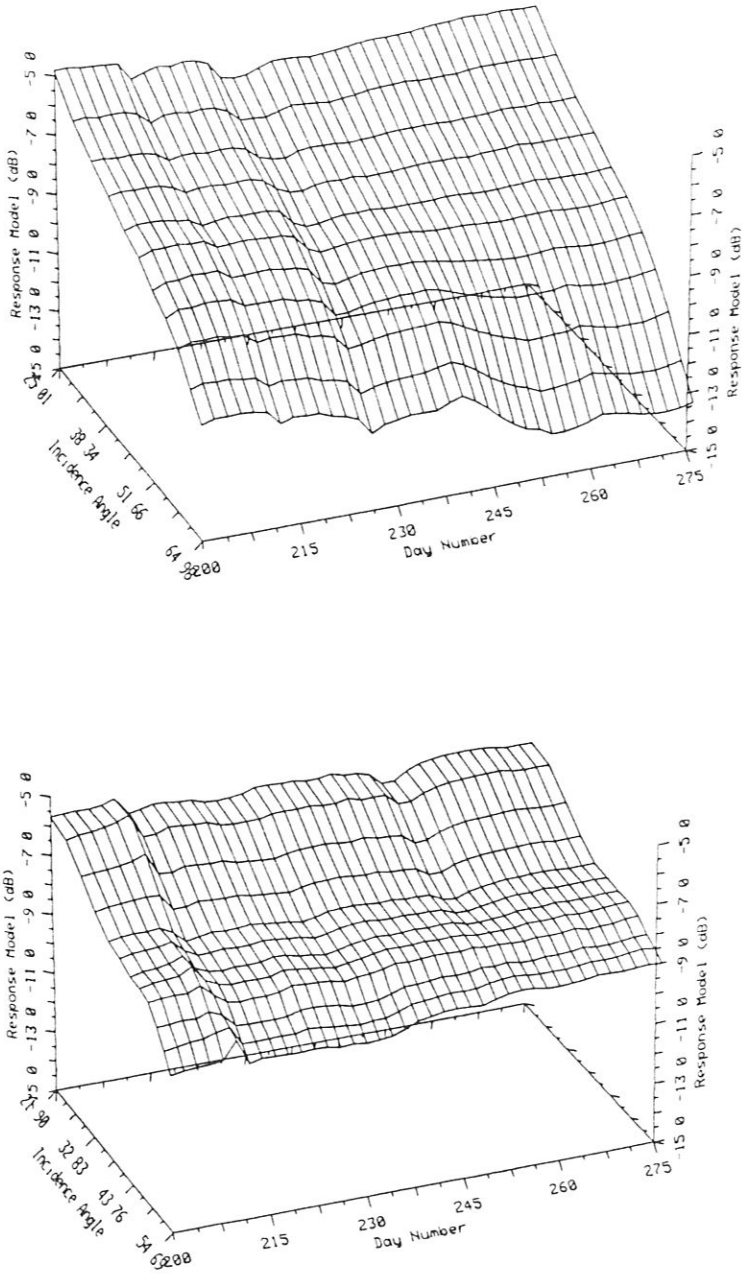

Figure 5.8: Measurement model for antenna 1 ascending (top) and descending (bottom)

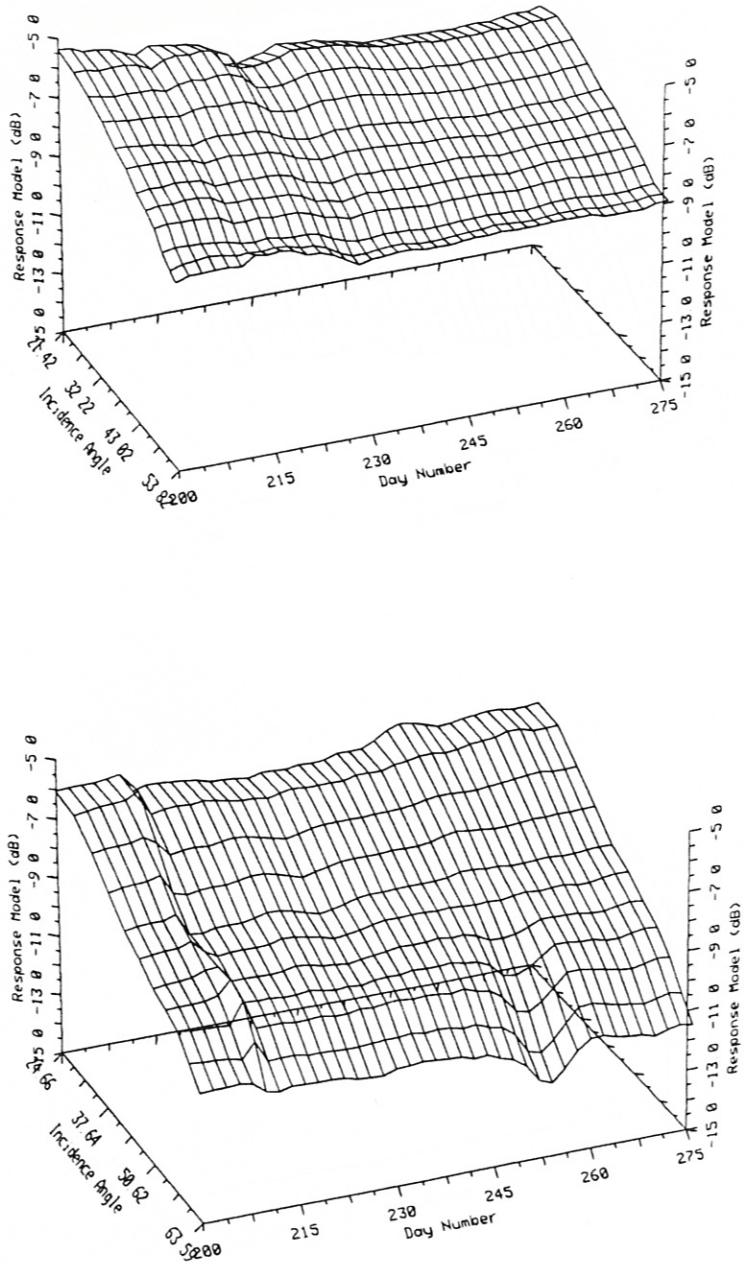

Figure 5.9: Measurement model for antenna 2 ascending (top) and descending (bottom)

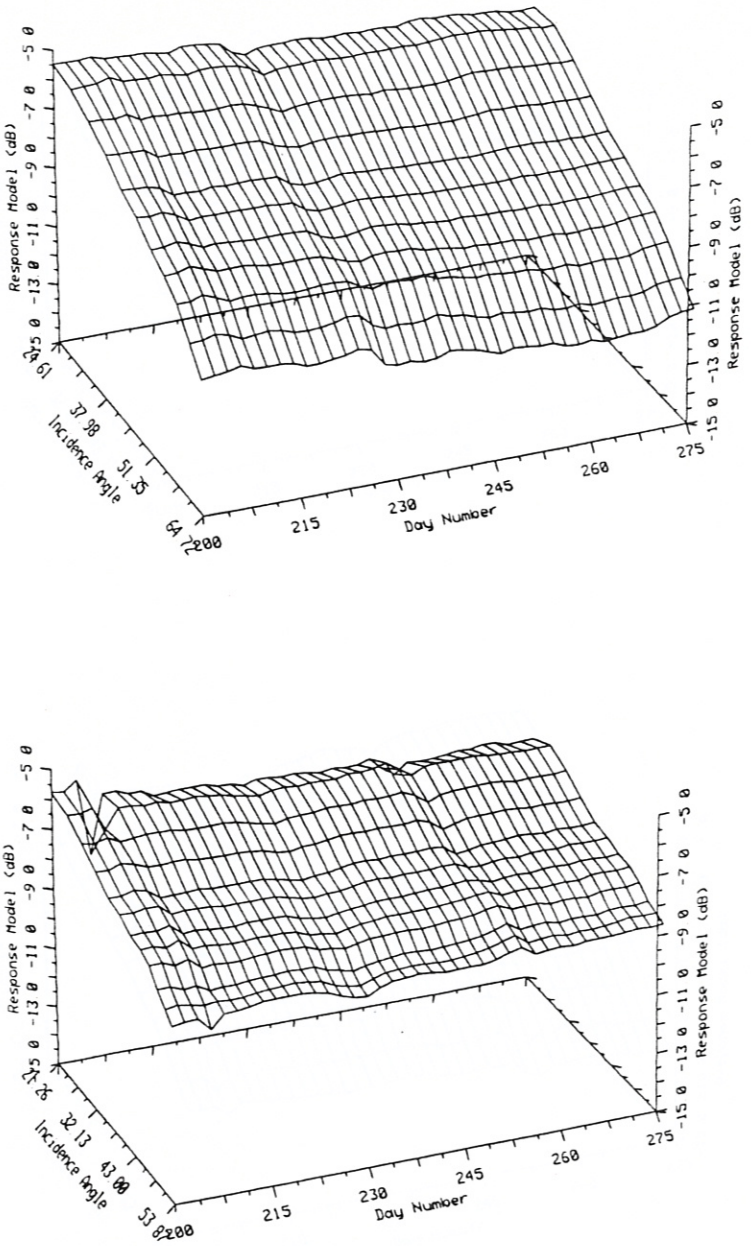

Figure 5.10: Measurement model for antenna 3 ascending (top) and descending (bottom)

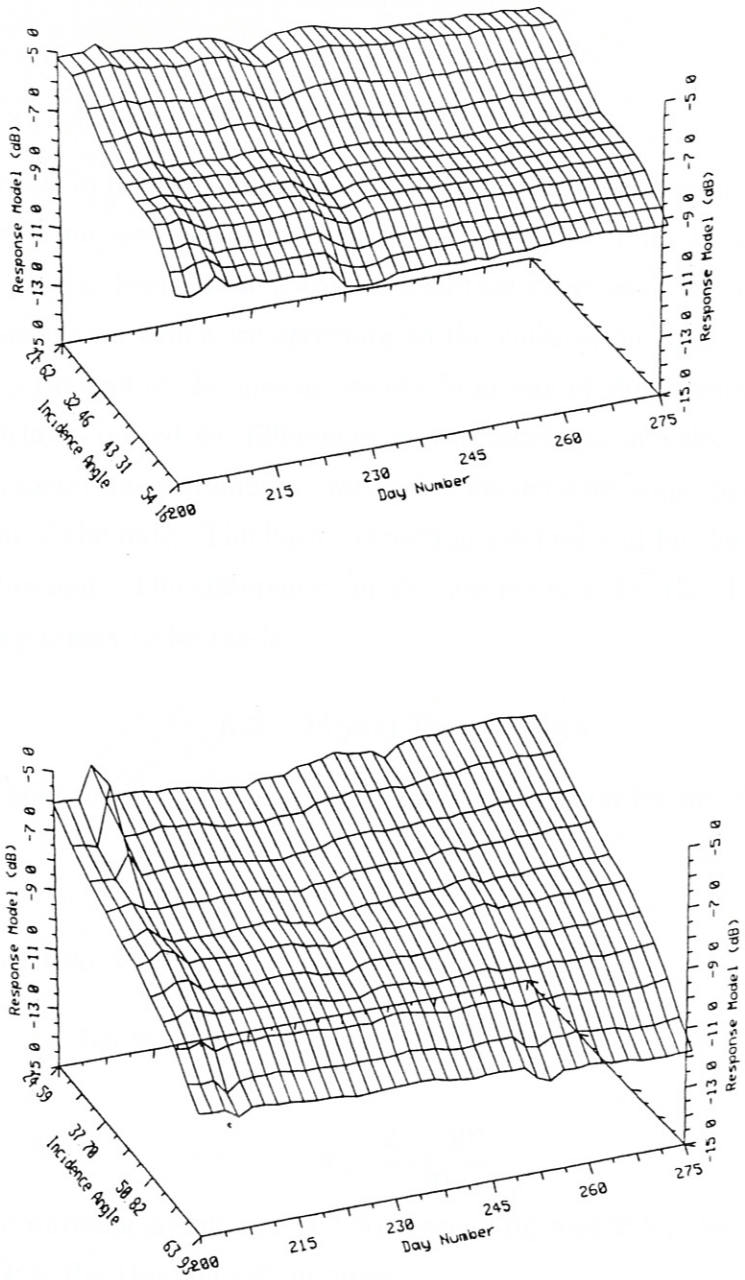

Figure 5.11: Measurement model for antenna 4 ascending (top) and descending (bottom)

CHAPTER 6

CORRECTION METHOD

6.1 Introduction

Plots of the polynomial and cell gain parameters as a function of window position over time are shown in Figures 5.2 through 5.7 for both ascending and descending passes. From these it can be seen that there are variations between the different parameters which we attribute to the calibration errors. A correction is necessary, so that all of the measurements from any of the antennas may be used together without regard to differences in the antennas or cells. After modeling the scatterometer measurements, we now consider the steps necessary to do a recalibration of the data. The basic correction method will be the same regardless of the application. The differences in the application for the data may require different corrections to be made.

6.2 Model Parameters

From the previous chapter, the model equation for the σ° measurements z is:

$$z_n = F\left(\theta_{in}, beam_n, Asc/Des_n\right) + G_{Ck} \tag{6.1}$$

which was written as

$$z_{jkl} = A_{jl} + B_{jl}\vartheta + C_{jl}\vartheta^2 + D_{jl}\vartheta^3 + E_{jl}\vartheta^4 + G_{Ck} \tag{6.2}$$

where

$$\vartheta = \frac{\theta_i - 40^\circ}{10} \tag{6.3}$$

and j is the antenna number, l is 1 for ascending and 2 for descending antenna passes and k is the Doppler cell number.

Table 6.1 shows some sample model parameters calculated using the method described in the previous chapter. These parameters were estimated using an eight-day time window centered at day number 230. The cell gain parameters are shown in Table 6.2.

Beam #	Asc./Des.	A	B	C	D	E
1	Asc.	-7.89	-0.940	0.056	-0.121	-0.005
2	Asc.	-7.58	-1.318	-0.025	0.165	-0.034
3	Asc.	-7.47	-1.235	0.084	0.114	-0.074
4	Asc.	-7.71	-0.823	0.369	-0.206	-0.204
1	Des.	-8.24	-0.696	0.589	-0.274	-0.233
2	Des.	-8.16	-1.433	0.211	0.185	-0.099
3	Des.	-7.84	-0.936	0.201	-0.040	-0.120
4	Des.	-8.22	-0.910	0.071	-0.042	-0.016

Table 6.1: σ° model polynomial parameters for a 15 day time period.

Cell #	1	2	3	4
Gain parm.	-0.066	0.055	-0.046	-0.057
Cell #	5	6	7	8
Gain parm.	-0.134	0.016	-0.004	0.049
Cell #	9	10	11	12
Gain parm.	0.074	-0.159	-0.104	-0.076

Table 6.2: σ° model cell gain parameters for a 15 day time period.

These parameters reveal the differences in the response of the individual antennas and cells. The standard method of correction is to first establish a reference. This reference is the model that we want the measurements to follow. The difference between the model and the reference is the amount to be used in correcting the measurements. This can be written as:

$$\begin{aligned} \mathcal{C}\left(\theta_{in}, cell_n, beam_n, Asc/Des_n\right) &= \mathcal{F}\left(\theta_{in}, cell_n, beam_n, Asc/Des_n\right) \\ &\quad -\mathcal{R}\left(\theta_{in}, cell_n, beam_n, Asc/Des_n\right) \end{aligned} \tag{6.4}$$

where $\mathcal{C}$ is the equation for the correction, $\mathcal{F}$ is the equation modeling the measurements [Eq. 4.3], and $\mathcal{R}$ is the chosen reference response to be used in the particular application. For a given measurement z_n, the corrected measurement $\hat{z}$ is found by:

$$\hat{z}_n = z_n + \mathcal{C}\left(\right) \tag{6.5}$$

This is the general method for correction to be used here. The differences in the methods discussed for the remainder of this chapter deal with reasons for choosing a particular $\mathcal{R}$ for a given application.

6.3 Reference Equation Selection

As mentioned earlier, the correction to be done on the measurements will depend on the application for the measurements. Three different correction methods were used. The basic types of corrections are: 1) polynomial response correction and 2) seasonal and time variation correction. These corrections may or may not be necessary for all given applications. This section will treat each correction separately although they may also be used together. Examples of these corrections will be given in section 6.4.

6.3.1 Polynomial Response

In general, it is desirable for all of the different antennas to produce the same measurement for the same type of terrain and incidence angle. By observing the calculated model parameters, it can be seen that this is not the case. All of the antennas should have the same model parameters, so that all antennas give

Asc./Des.	A'	B'	C'	D'	E'
Asc.	-7.66	-1.079	0.121	-0.012	-0.079
Des.	-8.12	-0.994	0.268	-0.043	-0.117

Table 6.3: Reference equation parameters for data in Table 6.1.

the same response under the same condition This can be done by choosing the reference equation as:

$$\mathcal{R} = A' + B'\vartheta + C'\vartheta^2 + D'\vartheta^3 + E'\vartheta^4 \tag{6.6}$$

where the A', B', etc. coefficients of the reference polynomial are chosen to represent the polynomial to which the measurements will be corrected. The values for the coefficients will again depend on the application for the correction. For general corrections, A', B', etc. are chosen to correspond to the mean response of all the antennas; for example, A' would be chosen as the mean of the model parameters for A for each antenna, and so on. A separate reference is used for the ascending and descending passes to prevent contamination from time-of-day:

$$A'_l = \frac{\sum_{j=1}^{4} A_{jl}}{4}, \tag{6.7}$$

where, as before, j and l are the antenna number and the ascending/descending number, respectively, with similar equations for the other coefficients of $\mathcal{R}$. Using this method for the parameters of Table 6.1, we get the coefficients for $\mathcal{R}$ shown in Table 6.3.

For applications such as high resolution land imaging however, it is necessary to have a linear response for σ° versus θ_i. In order to get this type of response the values of C', D' and E' should be chosen to be zero. By doing this, nonlinearities in the measurements will be eliminated. If This causes the calibrated data set to have a linear response.

6.3.2 Seasonal Correction

As discussed above, the time variations in the measurements are due to seasonal changes in the terrain and time-of-day variations. The time of day

variations have been handled by separating the antennas into ascending and descending passes. In order to remove any of the seasonal variations in the data, time windowing has been done.

In removing the variations in the data due to the time of day it is necessary to establish a constant reference equation common to both the ascending and descending passes. Using the mean response as above we have:

$$A' = \frac{\sum_{j=1}^{4}\sum_{l-1}^{2} A_{jl}}{8} \tag{6.8}$$

A similar method is used in the seasonal corrections. In this case, the values used for A', B', etc. will be found by calculating the reference parameters using all of the measurements. This will give a common reference equation for all of the time windows with different correction parameters for each time window. In this way an improved data set where the measurements are more consistent over time from antenna to antenna. The correction equation used here should come from the time window whose center is closest in time to the measurement being corrected.

6.4 Example Correction

One example of using these corrections is in high resolution land imaging. The SIRF algorithm assumes that the relationship of the measurements is linear with respect to θ_i. Therefore the reference equation for this case will be linear. The coefficients A' and B' are found from the polynomial fit from all of the measurements. The reference equation for this case is:

$$\mathcal{R}(\vartheta) = -7.579 - 1.010\vartheta \tag{6.9}$$

This same reference is used over the entire mission for both the ascending and descending passes. This removes all of the seasonal effects in the measurements, giving the correction equation:

$$\mathcal{C}(t,k,\vartheta) = A(t)+7.579+[B(t)+1.010]\vartheta+C(t)\vartheta^2+D(t)\vartheta^3+E(t)\vartheta^4+G_C(t,k) \tag{6.10}$$

where k is the cell number and t represents time. This is the equation to be used in correcting each of the measurements as in Eq. 6.5.

Another option is to do a correction over time while using the mean parameters for both the ascending and descending antennas as a reference. The correction parameters calculated in this way describe the deviations from the mean of the different parameters over time. The correction equation in this case is

$$\begin{aligned} \mathcal{C}(t,k,\vartheta) &= A(t) - A'(t) + [B(t) - B'(t)]\,\vartheta + [C(t) - C'(t)]\,\vartheta^2 \\ &\quad + [D(t) - D'(t)]\,\vartheta^3 + [E(t) - E'(t)]\,\vartheta^4 + G_C(t,k) \end{aligned} \quad (6.11)$$

This may be rewritten by defining A_c as $A - A'$ (and similarly for B_c through E_c) as:

$$\mathcal{C}(t,k,\vartheta) = A_c(t) + B_c(t)\,\vartheta + C_c(t)\,\vartheta^2 + D_c(t)\,\vartheta^3 + E_c(t)\,\vartheta^4 + G_{Ck}(t) \quad (6.12)$$

Figures 6.1 through 6.4 show this correction as a function of incidence angle and time. This gives the correction necessary for each of the antennas so that all patterns will match the mean response, giving an indication of the bias of the measurements from different antennas and cells, while excluding the seasonal information. These figures also show errors around day number 210, due to the small number of measurements.

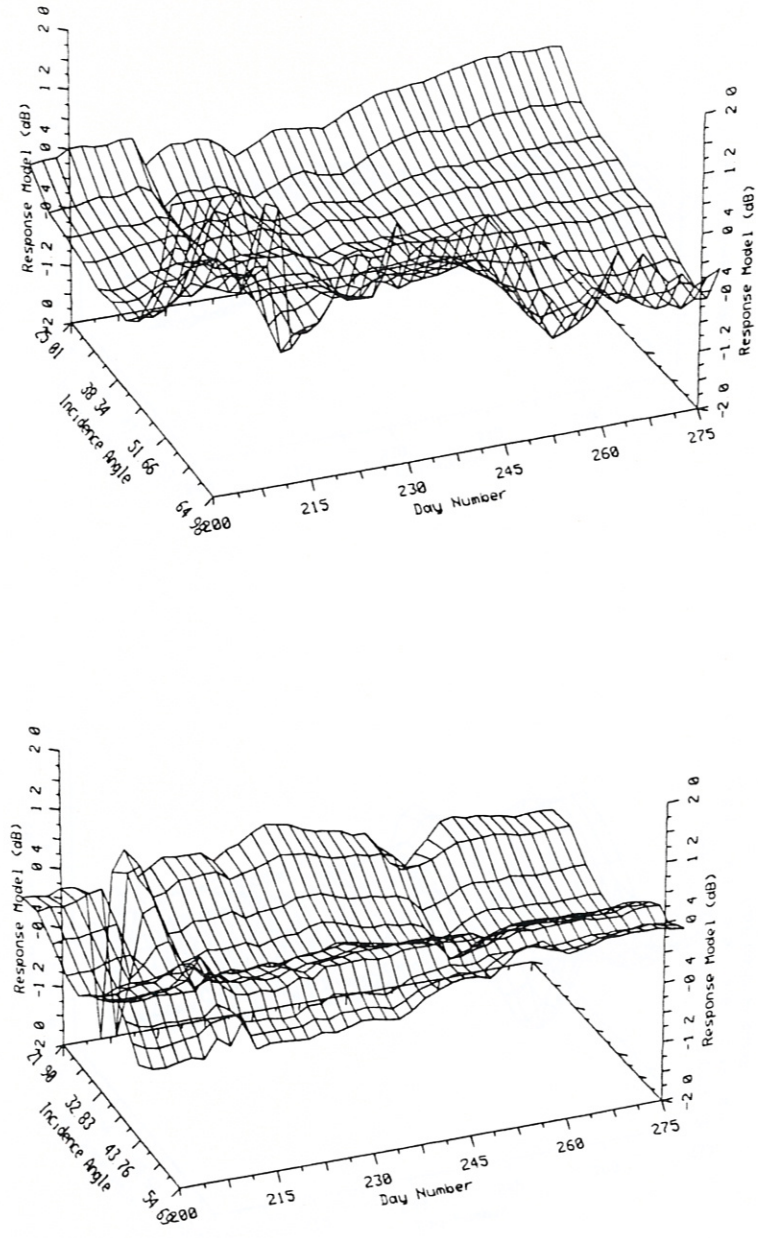

Figure 6.1: Correction to be made for antenna 1 Ascending (top) and descending (bottom).

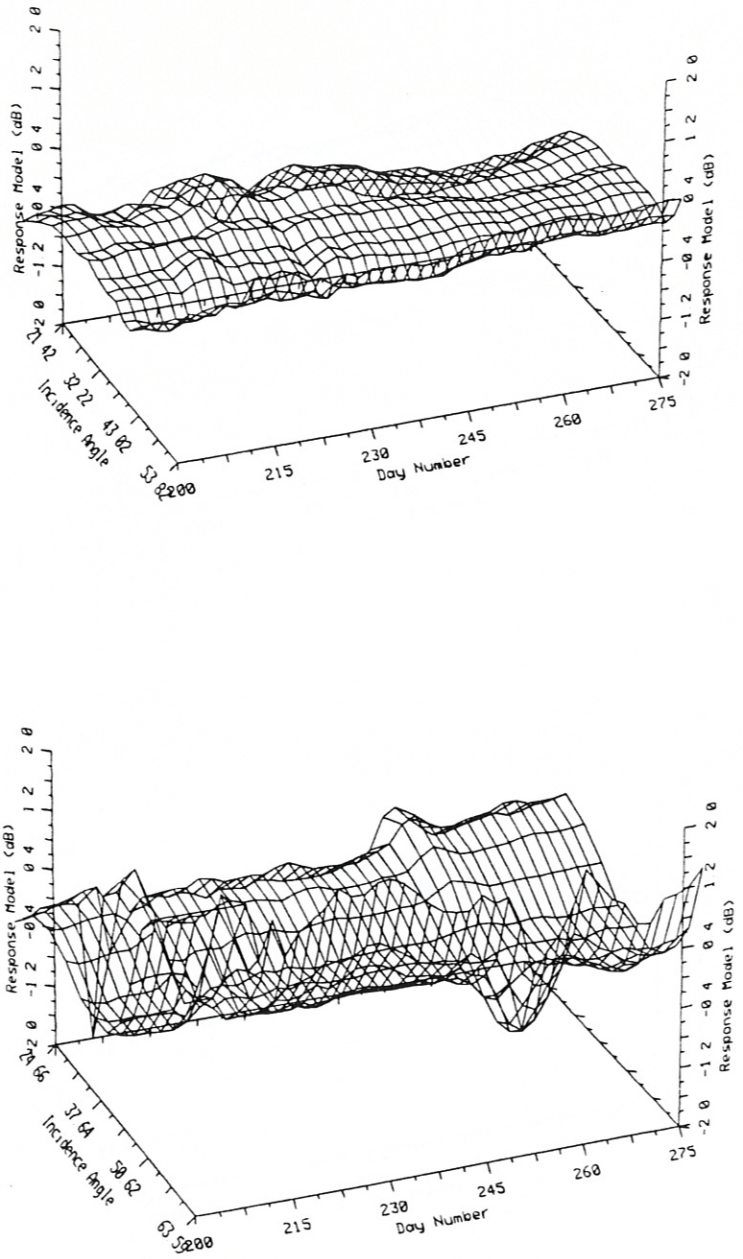

Figure 6.2: Correction to be made for antenna 2 Ascending (top) and descending (bottom).

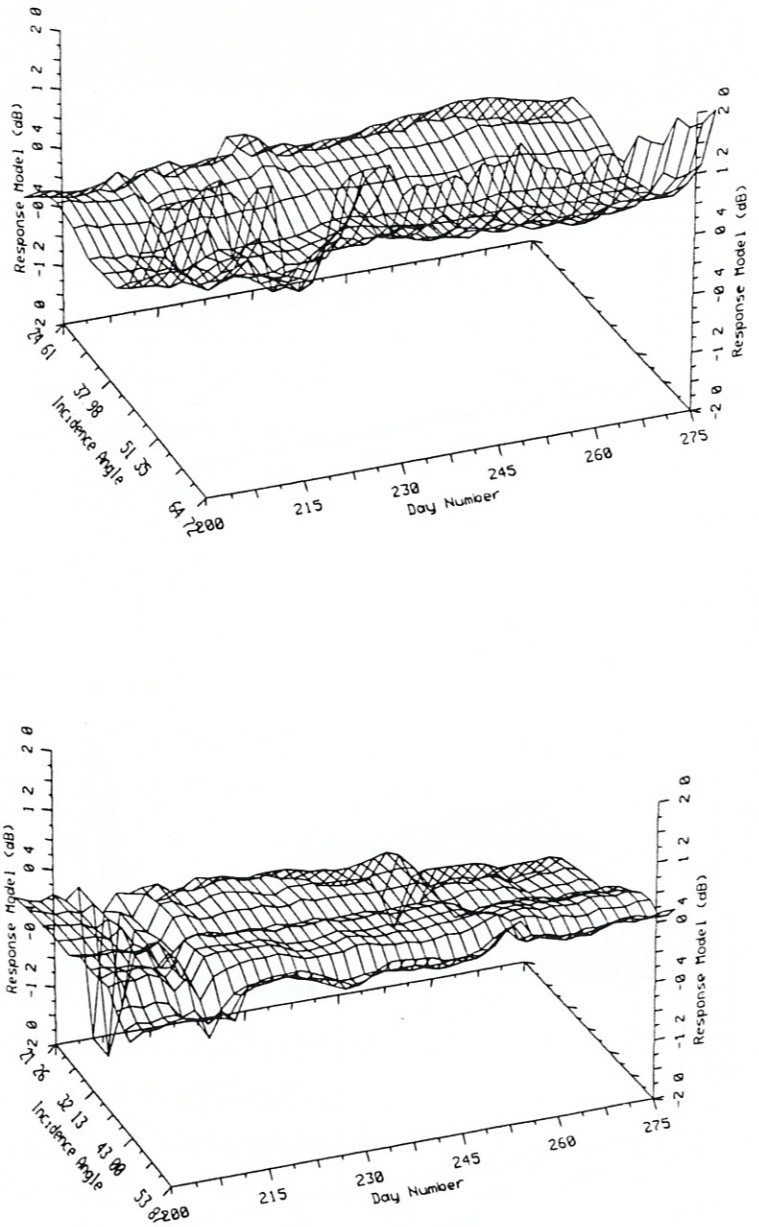

Figure 6.3: Correction to be made for antenna 3 Ascending (top) and descending (bottom).

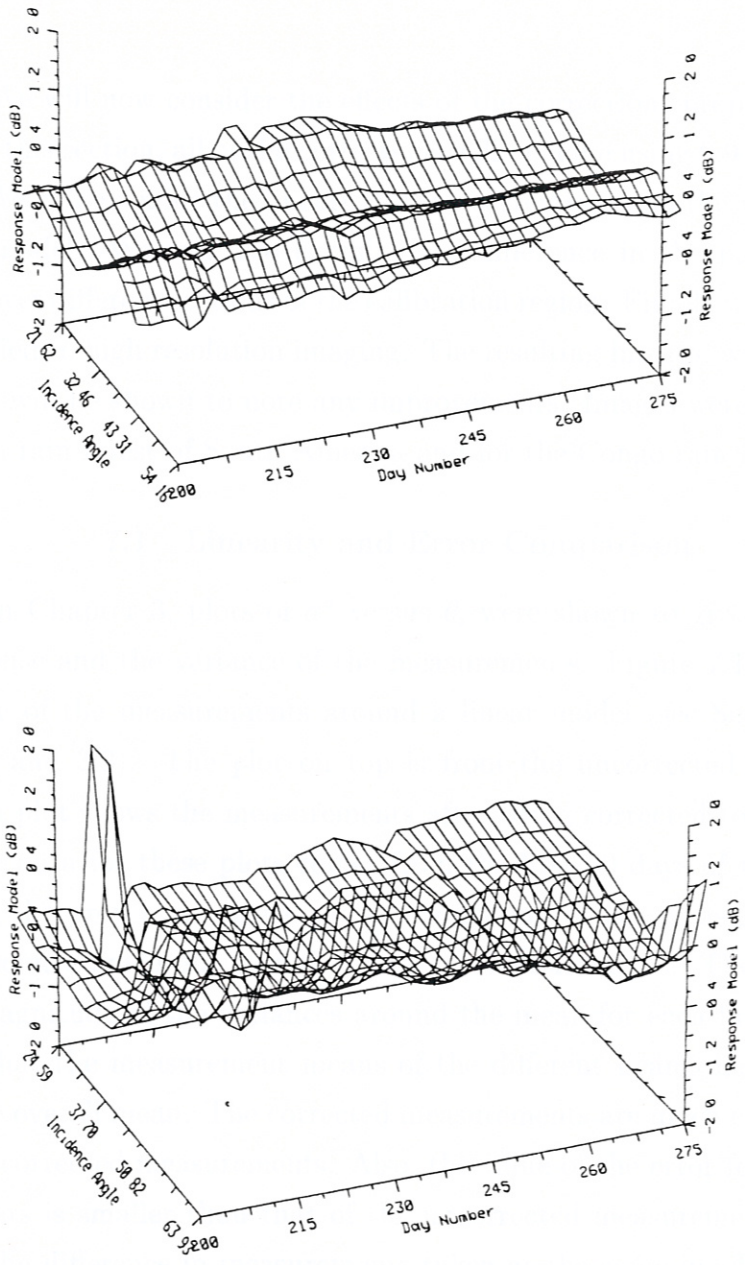

Figure 6.4: Correction to be made for antenna 4 Ascending (top) and descending (bottom).

CHAPTER 7

RECALIBRATION ASSESSMENT

We will now consider the effects of the corrections proposed in the last chapter. In this section, all of the corrections will be done using 6.9 as the reference equation. We will examine the linearity of the corrections and the variance around the linear model. We will also examine the difference in the parameters when calculated over different sections of the calibration region. Finally, the recalibration will be applied to high resolution imaging. The resulting images, with and without corrections, will be shown to note any improvements. Images were made for both the Amazon rain forest of South America and for the Congo rain forest of Africa.

7.1 Linearity and Error Comparison

In Chapter 3, plots of σ° versus θ_i were shown to give an idea of the linear response and the variance of the measurements. Figure 7.1 shows plots of the variance of the measurements around a linear model (see Section 3.2.1 and Figures 3.8 and 3.9). The plot on top is from the uncorrected measurements. The bottom plot shows the measurements after being corrected to follow a linear model. The data for these plots comes from the first 30 days of the mission. In these plots, the grey scale shows the concentration of the measurements within each 2° incidence angle bin over the range of measurements. The line markings show the magnitude of the variances around the mean for each bin. From this it is evident that the measurement means of the different beams have been moved closer to the overall mean. The corrected measurements are much closer to the line than the uncorrected measurements. Also, the value of the error for the corrected measurements is smaller than that of the uncorrected measurements. This error represents the difference in measurements taken at the same incidence angle. It is also evident that the corrected measurements are also closer to linear than the uncorrected measurements.

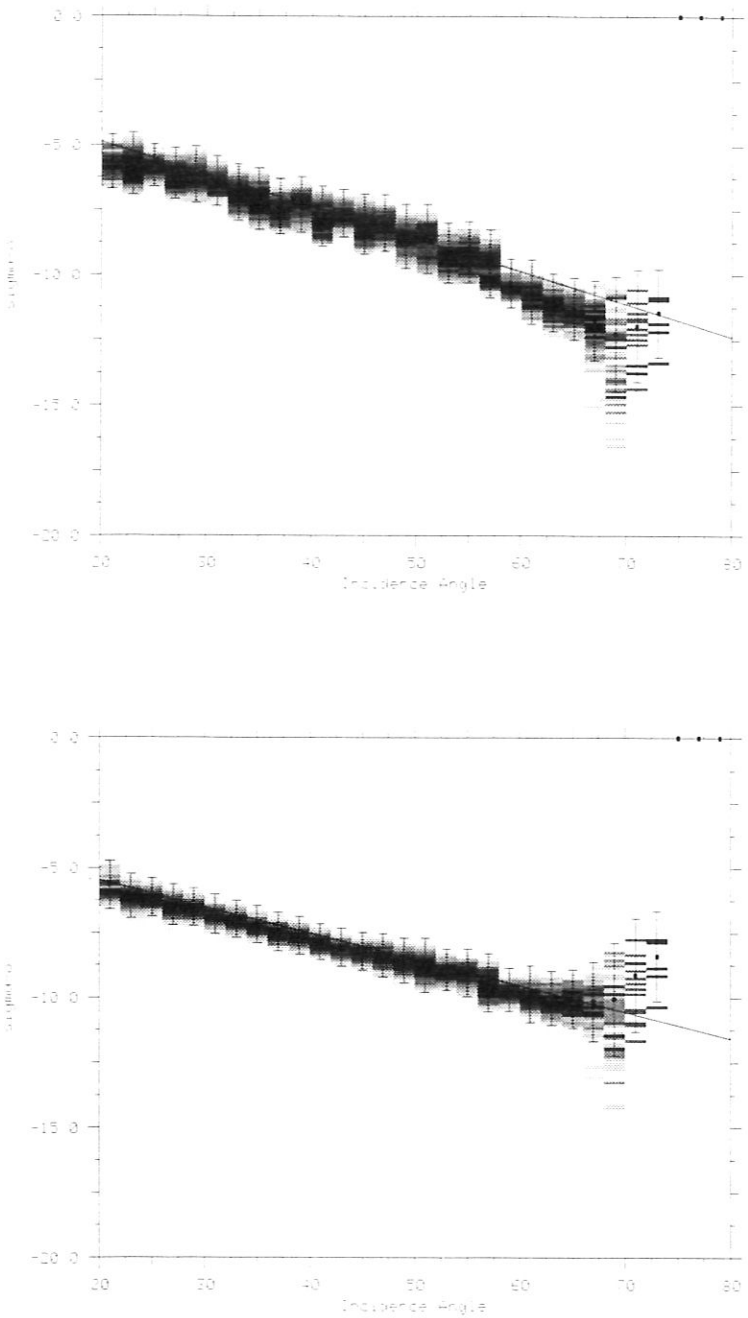

Figure 7.1: Plot of the mean and variance for uncorrected (top) and corrected (bottom) measurements

7.2 Parameter Location Dependance

As discussed before, the calibration data set was split into four different areas and the model parameters were calculated for each of them. Figures 7.2 and 7.3 show the A parameters for the ascending pass in each of the four sections. Because of the difficulty in obtaining a good parameter estimate with small amounts of data, the parameters in these plots were estimated using a ten-day time window. Although the parameters from the separate sections have more variation than the parameters estimated using the entire data set, the differences in the plots are small. This suggests that the parameters are not very sensitive to location. Figure 7.4 shows the A parameters over the Congo rain forest. Because of the smaller data set used over the Congo, the time window for this region was set at sixteen days rather than eight. These parameters also suggest a low sensitivity to location. Because of the slight variations in the parameters it should be possible to use the parameters calculated over the Amazon to do a recalibration of the Congo measurements.

7.3 Image Improvement

The original image of the Amazon area is given in Figure 3.1. Using the same method, the corrected measurements were used to produce the image of Figure 7.5. The corrected image shows the same resolution as the uncorrected image, with the improvement of having some of the graininess of the uncorrected image removed. In order to make the differences in the two images more apparent, two sections of the image over the Amazon have been expanded in Figures 7.6 and 7.7. This shows a good improvement in the corrected image.

A similar comparison between images made before and after the corrections, the Congo rain forest has been used. Figures 7.8 and 7.9 show the uncorrected and corrected images respectively for the Congo rain forest. The corrected image was made using the model parameters found over the Amazon rain forest. Further study of the parameters over the Congo area can be found in the appendix.

In order to see if further improvements are possible, the image from the calibrated data set was used to make a land mask similar to the one used in the data selection. This new land mask, shown in Figure 7.10 can be compared with

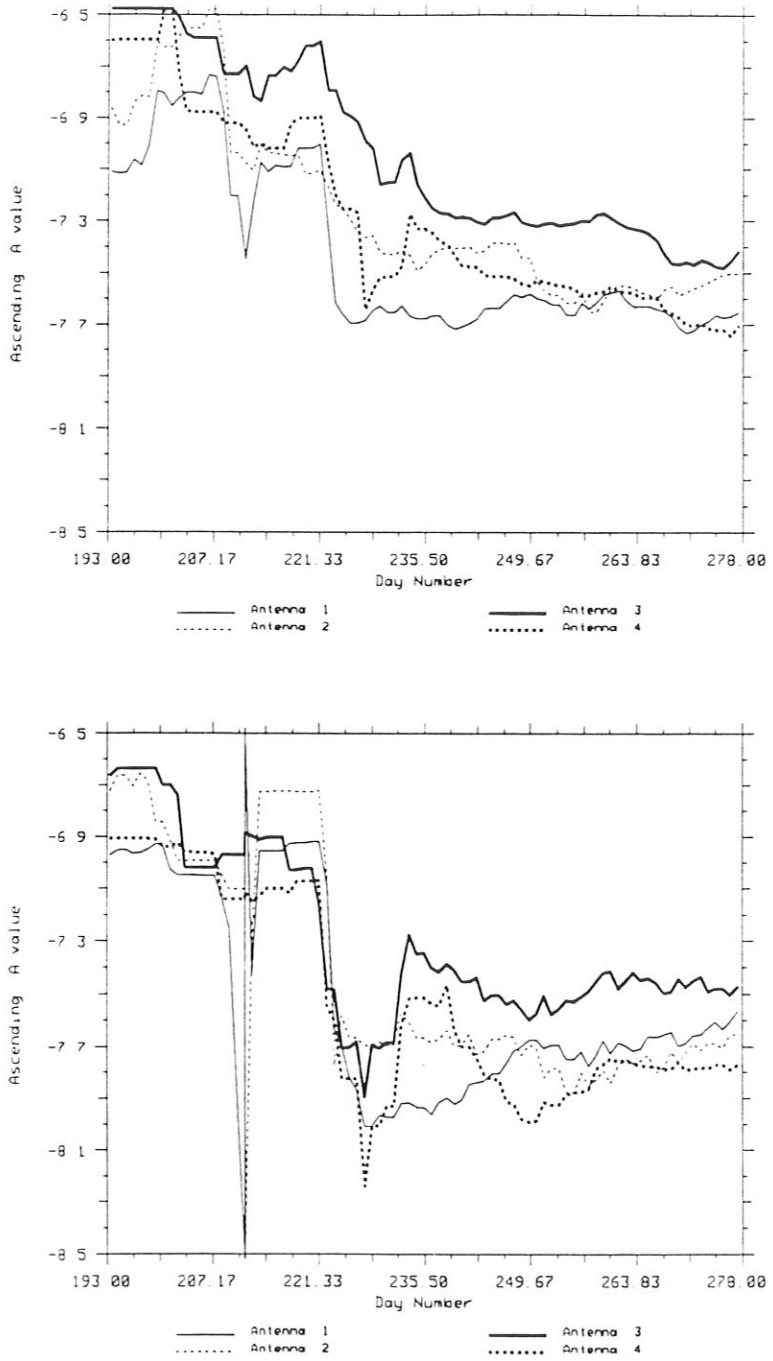

Figure 7.2: A parameters for sections NW (top) and SW (bottom) of the calibration data set

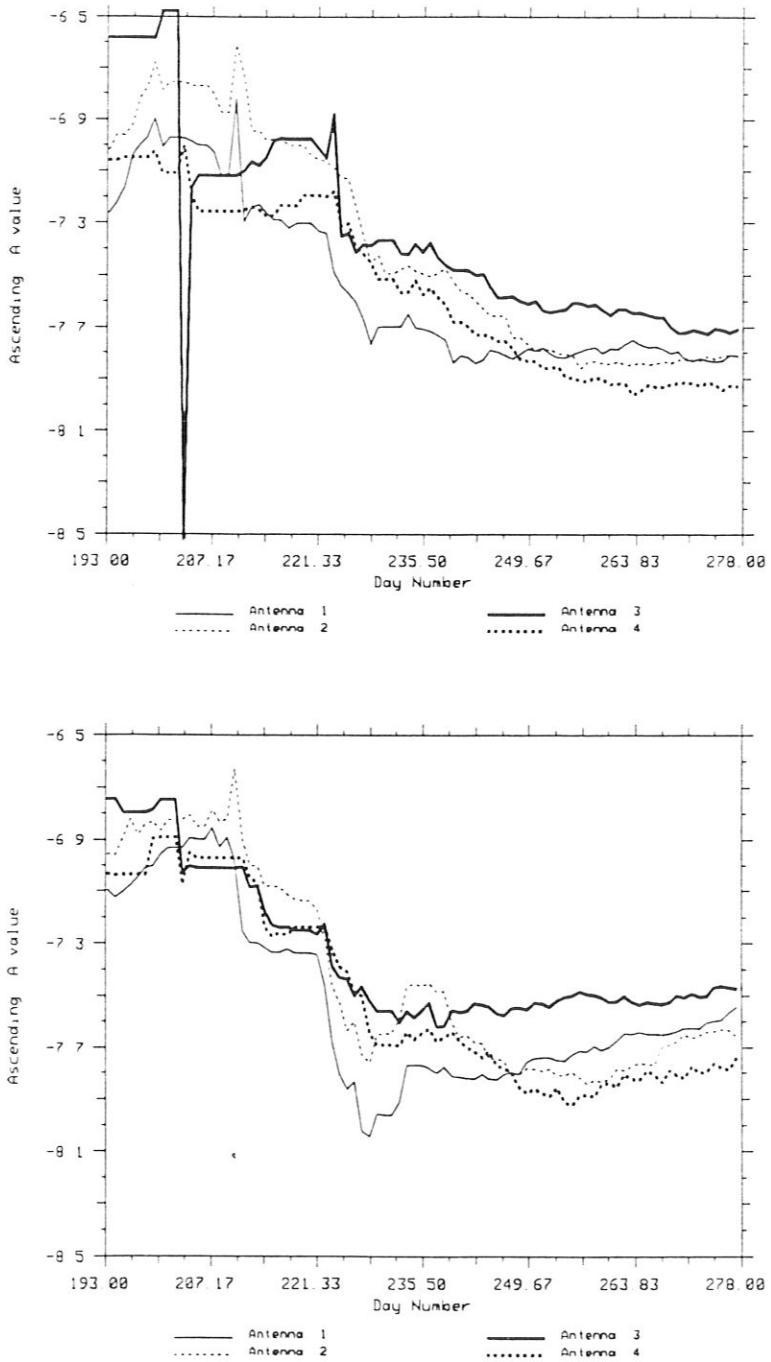

Figure 7.3: A parameters for sections NE (top) and SE (bottom) of the calibration data set

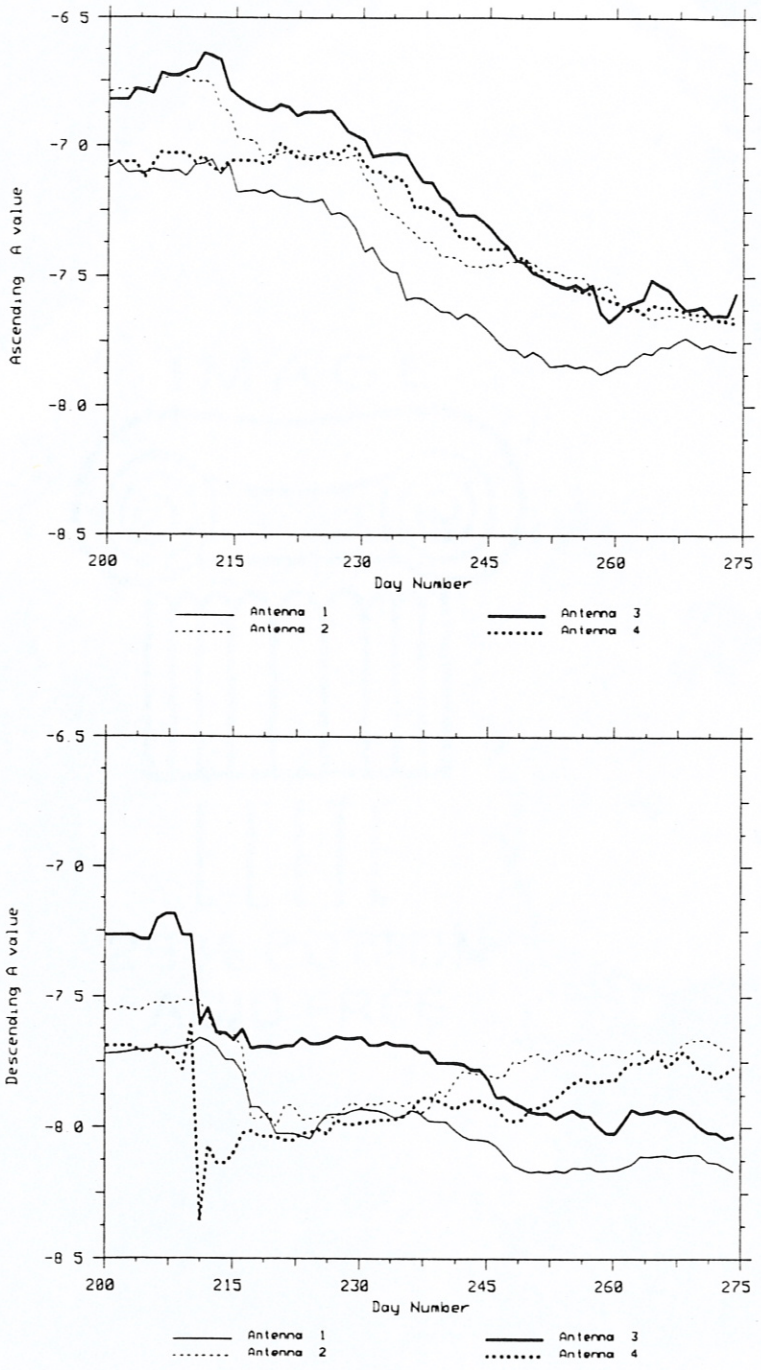

Figure 7.4: Estimated A parameters over the Congo rain forest. Ascending (top) and Descending (bottom)

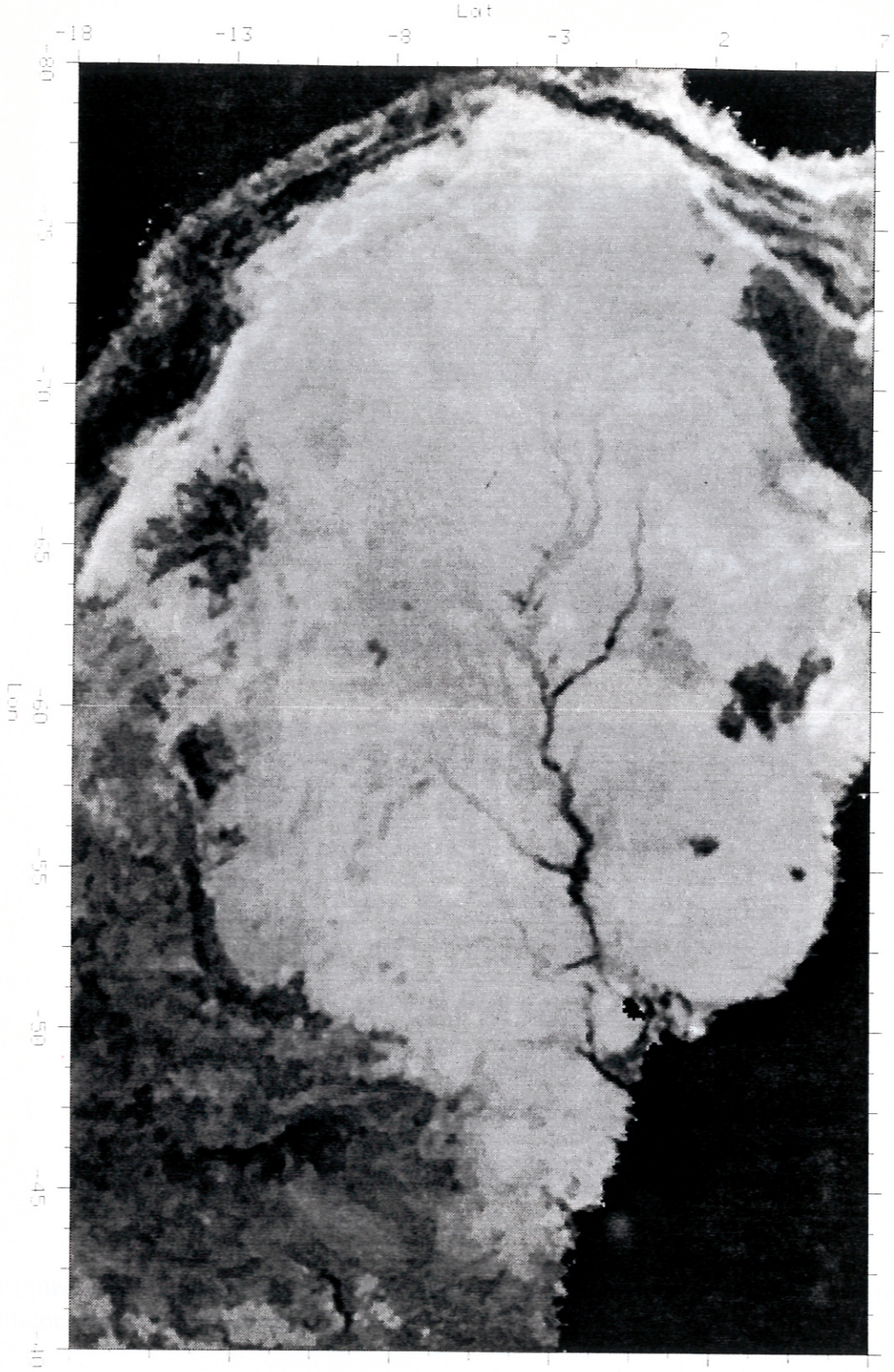

Figure 7.5: The SIRF image made using corrected measurements.

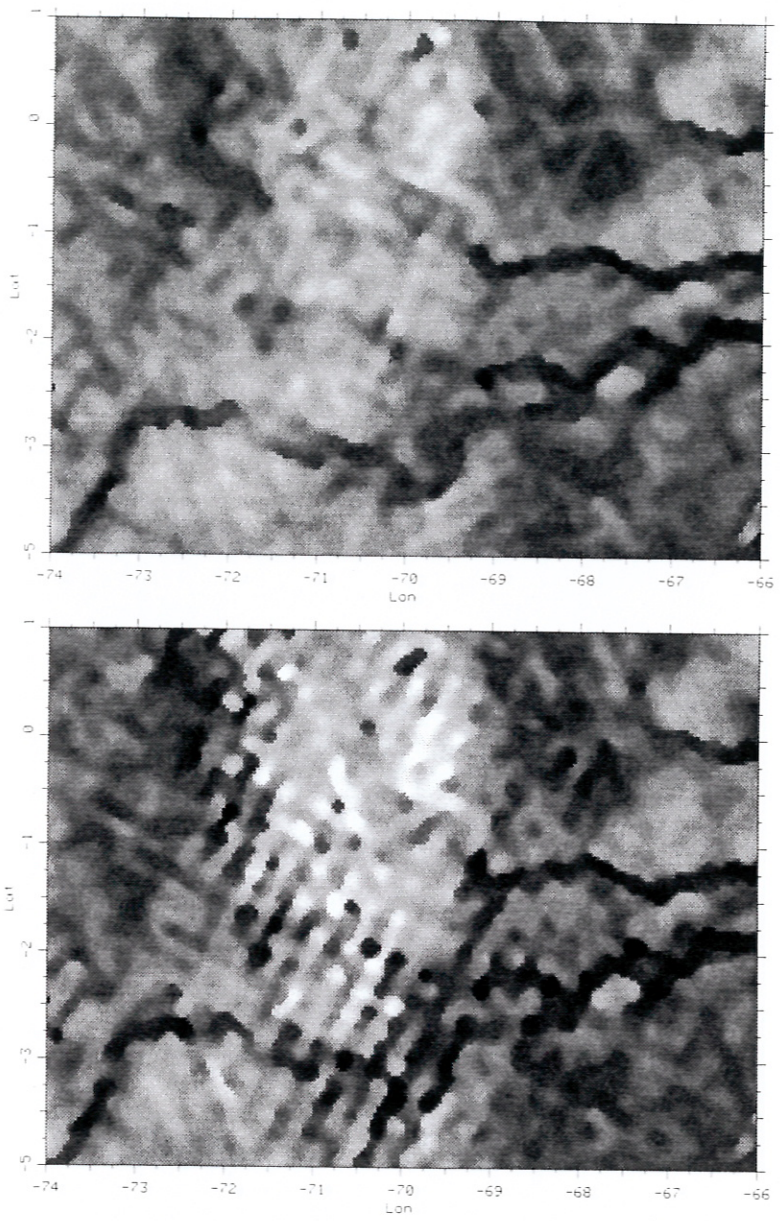

Figure 7.6: This shows the improvement in the corrected image (top) over the uncorrected image (bottom)

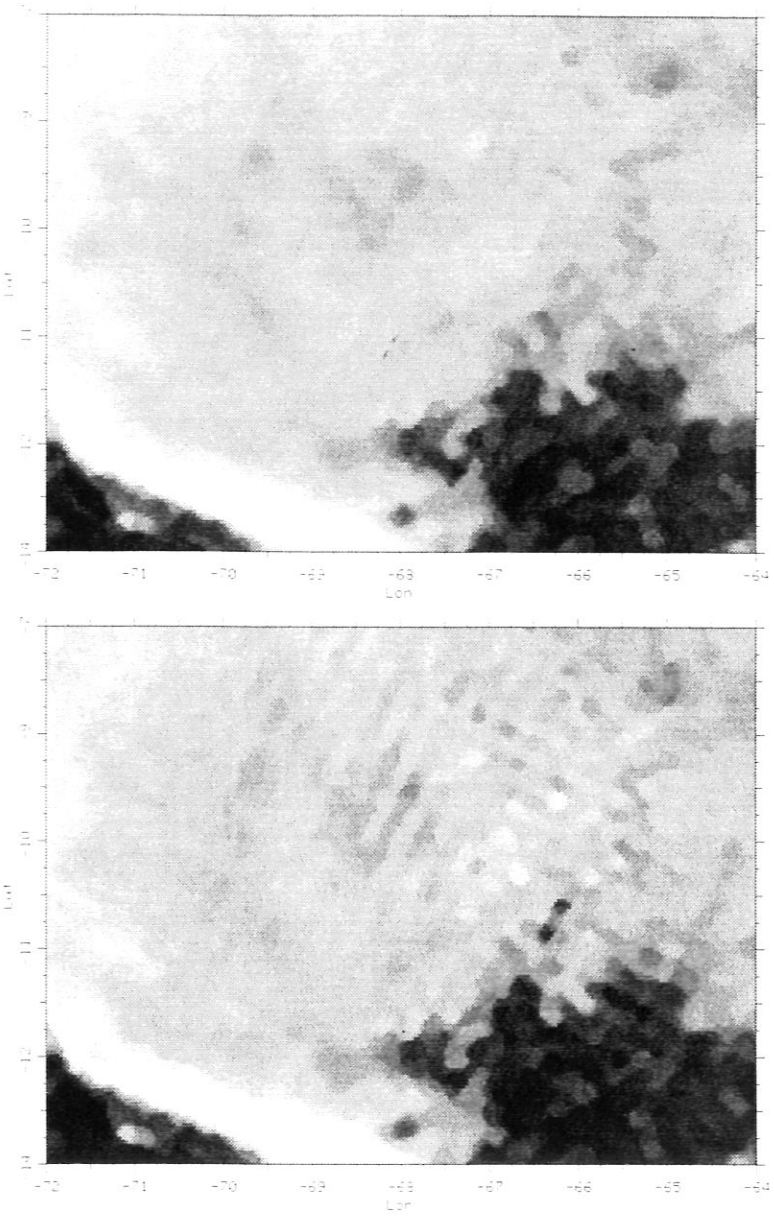

Figure 7.7: This shows the improvement in the corrected image (top) over the uncorrected image (bottom)

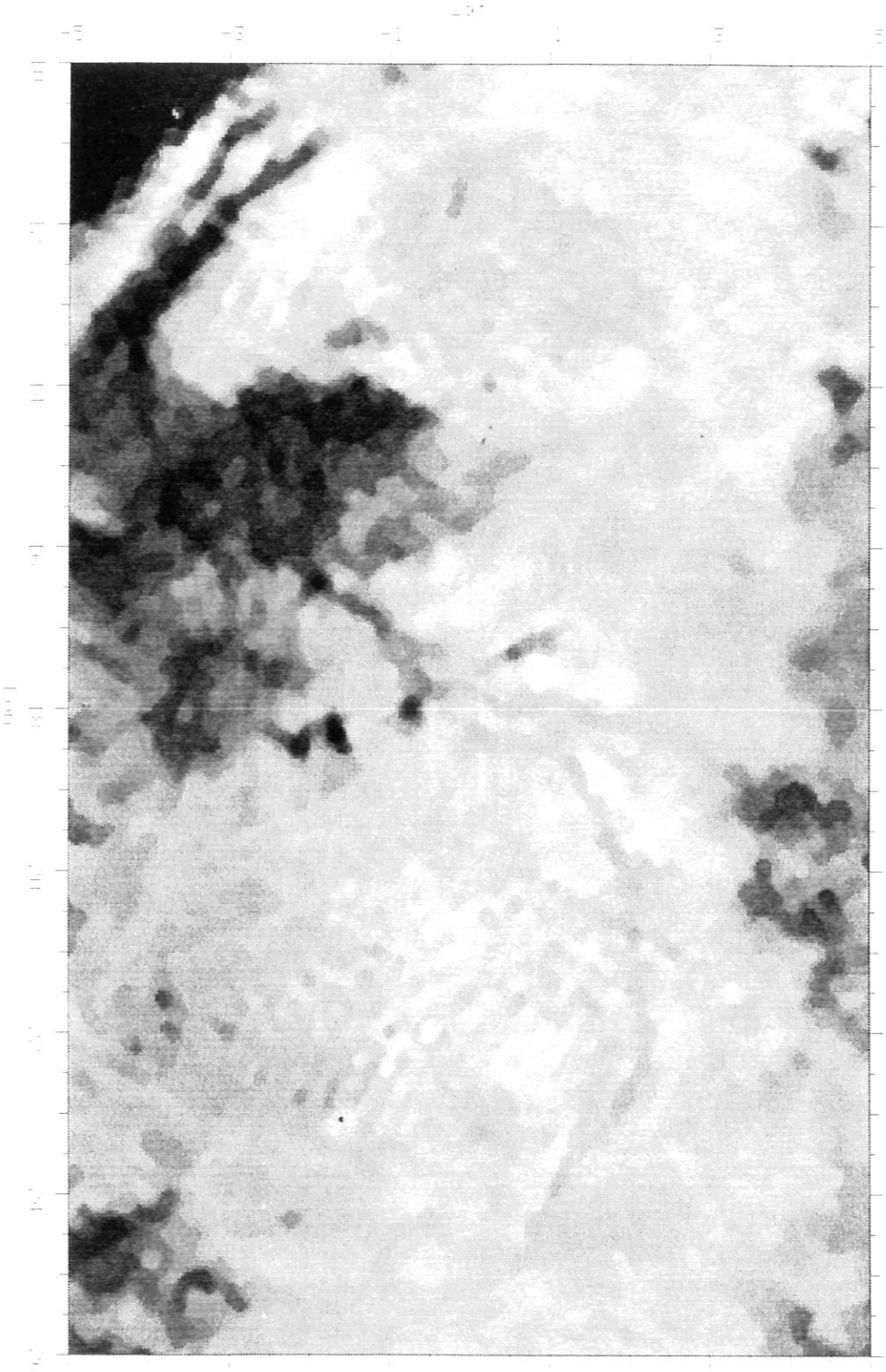

Figure 7.8: The Congo SIRF image made using uncorrected measurements.

Figure 7.9: The Congo SIRF image made using corrected measurements.

the one of figure 3.2. The differences in these masks are small, suggesting that no further iterations are necessary. The actual parameters calculated from the new land mask are given in the appendix.

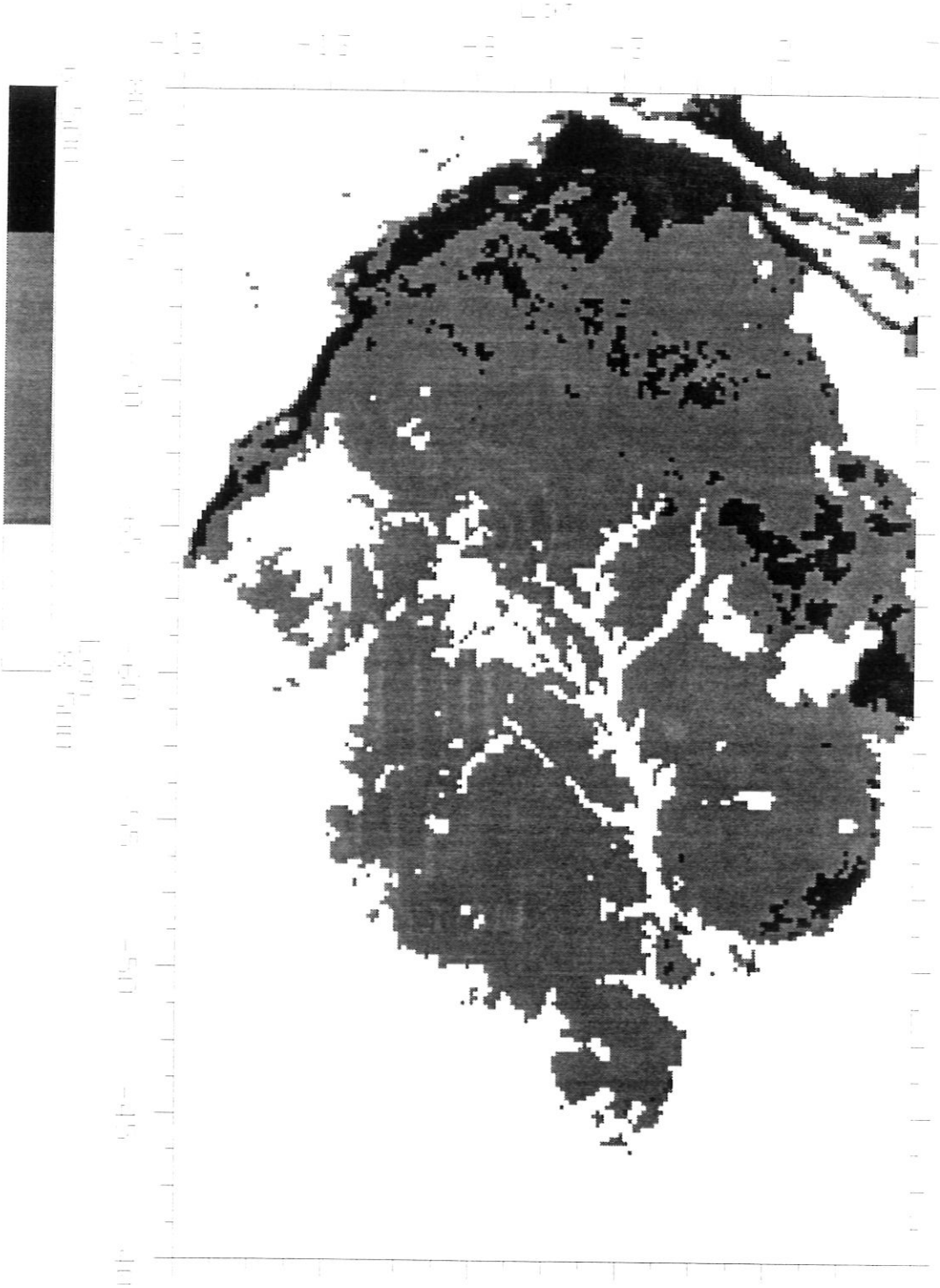

Figure 7.10: Land mask made using the corrected SIRF image

CHAPTER 8

CONCLUSIONS

8.1 Discussion

In the discussion of modeling and correcting the SASS measurements, the goal has been to improve the usefulness of the data, by developing a correction technique to improve the consistency of the measurements from different antennas and cells. This eliminates cell-dependent or antenna dependent bias in the data, making it possible to use any of the measurements from any of the cells or antennas without regard to instrument errors. This correction is important for most applications of SASS data. Corrections for time variability of the data and linearity were also considered. These two corrections are important in high resolution land imaging. By reducing the variability of the measurements in the data set, the imaging algorithm is able to produce images with less noise. This will improve the discrimination accuracy of the images.

8.2 Findings

In doing the preliminary analysis of the data, it was noted that the SASS data was remarkably good over most of the mission. The new findings that come from this work include:

1. The measurement data has been analyzed in detail and inconsistencies in the measurements over the same area were noted. These include antenna and time response differences, thus suggesting the need for recalibration.

    - Gain differences between the antennas were of the order of a few tenths of a dB were noted.
    - Slowly-varying time-dependent variations of up to 1 dB exist in the measurements of the Amazon and Congo rain forests.

2. A time-dependent model for the measurements from each antenna was developed. The model used was a fourth order polynomial in θ_i, and a sliding eight-day window.

3. In order to remove inconsistencies, the model of the measurements has been used to determine a recalibration to be applied to each measurement.

4. Several correction methods were considered.

   - Correction to the mean response of the antennas (several tenths of a dB).
   - Correction to a specified polynomial for all antennas (up to several tenths of a dB depending on the polynomial used).
   - Time-dependent corrections (over one half dB in cases needing a linear response over the entire mission).

5. The model parameters determined over the large Amazon area are similar to those parameters determined over only parts of the Amazon or over the Congo area. This indicates a small location dependence of the calibration correction.

6. Although the seasonal responses of the Amazon and Congo are broadly similar, the seasonal information in the model parameters from one area may not be useful for all areas. The estimated time dependent model for the Amazon and Congo differed by as much as one dB over a short interval of time.

7. Using the correction method developed here, images made of the rain forests can be improved by removing inconsistencies in the data.

8.3 Further Work

Although the work done here offers significant improvement in the measurement consistency between the different antennas, there are several ways in which this research may be improved. Some of the possible things to work on include developing better models for the measurements, using different areas other than rain forest, and using data from other scatterometers.

The model used in this research is quite simple and may be improved upon. The model used here is not able to distinguish between the seasonal effects of the land and long-term calibration changes in the instrument. Further work in modeling could include methods for distinguishing between the time varying changes of the land and the instrument. This would include developing time varying models for different types of land cover as well as for the instrument.

In the study done here, it was noted that there were large effects (as much as one dB) from the seasonal changes over the rain forest. It may be possible to reduce the large seasonal effects by choosing another area for the data selection. One possibility for this selection is the Antarctic. Because of the constant snow cover during the winter, it may be possible to obtain a data set with a much lower time variability, thus improving the accuracy of the correction.

Using data from other scatterometers may also be helpful in studying the seasonal changes in the rain forest. Because of the limited time of the Seasat mission, it is not possible to really study seasonal changes in the data over several years. As longer data sets become available, it may be possible to obtain better models for the seasonal changes of the land cover.

BIBLIOGRAPHY

[1] E. Bracalente and J. Sweet, "Analysis of normalized radar cross section (σ°) signature of amazon rain forest using seasat scatterometer data," NASA Technical Memorandum 85779, NASA, 1984.

[2] F. T. Ulaby, R. K. Moore, and A. K. Fung, *Microwave Remote Sensing, Active and Passive*, vol. 3. Dedham, MA: Artech House Inc., 1986.

[3] E. Bracalente, D. Boggs, W. Grantham, and J. Sweet, "The SASS scattering coeficient σ° algorithm," *IEEE Journal of Oceanic Engineering*, vol. OE-5, pp. 145–154, April 1980.

[4] J. Johnson, L. Williams, E. Bracalente, F. Black, and W. Grantham, "Seasat-A satellite scatterometer instrument evaluation," *IEEE Journal of Oceanic Engineering*, vol. OE-5, pp. 138–144, April 1980.

[5] D. G. Long, P. T. Whiting, and P. J. Hardin, "High-resolution imaging of land/ice using seasat scatterometer measurements," in *1992 International Geoscience and Remote Sensing Symposium*, 1992.

[6] D. G. Long and P. J. Hardin, "Land imaging with reconstructed high-resolution seasat-a scatterometer data: An amazon experiment," in *1992 International Geoscience and Remote Sensing Symposium*, 1992.

[7] R. G. Kennett and F. K. Li, "Seasat over-land scatterometer data, part I: Global overview of the ku-band backscatter coefficients," *IEEE Transactions on Geoscience and Remote Sensing*, vol. 27, September 1989.

APPENDIX A

AMAZON DATA

Because of the similarity in the land mask used from the original SIRF image and the mask made from the corrected image, parameters estimated from this new data set should be very close to those estimated previously. Figures A.1 through A.6 show the ascending model parameters estimated using the data set corresponding to the new calibrated image. These figures may be compared with 5.2 through 5.7. This is remarkably similar to the values found from the original land mask. Because of the similarities in the shapes and offset of the parameters from the two data sets, it is not likely that the parameters would improve with further iterations. It is also evident that the second estimation of the parameters is not significantly different than the first estimation

Another method for determining the amount of change in the estimated parameters due to the change in the mask is to look at the estimated parameters for the entire data set. This was done for both the original data set and for the recalibrated data set. The calculated parameters are shown in table A.1. Here it can be seen that the values of these parameters are close enough so that further iterations are not necessary.

Figures A.7 through A.10 show the differences between the models estimated from the original land mask and the new land mask. These show the differences to be quite small.

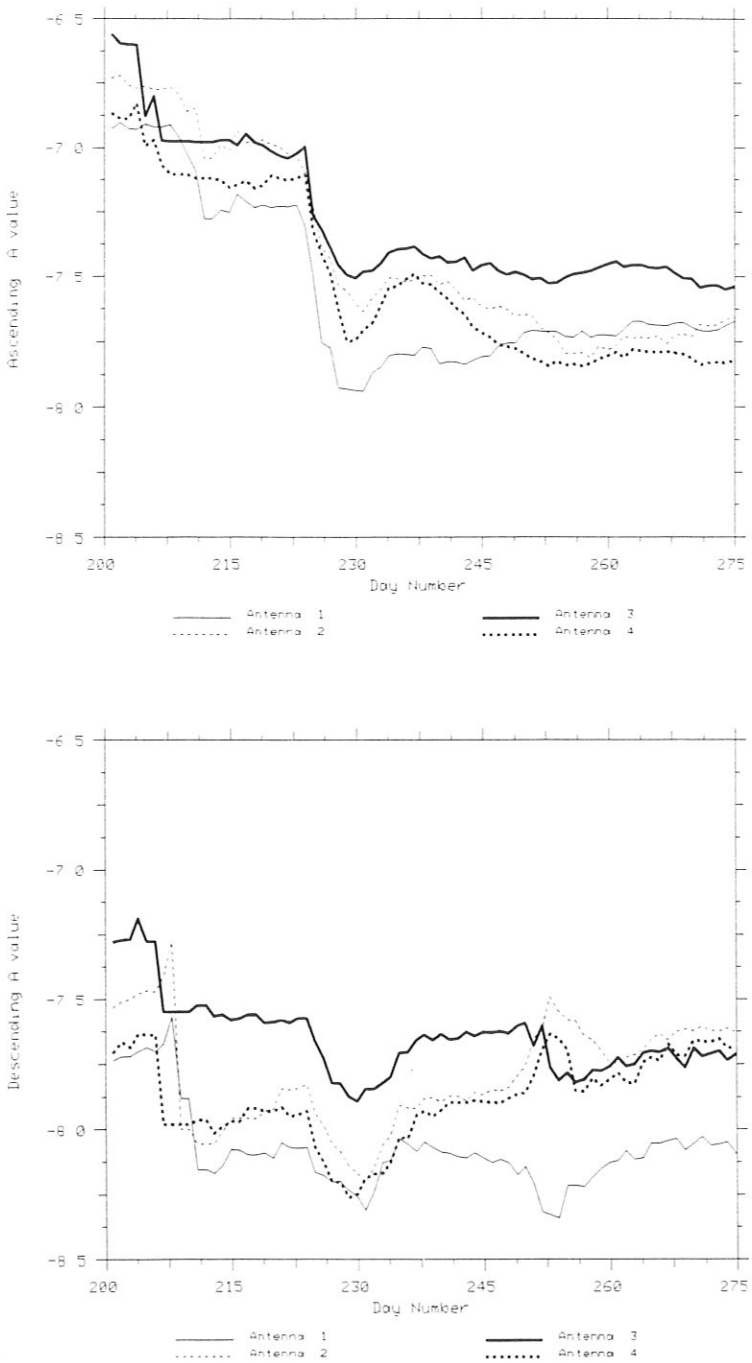

Figure A.1: Model A parameters estimated from the corrected mask. Ascending (top), descending (bottom).

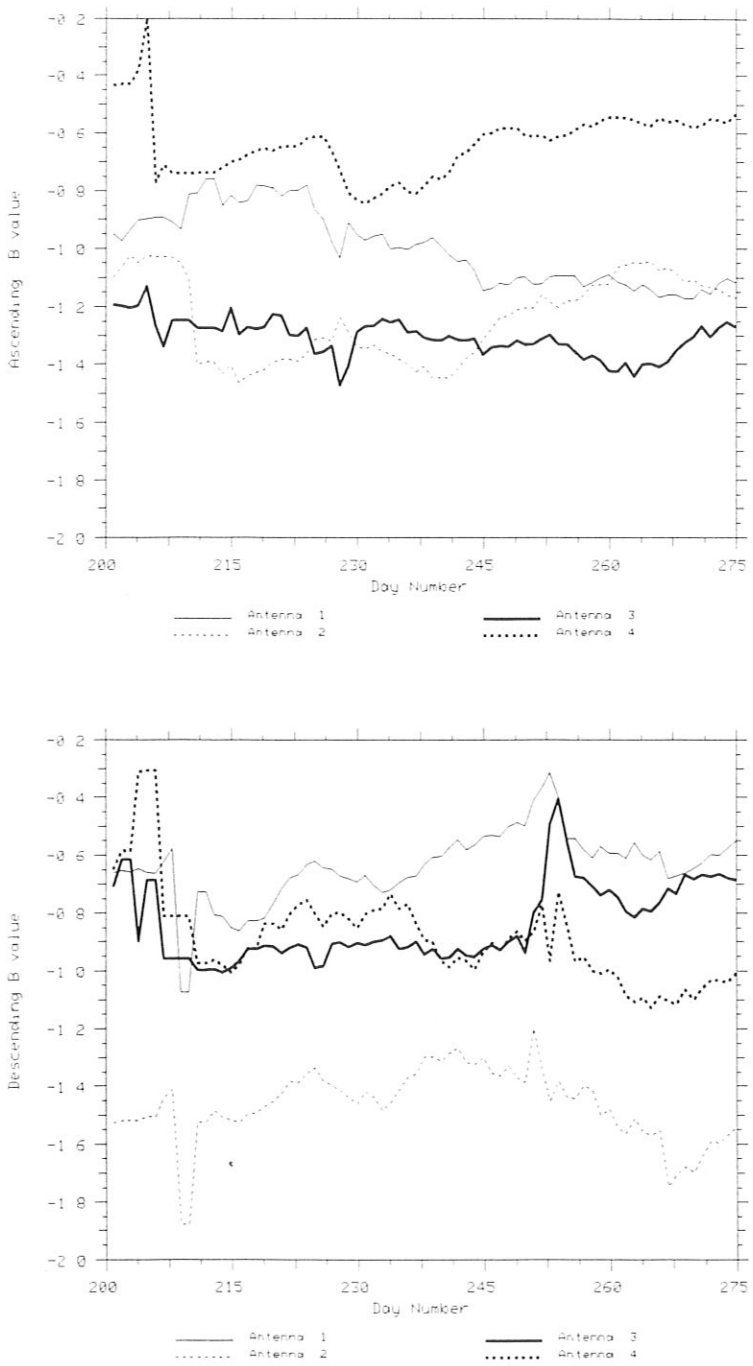

Figure A.2: Model B parameters estimated from the corrected mask. Ascending (top), descending (bottom).

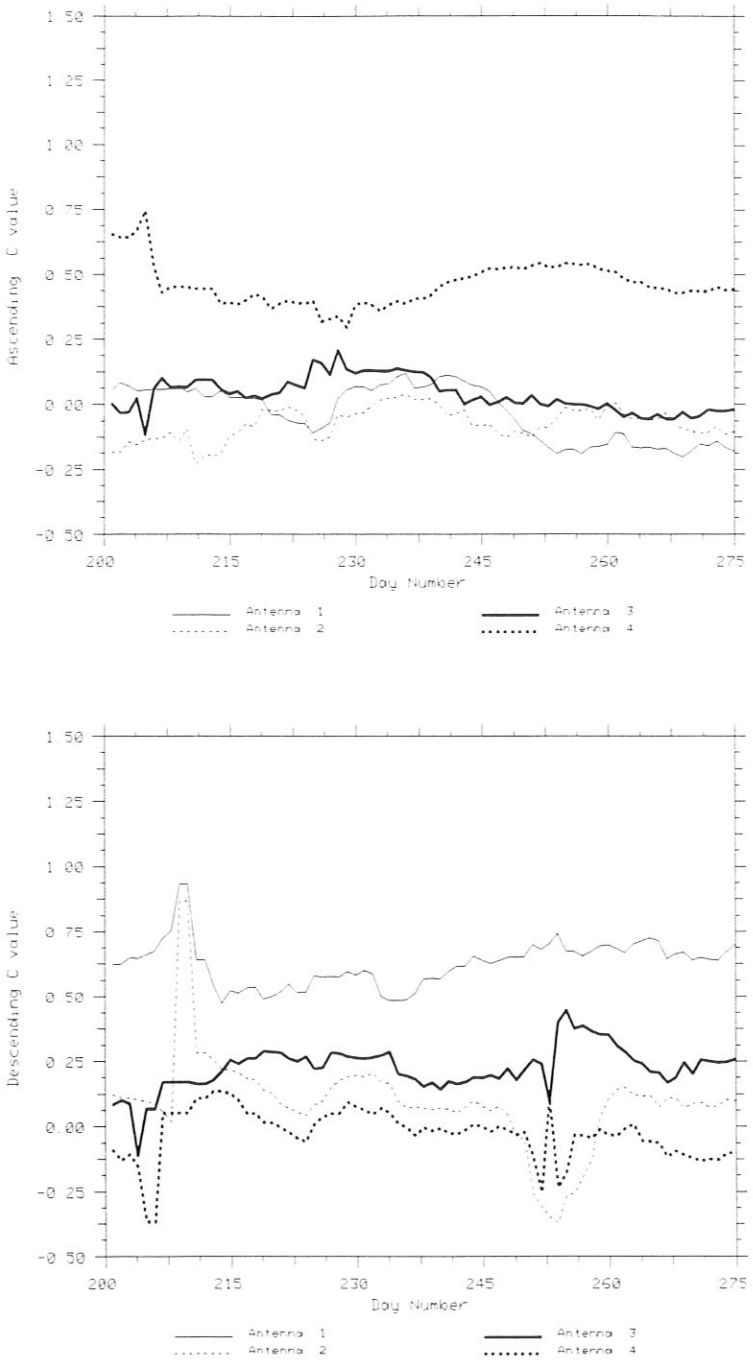

Figure A.3: Model C parameters estimated from the corrected mask. Ascending (top), descending (bottom).

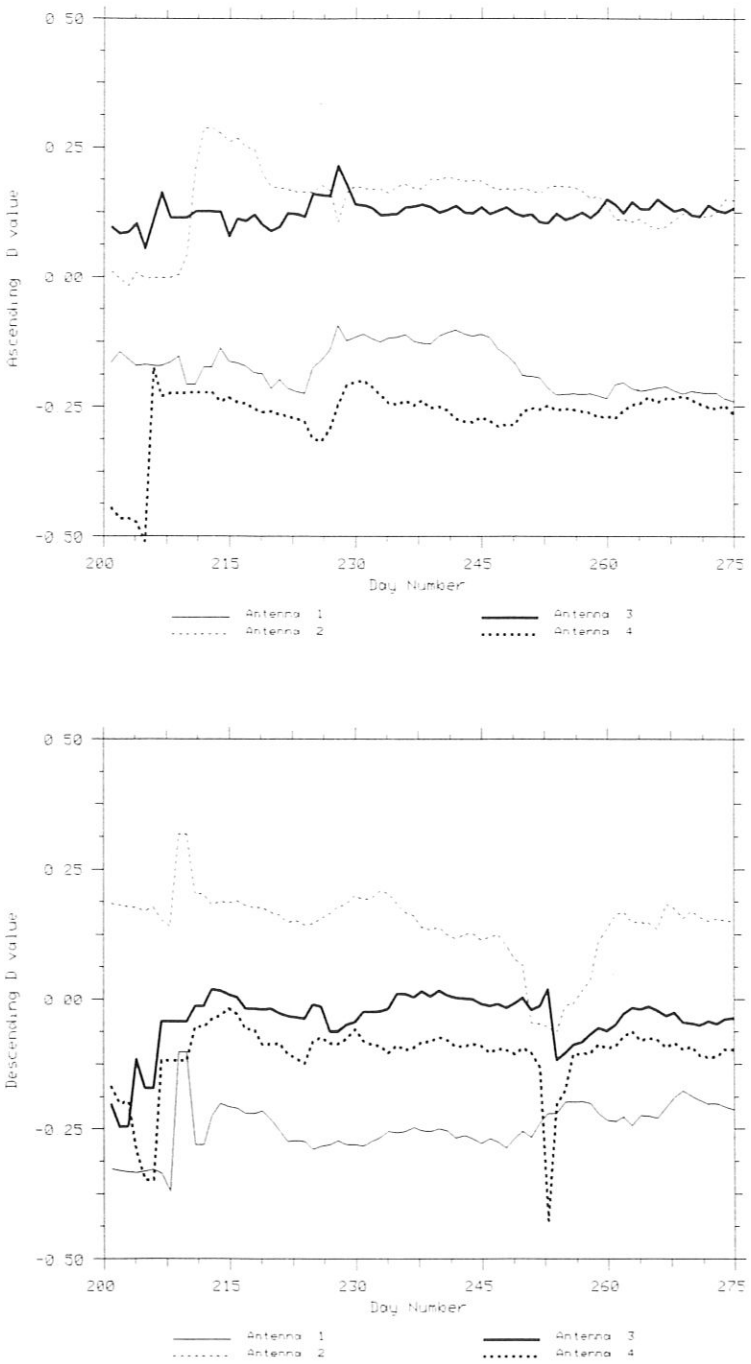

Figure A.4: Model D parameters estimated from the corrected mask. Ascending (top), descending (bottom).

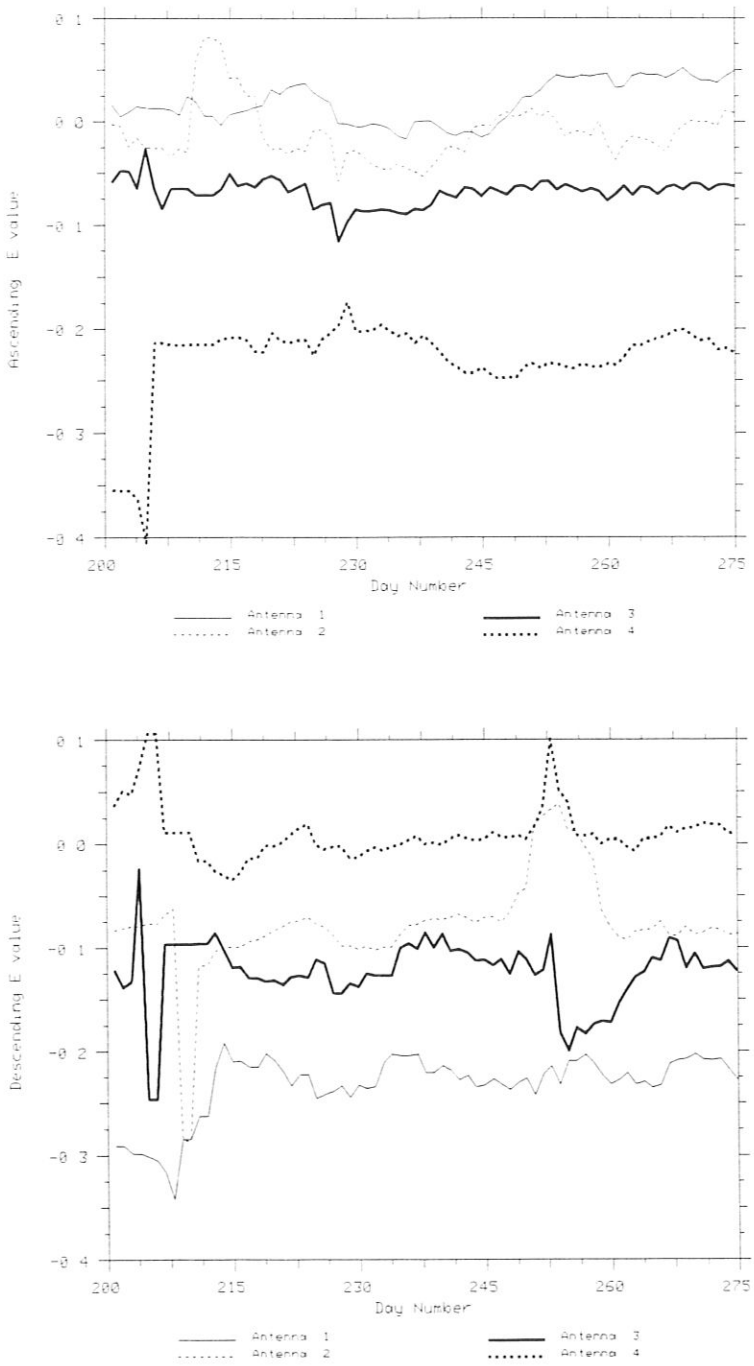

Figure A.5: Model E parameters estimated from the corrected mask. Ascending (top), descending (bottom).

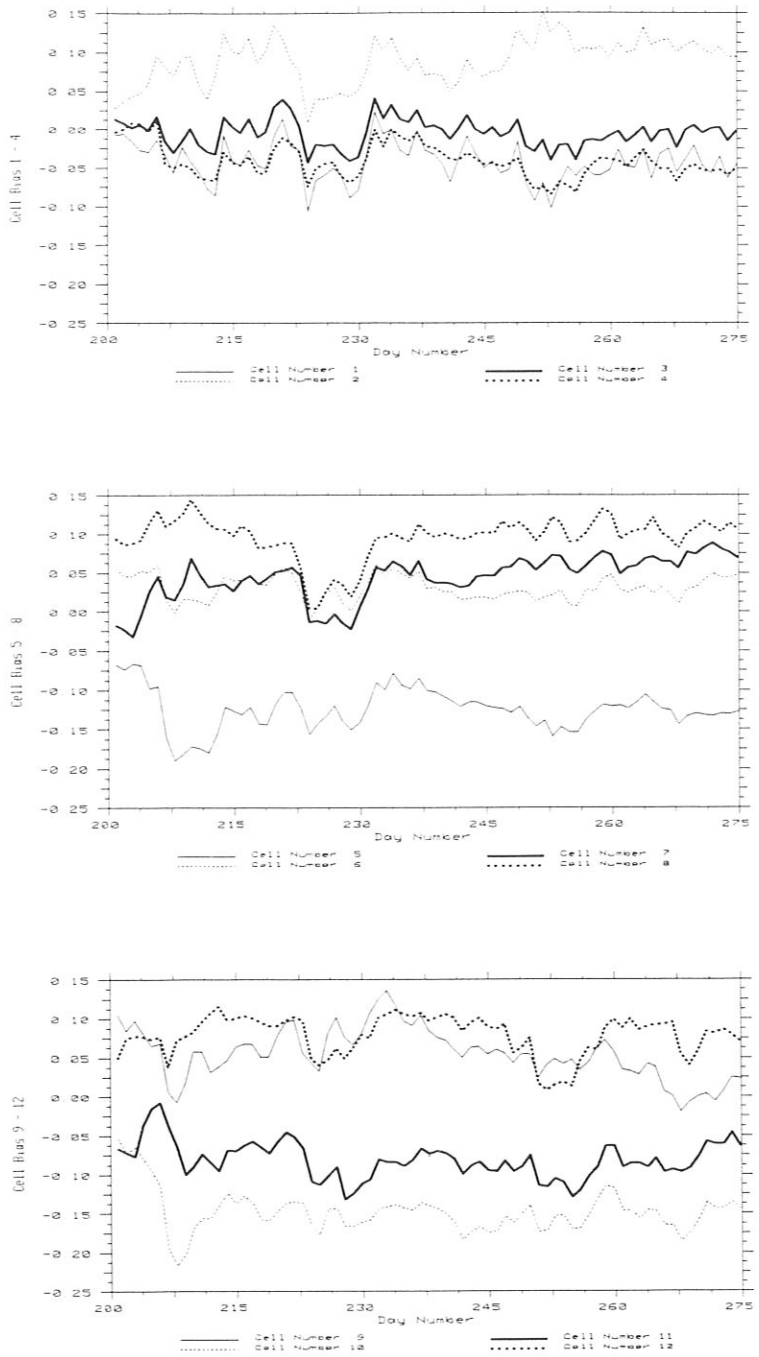

Figure A.6: Model Cell gain biases estimated from the corrected mask. Cells 1 - 4 (top), 5 - 8 (middle) and 9 - 12 (bottom).

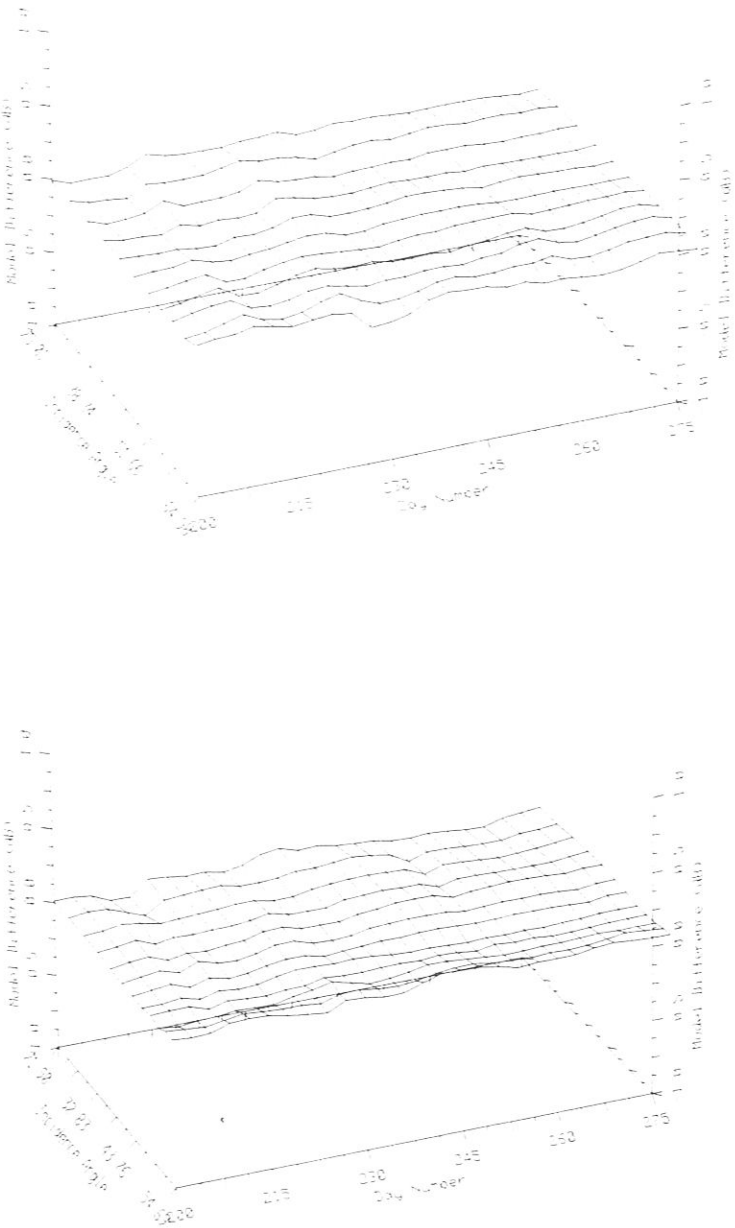

Figure A.7: Difference between the Amazon model using the original and corrected land masks for antenna 1. Ascending (top), descending (bottom).

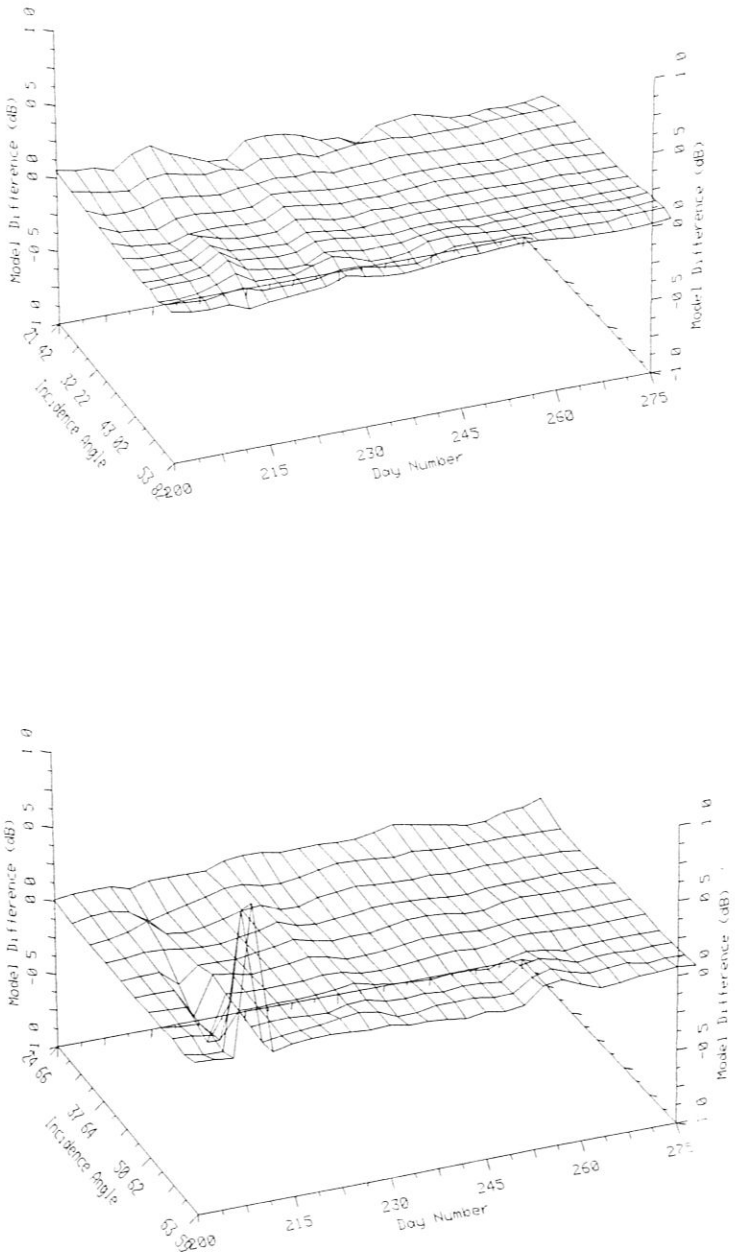

Figure A.8: Difference between the Amazon model using the original and corrected land masks for antenna 2. Ascending (top), descending (bottom).

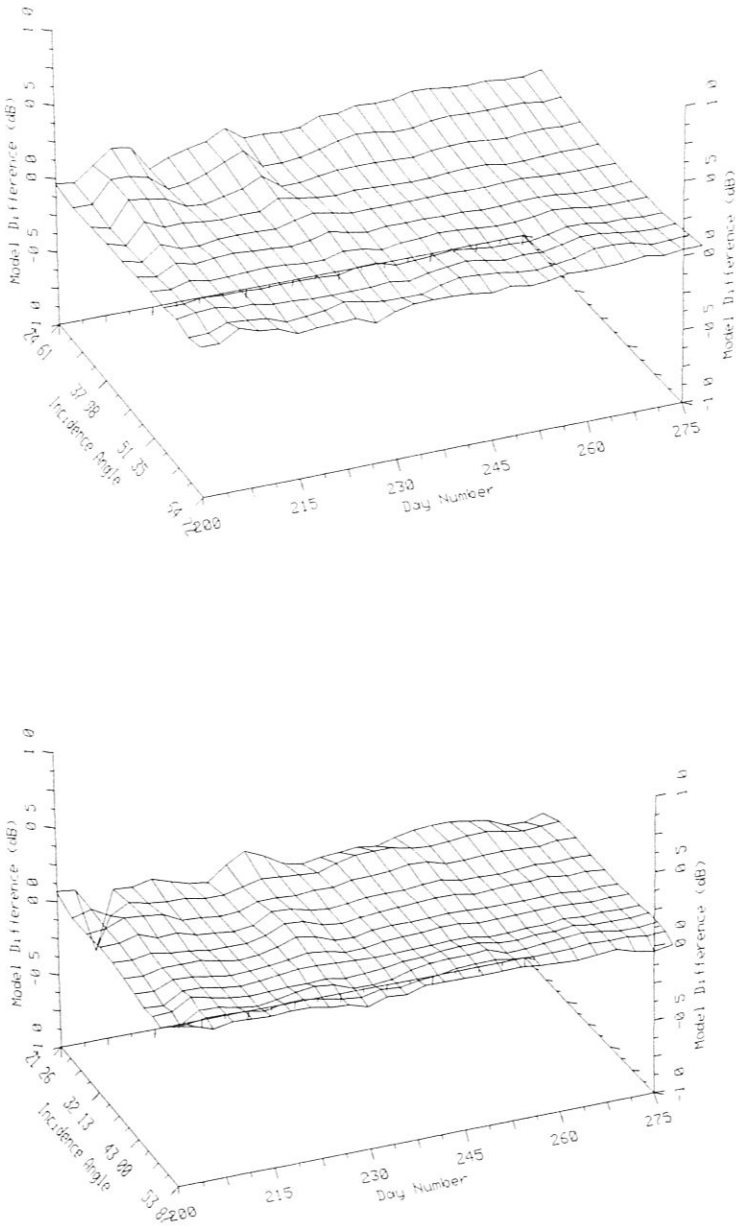

Figure A.9: Difference between the Amazon model using the original and corrected land masks for antenna 3. Ascending (top), descending (bottom).

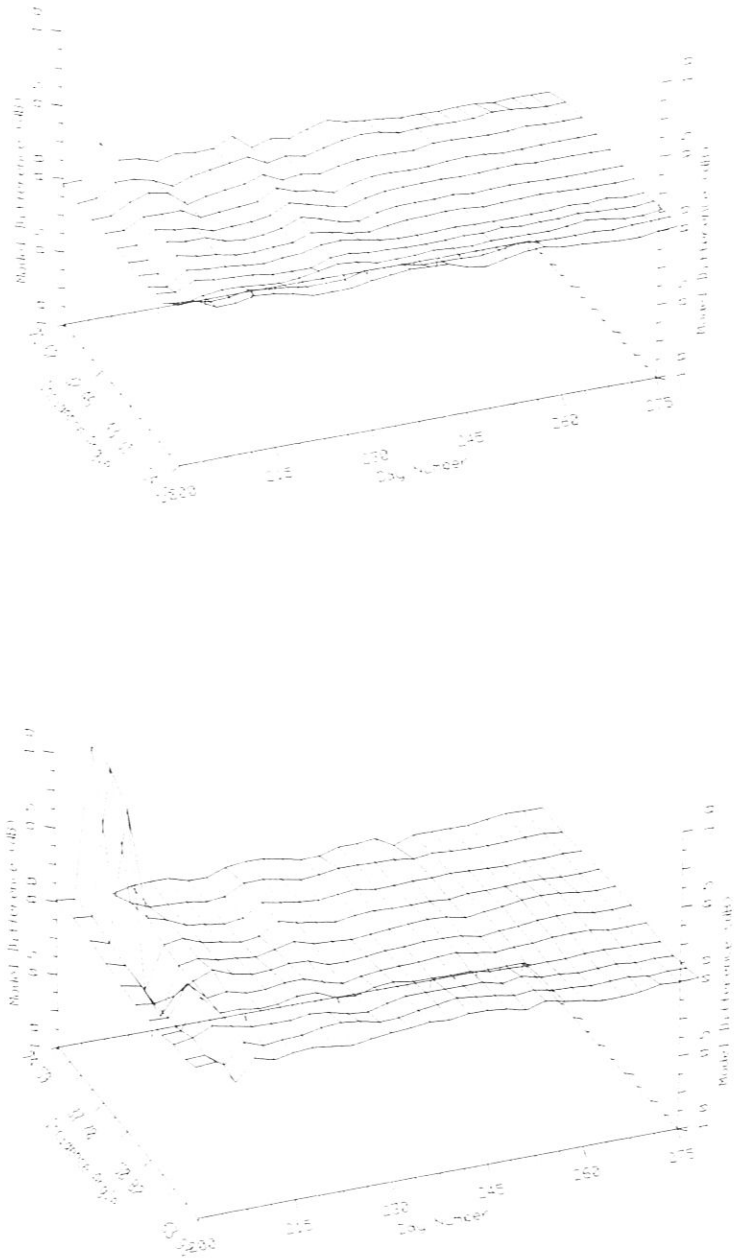

Figure A.10: Difference between the Amazon model using the original and corrected land masks for antenna 4. Ascending (top), descending (bottom).

	Original mask	Corrected mask
A	-7.579	-7.593
B	-1.010	-1.010
C	0.069	0.066
D	-0.022	-0.020
E	-0.040	-0.043

Table A.1: Regression parameters from the data using the uncorrected data mask and the corrected data mask.

APPENDIX B

CONGO DATA

While the Congo rain forest differs in vegetation from the Amazon rain forest, they are both equatorial rain forests. Because of this we expect the climate and seasonal response to be similar. This should allow the correction factors from the Amazon to be used with the measurements of the Congo. Figure B.1 shows the variance around a line for the uncorrected Congo data again for the measurements after correction with the Amazon correction factors.

The actual parameters over the Congo rain forest are shown in Figures B.2 through B.7. While these parameters differ from the parameters over the Amazon, these differences are small. These plots confirm the assumption that the seasonal effects over the Amazon and Congo should be similar. One problem with using the Congo forest measurements is that the data set is smaller than over the Amazon. This will cause the parameter estimates to be more dependent on noisy measurements. Because of the difficulty of obtaining a good parameter estimation with a small data set, the parameters have been estimated using a sixteen day window for the Congo data.

Figures B.8 through B.11 show the difference in the antenna response between the parameters calculated using the Amazon data and the parameters from the Congo data (compare with difference plots between the two land masks from the Amazon in Figures A.7 through A.10). These plots show the difference in the model from the two areas to be less than one dB for most places. The locations of large difference seem to be mostly from the seasonal differences in the two regions. There doesn't seem to be a constant offset between the two areas.

While the parameters calculated from the Amazon measurements and the Congo measurements are quite similar, there is a slightly different seasonal response. This means that it may not be possible to use parameters calculated over the Amazon in making corrections over the whole earth.

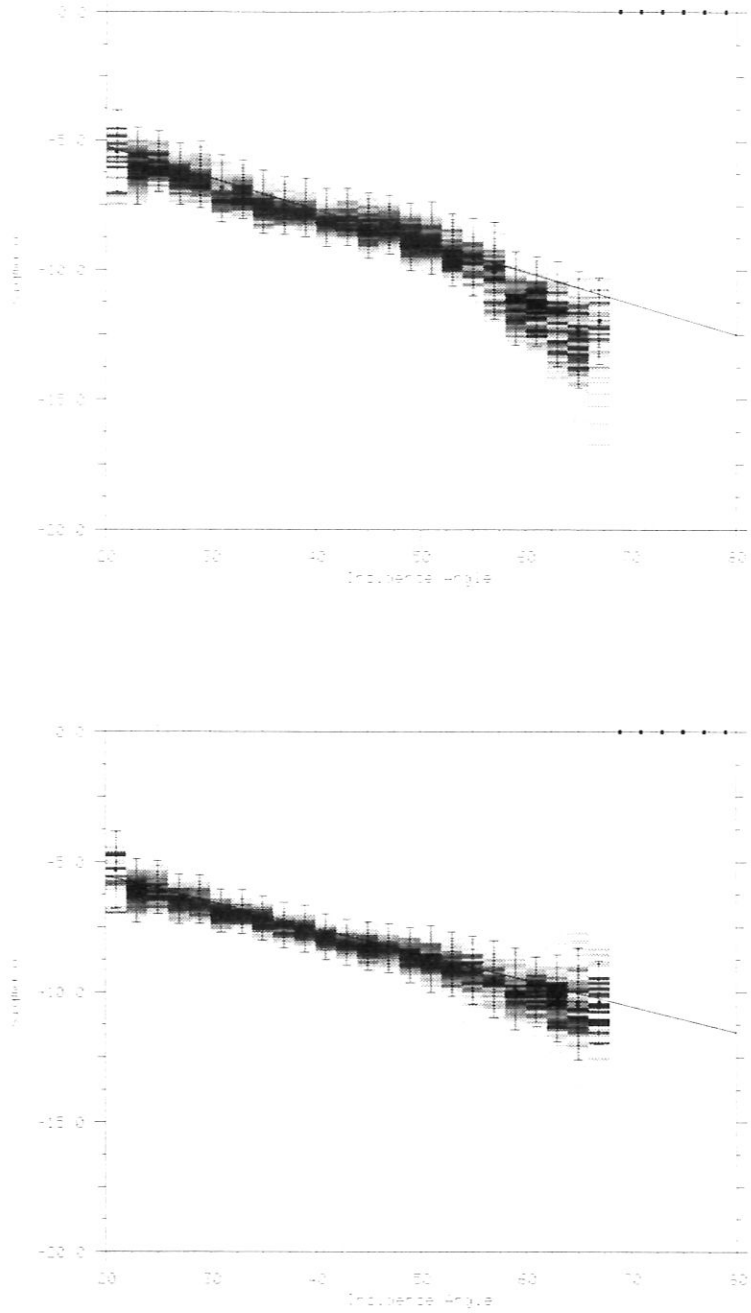

Figure B.1: Variance around a linear regression for the Congo measurements for uncorrected (top) measurements and for measurements corrected with the Amazon correction factors.

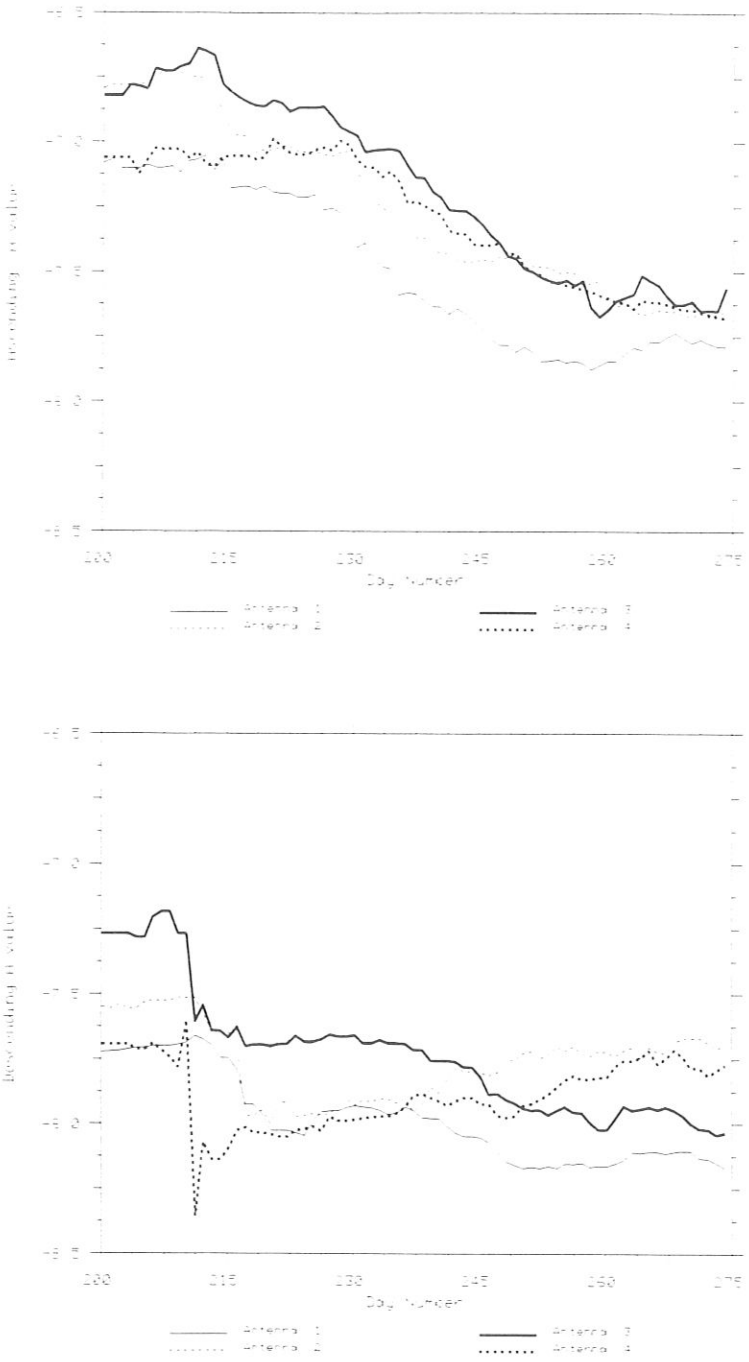

Figure B.2: Model A parameters estimated from the corrected mask. Ascending (top), descending (bottom).

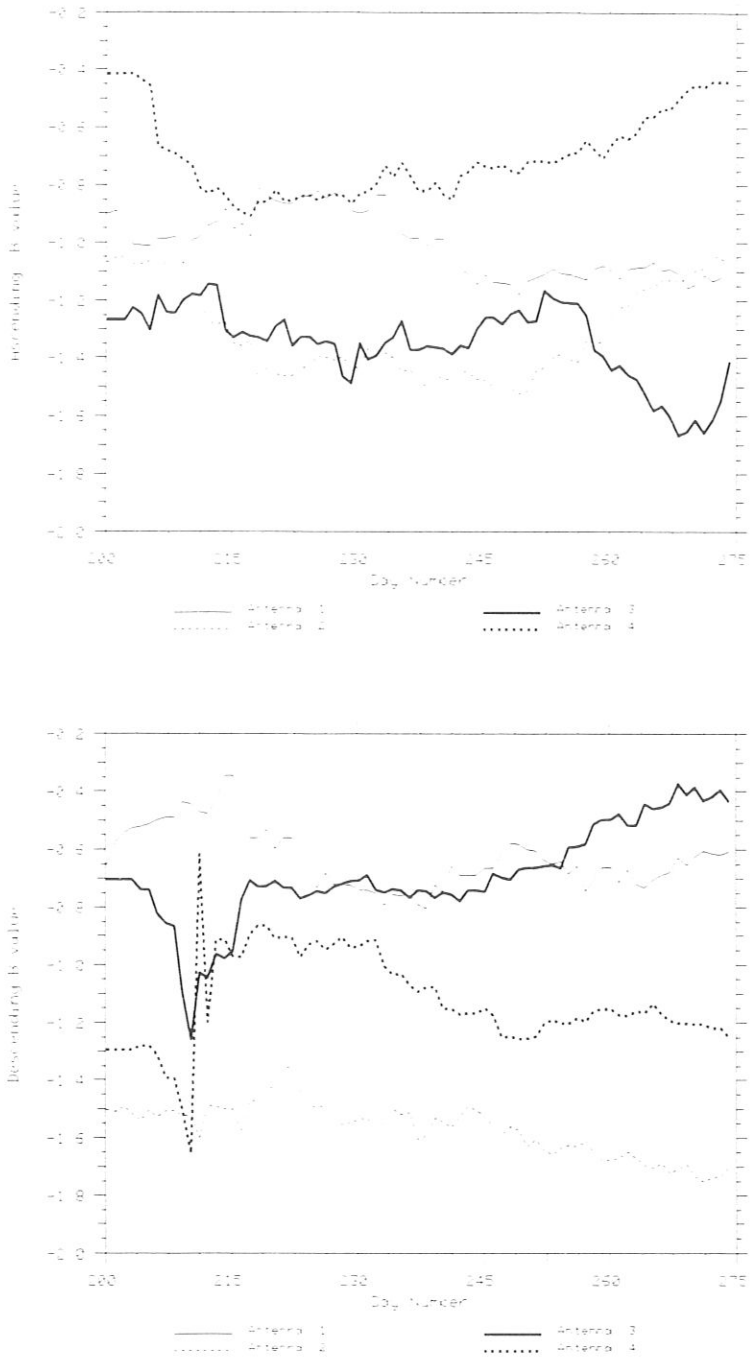

Figure B.3: Model B parameters estimated from the corrected mask. Ascending (top), descending (bottom).

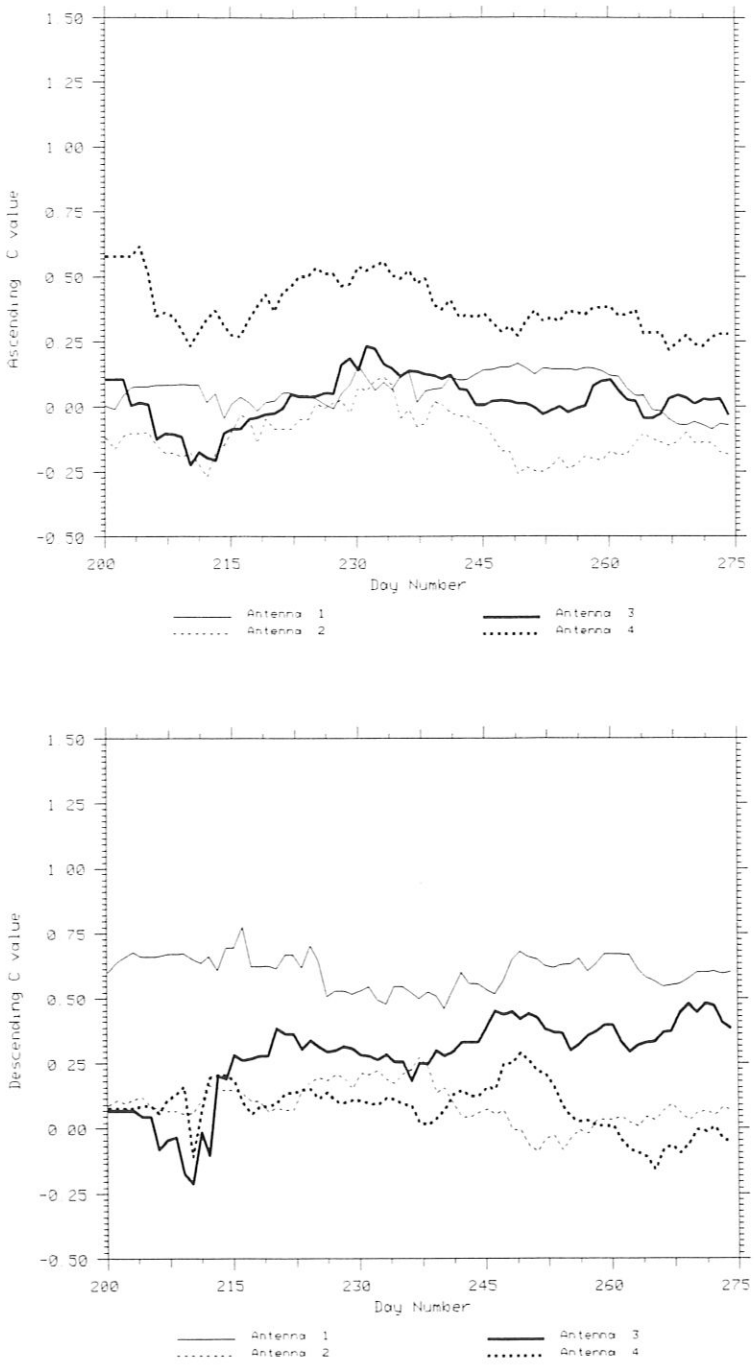

Figure B.4: Model C parameters estimated from the corrected mask. Ascending (top), descending (bottom).

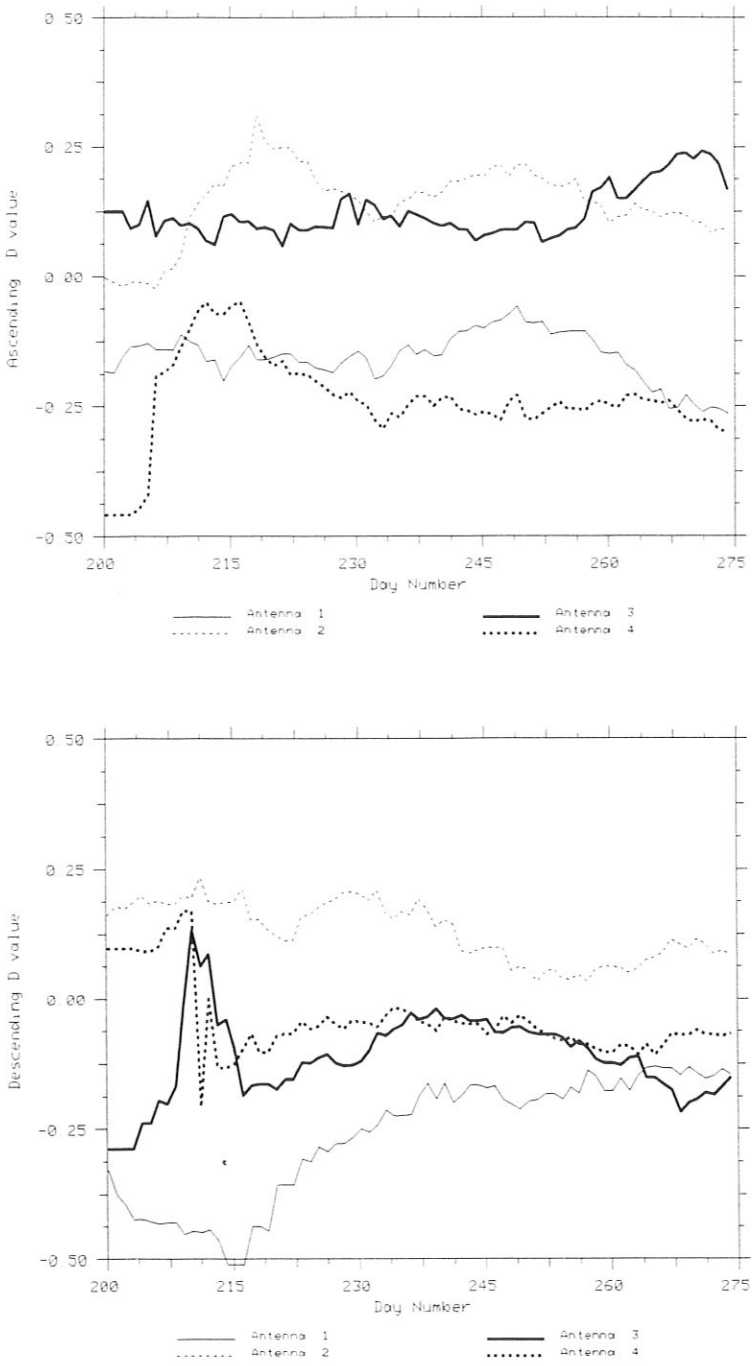

Figure B.5: Model D parameters estimated from the corrected mask. Ascending (top), descending (bottom).

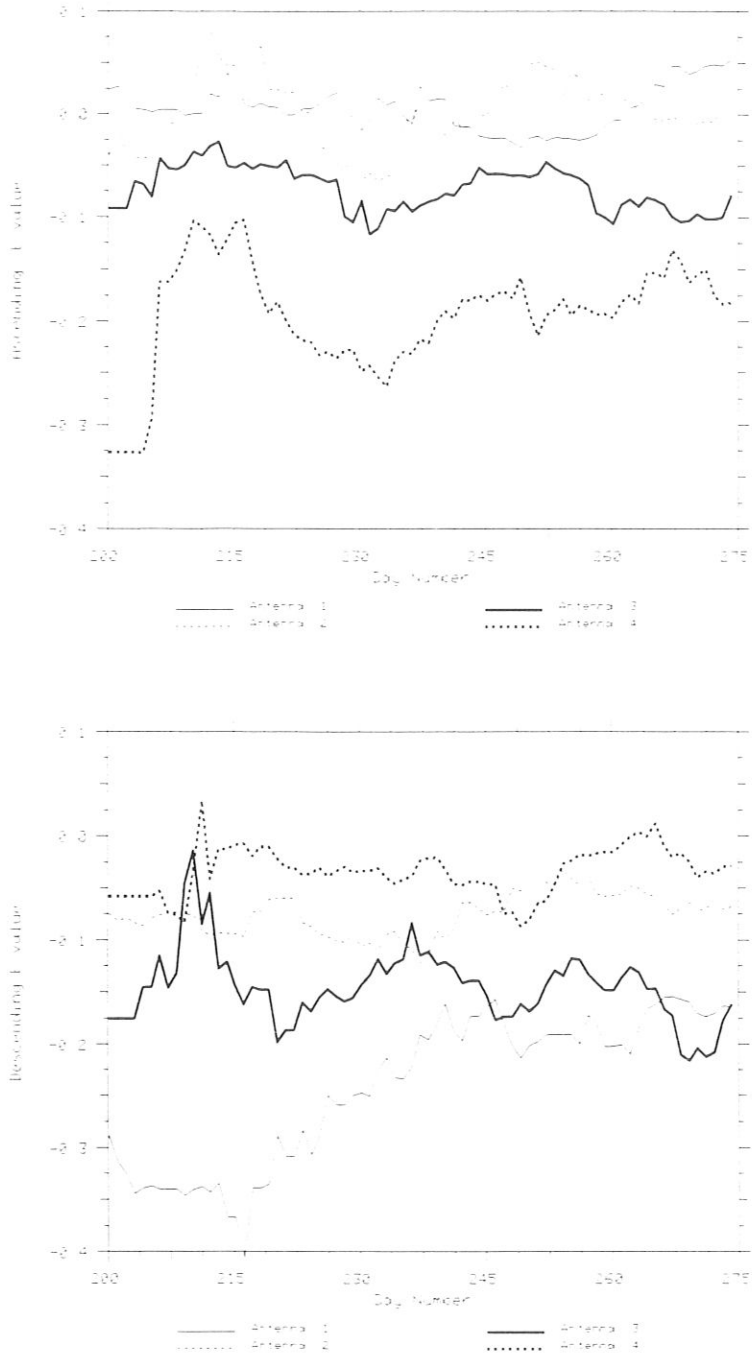

Figure B.6: Model E parameters estimated from the corrected mask. Ascending (top). descending (bottom).

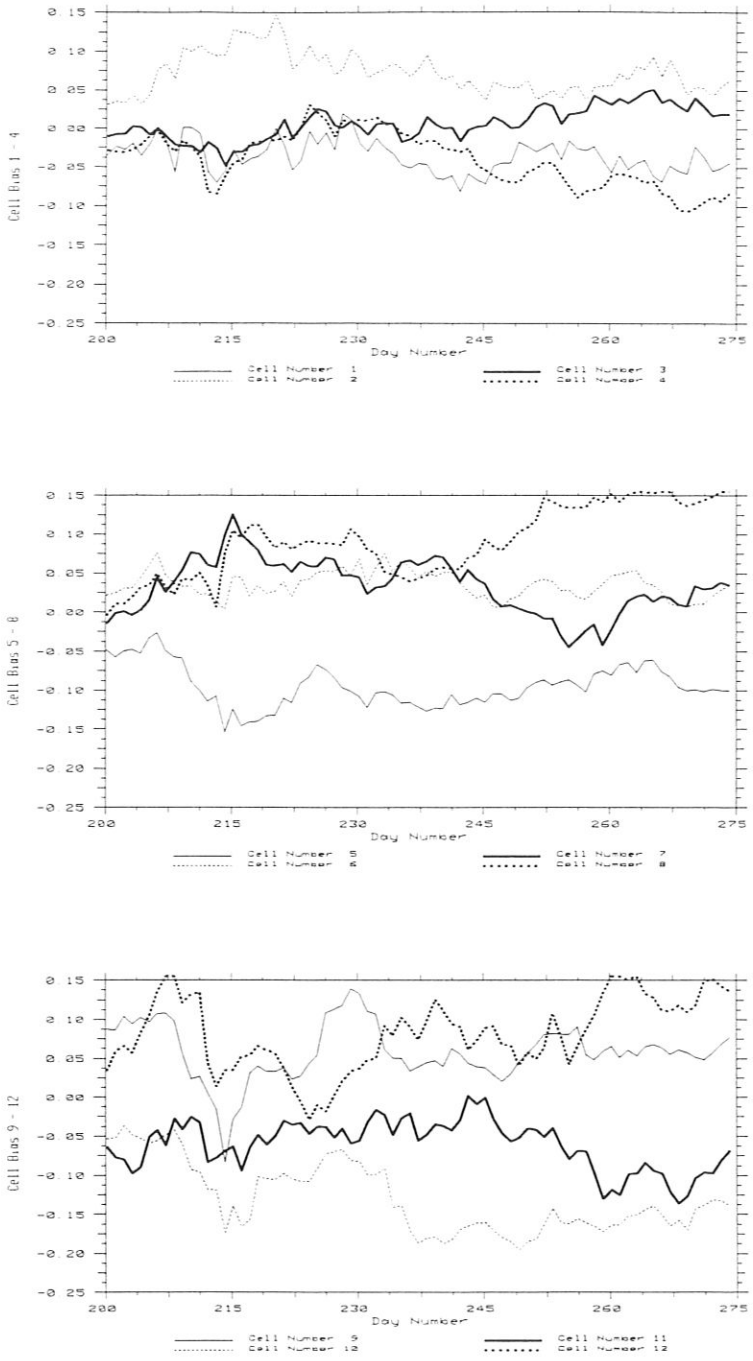

Figure B.7: Model Cell gain biases estimated from the corrected mask. Cells 1 - 4 (top), 5 - 8 (middle) and 9 - 12 (bottom).

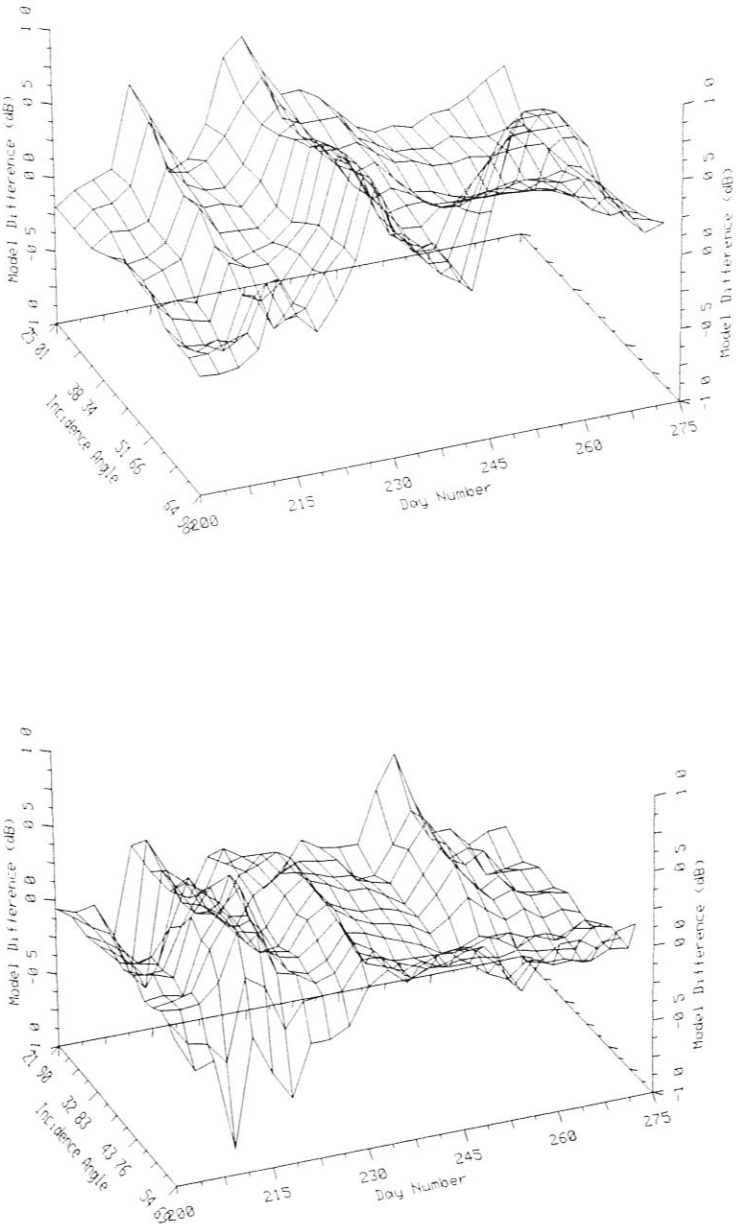

Figure B.8: Difference between the Amazon model and the Congo model for antenna 1. Ascending (top), descending (bottom).

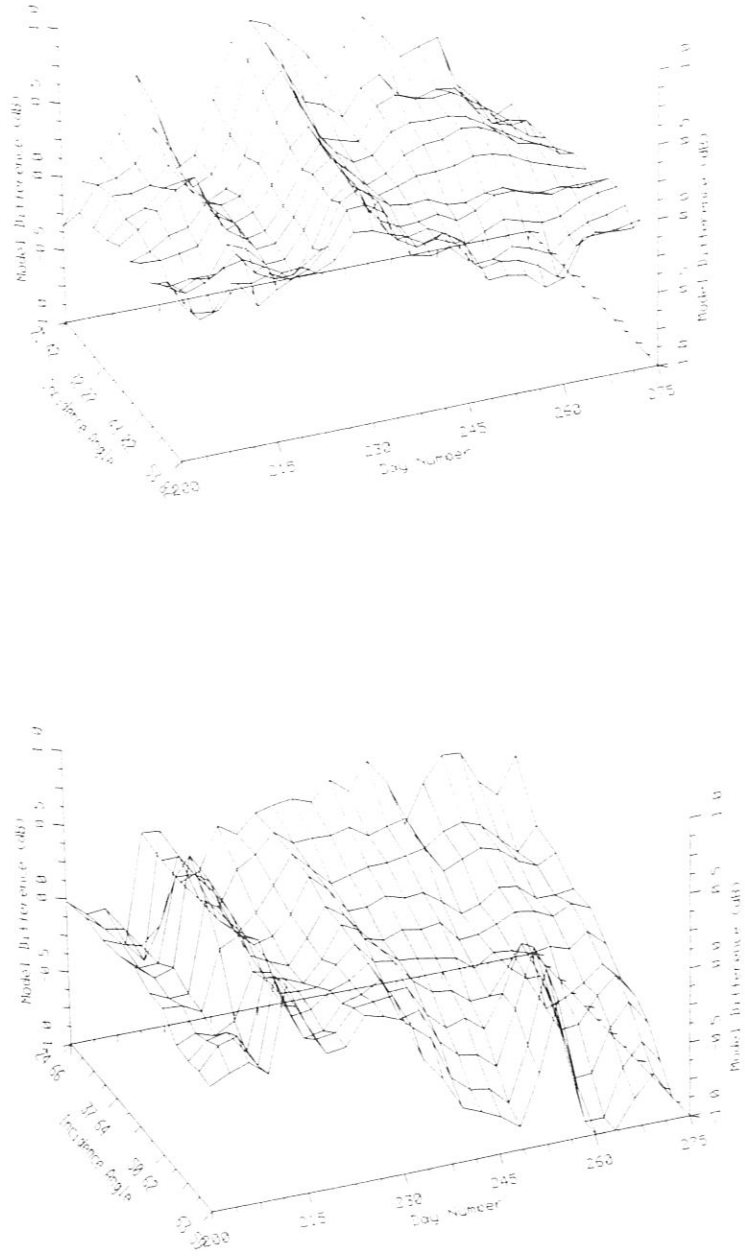

Figure B.9: Difference between the Amazon model and the Congo model for antenna 2. Ascending (top), descending (bottom).

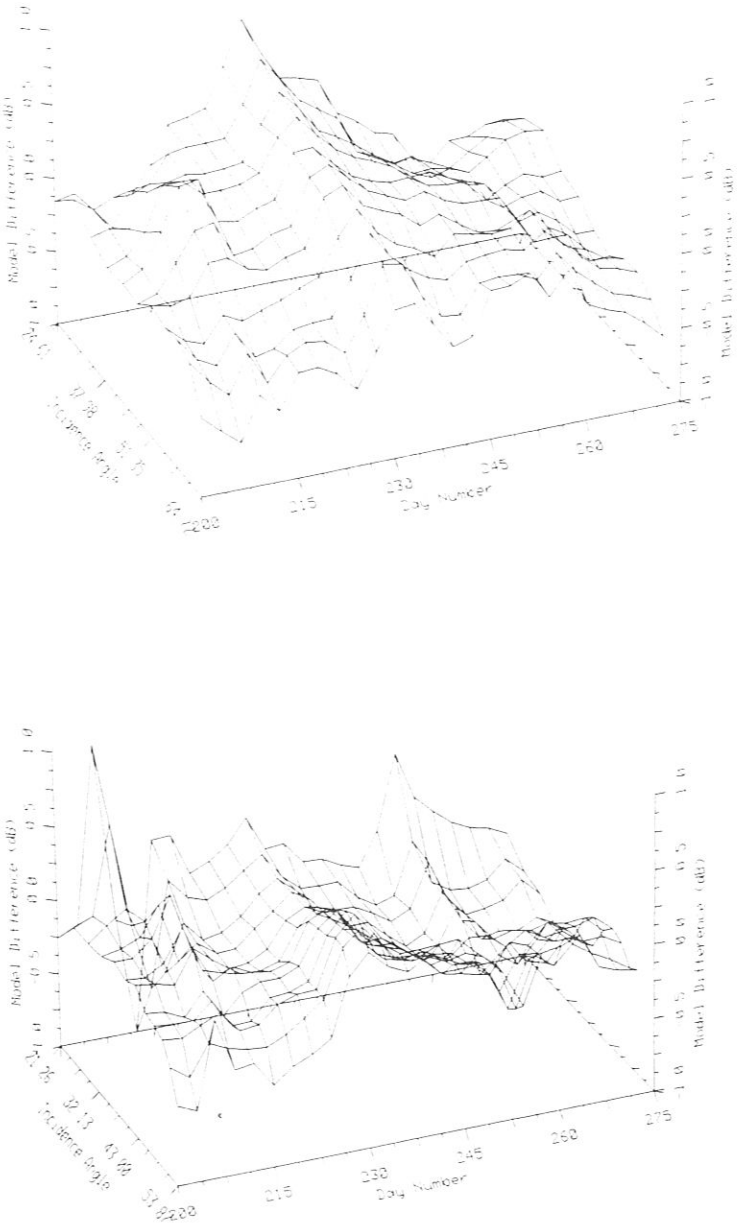

Figure B.10: Difference between the Amazon model and the Congo model for antenna 3. Ascending (top), descending (bottom).

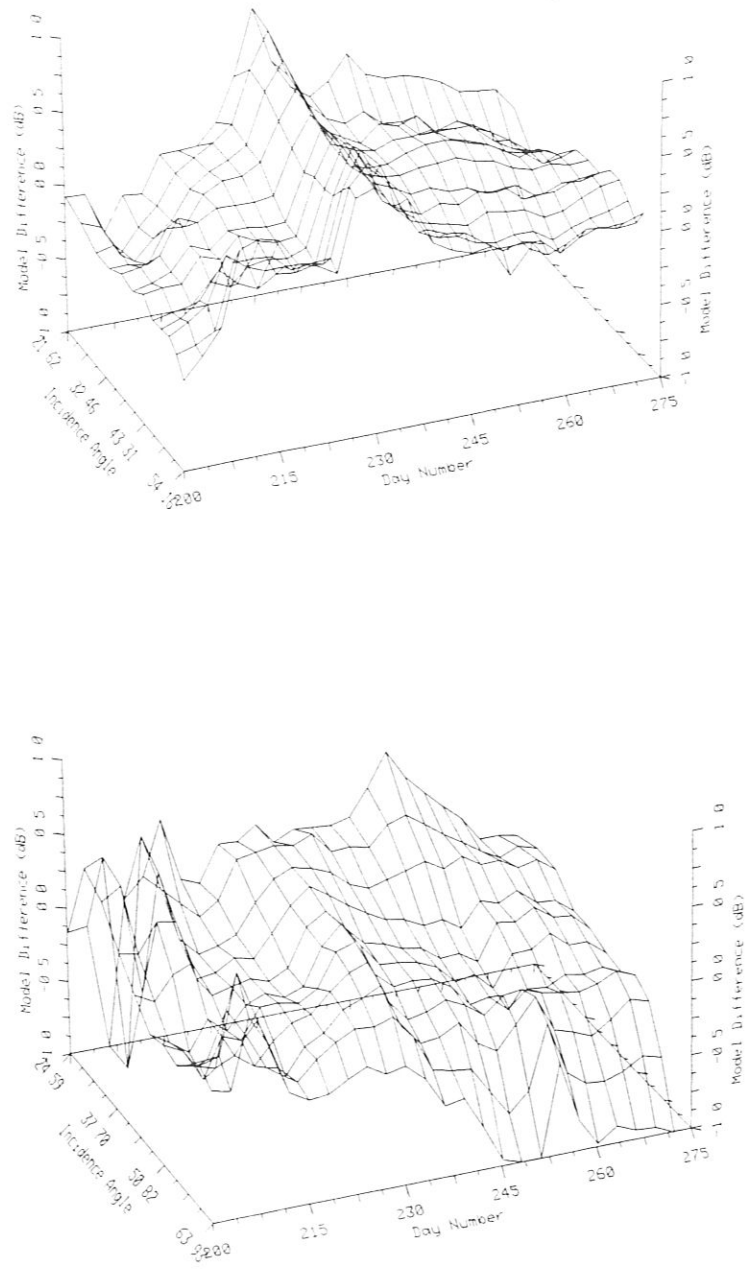

Figure B.11: Difference between the Amazon model and the Congo model for antenna 4. Ascending (top), descending (bottom).

CALIBRATION OF SEASAT SCATTEROMETER USING TROPICAL RAINFOREST

Gary B. Skouson

Department of Electrical and Computer Engineering

M. S. Degree, October 1992

ABSTRACT

The Seasat scatterometer was a satellite scatterometer designed to measure wind speed over the ocean. These measurements have also been shown to be useful for vegetation studies over land. This thesis describes a method for recalibration of Seasat scatterometer measurements. Although other researchers have presented recalibration techniques, their suggested calibrations do not give a correction adequate for some applications. In the approach presented in this thesis, measurements from each of the antennas and cells are modeled as a fourth order polynomial function of incidence angle. Using this model, antenna dependent biases in the system gain, of up to several tenths of a dB, were identified using Amazon and Congo data. In addition to the antenna and cell errors, linearity and time variability of the measurements can be corrected using this model. The correction required to obtain a linear response with incidence angle was as much as five tenths of a dB for some of the far swath measurements with lower corrections for cells closer to the spacecraft. These corrections make it possible to use a measurement without regard to the antenna or cell making the measurement. Using these corrections noise present in original land images is removed.

COMMITTEE APPROVAL:

David G. Long
Committee Chairman

A. Lee Swindlehurst
Committee Member

Richard H. Selfridge
Graduate Coordinator